

THE MEASUREMENT OF RADIATIVE ELECTRON CAPTURE
AND
THE NUCLEAR SPECTRA OF CE-144 AND ITS
DECAY PRODUCTS

DISSERTATION

Presented in Partial Fulfillment of the Requirements
for the Degree Doctor of Philosophy in the
Graduate School of The Ohio State
University

By

WERNER S. EMMERICH, B.Sc., M.Sc.

The Ohio State University

1953

Approved by:

C. D. Humbarton
Adviser

ACKNOWLEDGMENT

Grateful acknowledgment is made to Dr. J. D. Kurbatov for his guidance and helpful advice in the course of this work, and to the entire group of graduate students under his direction, especially Major S. E. Singer and Captain W. J. Auth, for chemical purification of radioactive materials and their help and cooperation with the various phases of the research.

TABLE OF CONTENTS

	<u>Page</u>
I. The Measurement of Radiative Electron Capture.....	1
A. Introduction.....	1
B. Preparation of Radioisotopes.....	6
1. Preparation of Iron-55.....	6
2. Preparation of Argon-37.....	7
3. Preparation of Nickel-59.....	8
C. Review of Radiative Capture Theory..	10
D. Design and Operation of Instruments.	13
1. General Requirements.....	13
2. The first Model Scintillation Spectrometer.....	16
a. Crystal Mounting.....	16
b. Photomultiplier Base.....	16
c. High Voltage Supply.....	19
d. Pulse Amplifier.....	19
e. Single Channel Pulse Height Analyzer.....	23
f. Power Supply.....	26
3. Operation of the First Model....	28
4. Design of the Second Model Scintillation Spectrometer.....	40
a. Crystal Mounting and Photomultiplier Base.....	42
b. High Voltage Supply.....	42
c. Linear Pulse Amplifier.....	43
d. Pulse Height Analyzer.....	45
e. Regulated Power Supplies....	51
5. Operation of the Second Model...	57
a. General Operation.....	57
b. Calibration.....	59
c. Overall Efficiency Determination.....	59
6. The Correction for Compton Scattering.....	65

TABLE OF CONTENTS, (cont.)

	<u>Page</u>
E. Experimental Results on Radiative Capture.....	74
1. Introduction.....	74
2. The Measurements of Iron-55....	75
3. The Measurements of Argon-37...	75
4. The Measurements of Nickel-59..	78
F. Discussion of Results.....	86
II. The Nuclear Spectra of Ce-144 and Its Decay Products.....	94
A. Introduction.....	94
B. Mode of Decay.....	96
C. Experimental Results.....	97
1. Internal Conversion Lines.....	97
2. The 175 kev Level in Pr-144....	101
3. The 60 kev Transition in Nd-144.....	103
4. The Branching Ratios in Ce-144..	104
5. The Branching Ratios in Pr-144..	110
D. Discussion of the Beta Transitions..	115
E. Excited States of the Even-Even Nucleus Nd-144.....	118
F. The Scheme of Disintegration for Ce-144 and Pr-144.....	119
Bibliography.....	121
Autobiography.....	124

I. THE MEASUREMENT OF RADIATIVE ELECTRON CAPTURE

A. INTRODUCTION

Radiative orbital electron capture originates from the change in charge distribution which takes place when an electron is absorbed into the nucleus. In ordinary electron capture all the available energy in the transition leading to a definite energy level of the product nucleus is carried away by a neutrino. Because of the charge transfer it is possible, however, that a part of the available energy may escape as a photon, and only the remaining balance is carried away by the neutrino. This allows transitions to intermediate states having a continuous range of energies. The maximum possible energy of the photon thus represents the case in which the neutrino carries nothing but its energy of formation. This is either very small by comparison or zero. Consequently the maximum experimental endpoint of the electromagnetic radiation is direct evidence regarding the transition energy of the orbital electron capture process.

The theory of radiative electron capture is analogous to internal bremsstrahlung as developed for beta decay by Knipp and Uhlenbeck (1) and independently by Bloch (2). The application to orbital electron capture was made by Morrison and Schiff (3). Chang

and Falkoff (4) treated various types of coupling and forbidden beta transitions. The work was reviewed by Jauch (5) and extended in the case of radiative electron capture.

The first experimental measurements on radiative electron capture were reported by Bradt et al (6). Later experiments on Fe-55 made by Maeder and Preiswerk (7), Bell, Jauch, and Cassidy (8), and Bolgiano, Madansky, and Rasetti (9) have confirmed the endpoint energy and spectral distribution.

Radiative electron capture has also been studied in A-37. The spectrum was measured by Anderson, Wheeler, and Watson (10), but the spectral analysis was incomplete because the data could not be corrected for Compton scattering in the detection crystal.

Whereas the above two examples represent allowed transitions, investigations on forbidden transitions have not been made to date with the exception of Tl-204. This nucleus was studied by DerMateosian and Smith (11) in conjunction with the establishment of its decay scheme. In the course of their work, the radiative electron capture was measured by coincidence techniques for the purpose of measuring the disintegration energy.

For the purpose of studying the radiative capture energy distribution in allowed and forbidden transi-

tions the following rules regarding the selection of suitable radioactive species should be considered:

1. Procurement of sufficient activity.
2. Chemical purification.
3. Absence of gamma rays, in the product nuclei.
4. Absence of positron disintegration.
5. Absence of other isotopes of the same element disintegrating with the emission of electromagnetic radiation.
6. Large difference between the transition energy and the K-L x-ray energy.
7. Long half life to permit a thorough investigation of the radiative capture spectrum.

Only a few radioisotopes can be found which satisfy all of the above requirements to a sufficient degree to warrant the investigation of their radiative capture spectrum. Since this radiation has a small probability as compared to ordinary electron capture, it is necessary to obtain activities on the order of at least 0.1 millicurie. In case of transitions for which the electron capture half life is long, neutron capture in a high flux nuclear reactor is the only reasonable mode of production at this time. Therefore the list of possible isotopes is limited to those which can be formed by (n, γ) , and possibly by (n, p) or

(n, α) reactions.

(n, γ) being the most prolific of these reactions, it represents a favorable mode of production. In this case, the product isotope belongs to the same element as the parent isotope and is therefore inseparable by chemical means. The presence of large quantities of inert material is of no consequence in the measurement of the radiative capture, but relatively large quantities of material are subject to chemical purification against radioactive contaminants, which may introduce some technical difficulties.

The disintegration of the isotope should not involve any excited states of the product nucleus having an energy greater than an insignificant percentage of the electron capture transition. Any gamma ray near or above the endpoint energy of the electron capture radiation may produce Compton scattering in any given detector so that the measurement of the spectrum, if not completely overshadowed, is subject to large statistical uncertainties. Similarly, in the case of positron emission, interference is encountered from annihilation radiation unless the positron-electron capture branching ratio is negligibly small.

Not only is it desirable that the product nuclei be free from gamma ray emission, but other radioactive isotopes of the same element should not remain at the

time of measurement, if they decay with the emission of electromagnetic radiation. It is therefore obligatory to ascertain that all such activities have died out by the time the measurements are undertaken.

If the investigation is made in a heavy element, the x-rays emitted in the ordinary electron capture may be of sufficient energy to overlap the radiative capture spectrum. This is especially true since the endpoint of the radiative spectrum is lower than the transition energy by an energy equal to the K shell binding energy.

A thorough survey of the isotopic table showed that several species are known in which all of the above conditions are satisfied to a reasonable degree. From this list, the following three isotopes were chosen because they were available in this laboratory or could be obtained by neutron irradiation:

<u>Isotope</u>	<u>Half-life</u>	<u>Expected Endpoint Energy</u>
Fe-55	2.9 years	217 kev
A-37	34 days	813 kev
Ni-59	8×10^4 years	1065 kev

In these examples, the endpoint energies are sufficiently high so that the radiative electron capture should be experimentally observable. The half-lives are within experimentally suitable ranges, and isotopic interference

can be eliminated.

In these three examples, the endpoint energy can be calculated in advance of the present measurement by the indirect means of mass difference between the parent and the daughter nuclei. These mass differences have been determined by the method of (p,n) reaction thresholds. If the nuclei: Mn-55, Cl-37, and Co-59 are bombarded by protons with a suitable accelerator, such as a Van de Graaff generator, it is observed that above a certain threshold energy, neutron emission takes place from the nuclei. This threshold energy is related to the Q value of the reaction by:

$$E = - Q M / (M - m)$$

where E is the threshold energy, M is the mass of the product nucleus, and m is the mass of the proton. If the disintegration energy between neutron and proton is deducted from the Q value, the disintegration energy of the electron capture is left. In the case of K electron capture, the K shell binding is subtracted also to obtain the endpoint energy of the radiative electron capture spectrum.

B. PREPARATION OF RADIOISOTOPES

1. Preparation of Iron-55

Radioactive Fe-55 is prepared by slow neutron irradiation of iron. The stable isotope Fe-54 is

prepared by slow neutron irradiation of iron. The stable isotope Fe-54 is present in natural iron with an abundance of 5.81 per cent. Other stable isotopes are Fe-56, Fe-57 and Fe-58. The radioactive isotope Fe-59 is formed by neutron capture in Fe-58. It has a half life of 46 days and emits beta rays of 0.26 and 0.46 Mev followed by gamma rays of 1.1 and 1.3 Mev energy. This represents a serious interference in freshly irradiated material.

The Fe-55 investigated in the present work has been produced at the Oak Ridge reactor and aged for over five years corresponding to 40 half lives of Fe-59. No gamma rays were observed showing that the material was free from interfering radiation of Fe-59.

The iron was chemically purified by ethyl ether extraction technique. Extraneous radiation found in unpurified iron was believed to originate from Mn-54 formed by (n,p) reaction.

2. Preparation of Argon-37.

This isotope can be prepared by (n,gamma) reaction on A-36 or (n,alpha) reaction on calcium. The latter method has the advantage that the irradiation produces also Ca-41, which is in itself an electron capture species and may be investigated for radiative capture radiation. Thirty grams of calcium oxide were irradiated for a period of two months in the Brookhaven reactor with a

flux of about 4×10^{12} neutrons/sec/cm².

There is no isotopic interference in argon, because the only other isotope produced is A-41, which has a half-life of two hours. The chemical separation from calcium was accomplished by dissolving the calcium, which was irradiated in the form of calcium oxide, in water and extracting the gaseous products into an evacuated vessel. A detailed description of the procedure is given by S. E. Singer (12). The presence of gaseous C-14, which might have been formed during the irradiation, is of no importance in the measurement of the radiative capture spectrum since C-14 decays by beta emission of 150 kev without any gamma radiation. Nevertheless, a half-life measurement has been carried out as shown in Figure 1. The experimental half-life of 35 days is in agreement with previous measurements.

3. Preparation of Nickel 59.

The activity of Ni-59 is produced by (n,gamma) reaction on Ni-48, which has a natural abundance of 67.7 per cent. Other stable nickel isotopes are Ni-60, 61, 62, and 64. Only one other nickel radioactivity is produced in the irradiation with appreciable half-life. This is Ni-63 which disintegrates by emitting beta rays of 65 kev energy. This radiation does not affect the radiative capture spectrum of Ni-59.

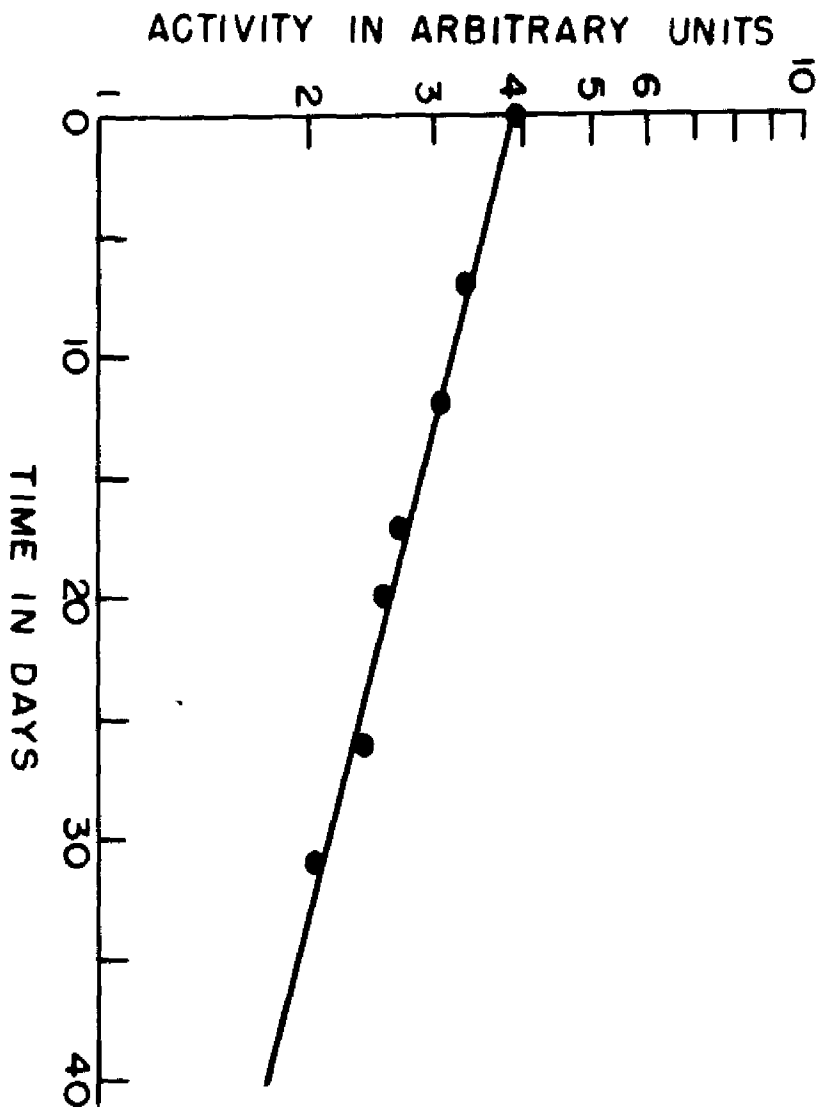


FIGURE 1 HALF-LIFE OF A-37

For the present investigation, 40 grams of nickel metal were irradiated for a period of four weeks in position A of the NRX reactor operated by the Eldorado Mining, Ltd., at Chalk River, Canada. Upon arrival of the irradiated metal, strong gamma radiation was found to be present and believed to be primarily due to the formation of radioactive cobalt isotopes through (n,p) reactions.

The chemical purification of nickel was carried out by Major S. E. Singer utilizing a novel method of nickel precipitation with dimethylglyoxime (12). After six steps of purification, only insignificant traces of foreign radioactivities were left. The material was reduced to nickel-oxide, and 15 grams of the nickel were actually employed in the radiative capture measurements.

C. REVIEW OF THE RADIATIVE CAPTURE THEORY

The origin of the electromagnetic radiation is the change in the charge distribution when the nucleus falls to a stable state through the capture of an orbital electron. The electromagnetic process may occur in two distinct ways: the nucleus may first emit a virtual positron and a real neutrino. The positron is subsequently annihilated by an electron of the K shell. Alternately, the K shell electron may be scattered into

an intermediate state by emission of a photon and is then absorbed into the nucleus with the emission of a neutrino.

The Hamiltonian which represents the transition may be written in the linear form:

$$H = H(n) + H(e)$$

where $H(n)$ is the Hamiltonian for the electron capture interaction, and $H(e)$ describes the interaction with the electromagnetic field.

The process is calculated by means of second order perturbation method according to the standard formula for dP , the transition probability per unit time for a photon of momentum k within dk and solid angle dv , and a neutrino within the solid angle du .

$$dP = 2\pi \sum (H)^2 dr$$

(H) stands for the second order matrix element:

$$(H) = \sum \frac{H(f,n) H(n,i)}{E(i) - E(n)}$$

and dr denotes the density of the final states per unit energy range:

$$dr = \frac{V k^2}{(2\pi)^3} dk dv \frac{V n^2}{(2\pi)^3} du .$$

By evaluation of $(H)^2$, J. M. Jauch (5) obtains for the probability per unit time of the emission of a photon of energy w within dw :

$$dP = \frac{2}{137\pi^2} G^2 (M)^2 (r^2 + (r_0 - m_0)^2) w (W - w)^2 dw$$

where:

G = coupling constant of the order 10^{-32} cm^2 .

(M) = nuclear matrix element

W = maximum photon energy

The relative probability for radiative capture is obtained by dividing dP with P_0 , the electron capture probability per unit time, which is:

$$P_0 = \frac{1}{\pi} G^2 (M)^2 u(0)^2 W^2$$

where $u(0)$ is the K shell electronic wave function.

The result is:

$$\frac{dP}{P_0} = \frac{2}{137\pi} \frac{r^2 + (r - m_0)^2}{u(0)^2} w (1 - w/W)^2 dw.$$

If the photon energy is large in comparison to the K shell binding energy, J. M. Jauch (5) shows that the following approximations are valid:

$$u(0)^2 = 1$$

$$r = \frac{W}{2mc^2w}$$

$$r_0 = \frac{-W}{2mc^2w}$$

$$m_0 = \frac{-mc^2}{2mc^2w}$$

which yields in approximation:

$$r^2 + (r_0 - u)^2 = \frac{1}{2m^2c^4}$$

and the result:

$$\frac{dP}{P_0} = \frac{1}{137\pi} \frac{w dw}{m^2c^4} (1 - w/W)^2 .$$

The total number of radiative capture transitions per electron capture is given by:

$$\int \frac{dP}{P_0} = \frac{1}{137 \times 12 \pi} (W/mc^2)^2 .$$

A linear plot of the experimental data is possible in analogy to a Kurie plot in the beta decay theory:

$$\frac{1}{w} \frac{dP}{dw} = \frac{P_0}{137 \pi} \frac{1}{(mc^2)^2} (1 - w/W)^2$$

$$\frac{N}{w} = K (1 - w/W)$$

where $N = \frac{dP}{dw}$ = Number of counts per unit time per unit energy range, and $K = \text{constant}$.

D. DESIGN AND OPERATION OF INSTRUMENTS

1. General Requirements.

In the measurement of the internal bremsstrahlung originating through radiative electron capture, two determinations are of interest. First, the determination of the endpoint energy gives the transition energy. If this has already been determined by indirect means, such as a threshold energy measurement of the (p,n) reaction, a confirmation of the transition energy can be obtained by the direct method.

The second measurement of interest concerns the spectral shape of the radiative capture radiation. This shape can be obtained by direct measurement.

Since the radiative capture process is expected

to occur in the most favorable cases only with a probability of 10^{-3} as compared to ordinary electron capture, and since the radiation is spread out through a continuous region of energy, the most efficient method of detection for electromagnetic radiation should be employed in the measurement.

The most efficient method known to date for the measurement of electromagnetic radiation is also the most widespread method, namely, scintillation spectroscopy with thallium activated sodium iodide crystals. This method has been developed considerably during the time that this study was made, and a detailed description of the equipment for the present study is included here.

A scintillation spectrometer consists essentially of the following components:

1. Scintillation crystal
2. Photomultiplier
3. Pulse amplifier
4. Pulse Height Analyzer
5. Scaler
6. Power supplies

The mode of operation is as follows: A photon incident on the scintillation crystal interacts with an electron either through the photoelectric process or through Compton scattering. The electron traverses

the crystal and dissipates its energy in the neighborhood of its path. This causes excitation in the crystal lattice which results in the emission of fluorescence radiation. The light which is formed in this process leaves the crystal and strikes the photo-sensitive cathode of the photomultiplier tube. Here the light causes emission of photoelectrons which are collected at the first dynode by electro-static focusing inside the tube. Each electron striking a dynode causes the emission of several secondary electrons.

This process is repeated through ten dynode stages in the photomultiplier. The total average electron multiplication varies between 10^5 and 10^7 , depending on the voltages applied to the dynode stages. The electrons are then collected at the anode and form an electric current. Each gamma ray striking the scintillation crystal thus causes a current pulse at the output of the photomultiplier.

The pulses are further amplified by means of a vacuum tube amplifier until they attain a peak height of several volts. Pulse height analysis of the pulses is then performed by feeding the pulses into two discriminating circuits biased at different voltage levels. These are connected in anti-coincidence so that only those pulses are counted which actuate the lower biased discriminator alone. Thus pulses are counted only if

they fall in amplitude within the "window" displayed by the discriminating circuits. The output is fed into a conventional scaling circuit. Because one channel is scanned at a time, this type of analyzer is generally known as a single channel differential pulse height analyzer.

2. The First Model Scintillation Spectrometer

2a. Crystal Mounting: - The first model scintillation spectrometer for the measurement of continuous electromagnetic radiation is built closely analogous to the outline given above. A single crystal of thallium activated sodium iodide, one inch diameter and one half inch high, is used. It is polished and placed in a copper cap lined with highly reflecting aluminum foil. In order to keep the crystal dry, the cap is filled with argon gas, and an RCA type 5819 photomultiplier fitted into the cap so that the crystal is in contact with the photosensitive cathode as shown in Figure 2. The entire assembly is wrapped with black plastic tape to make it light and air tight.

2b. Photomultiplier base: - The electrical connections of the photomultiplier are made as shown in Figure 3. The resistors and condensers are mounted closely to the pins on the socket of the tube, and the high voltage and output signal fed through coaxial cable. The output lead is kept as short as possible.

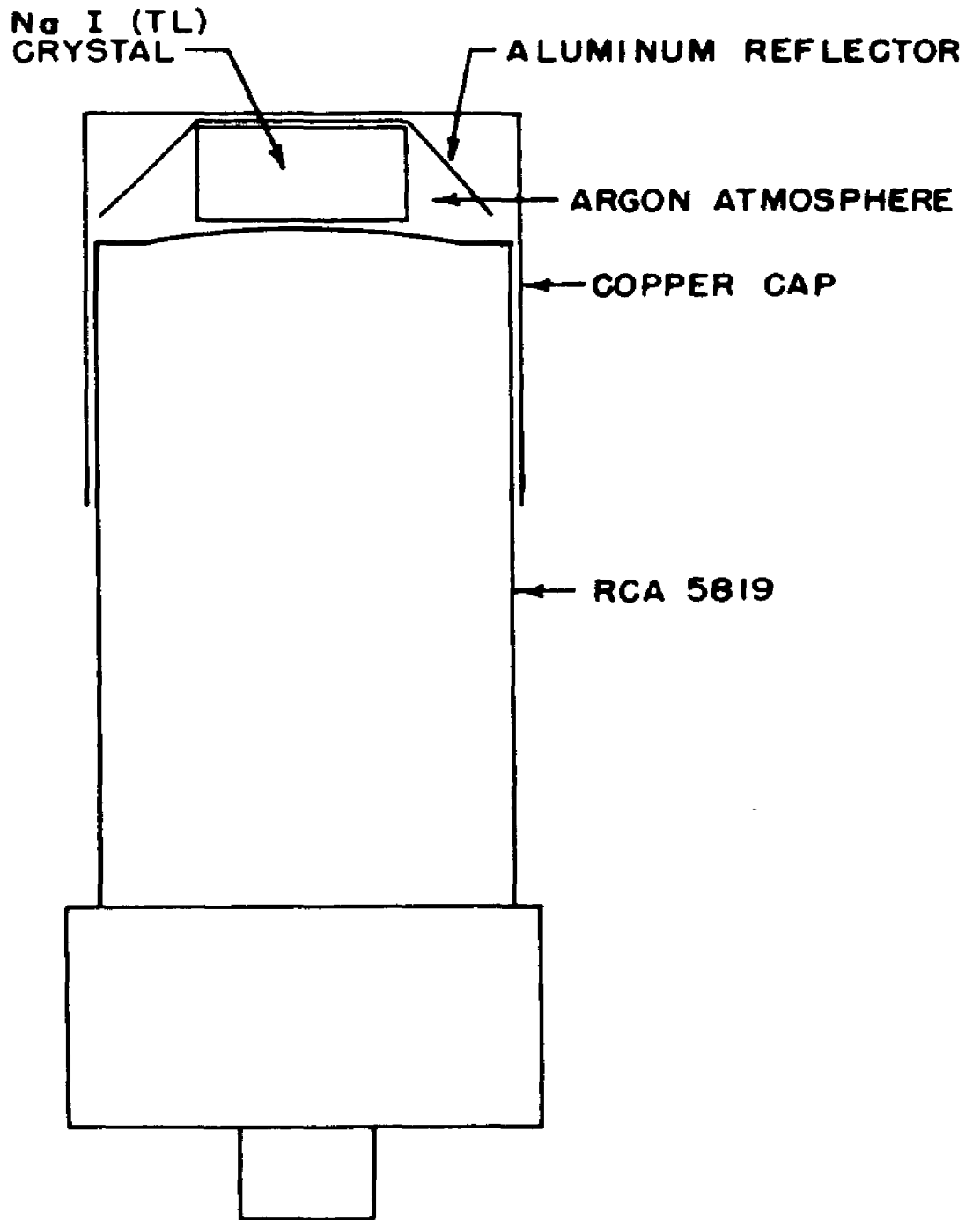
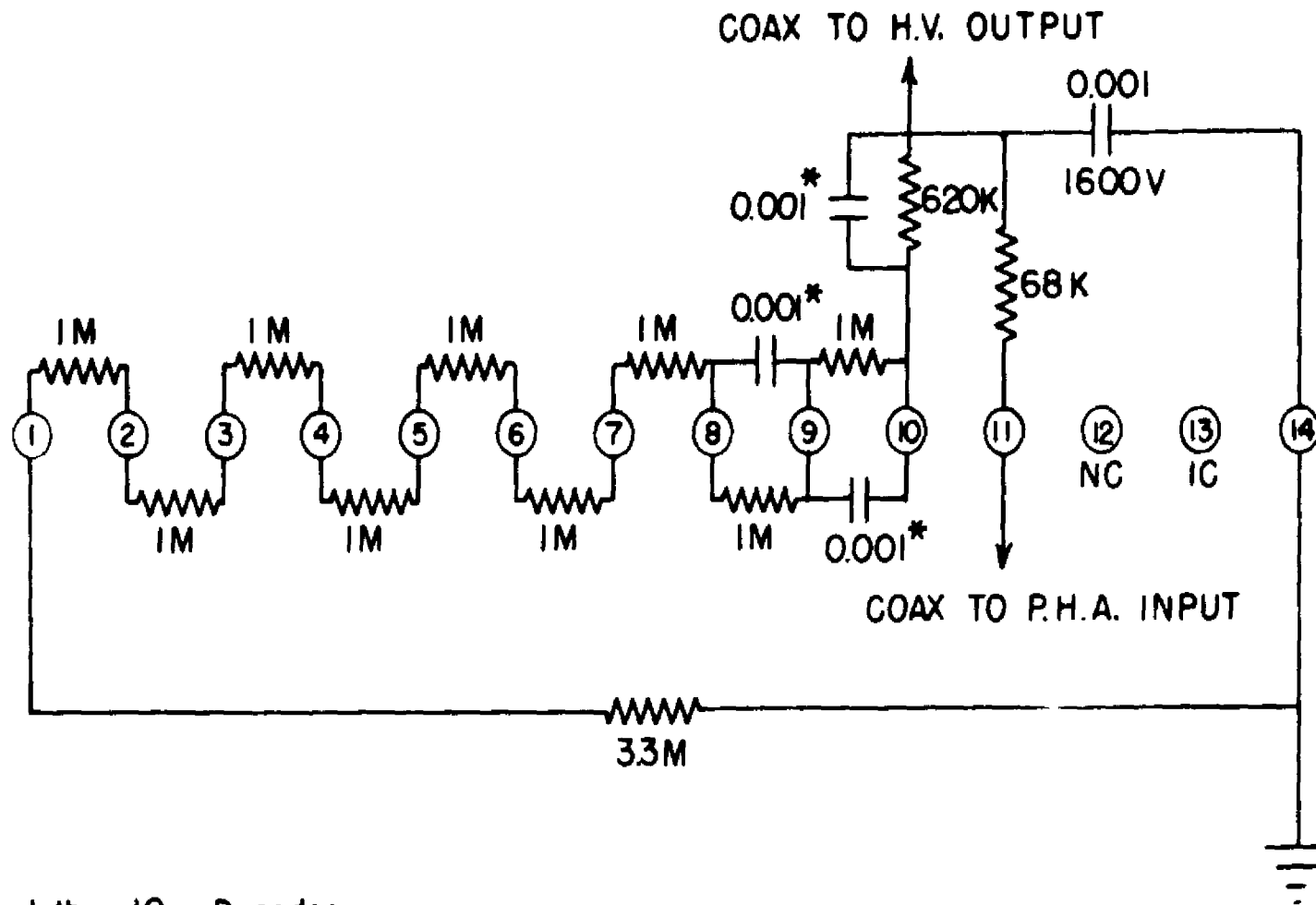


FIGURE 2 SCINTILLATION SPECTROMETER HEAD

PHOTOMULTIPLIER CONNECTIONS



Pins 1 thru 10 - Dynodes
 Pin 11 - Anode
 Pin 14 - Cathode

* Ceramics
 All resistors 1 watt

FIGURE 3

The resistors form essentially a voltage dividing system such that the voltage drop across each dynode is equal. Capacitors across the last three dynode stages prevent the feedback of transients to the lower dynodes. The photomultiplier assembly is placed in an electric and magnetic shield, shown in Figure 4.

2c. High Voltage Supply: - The high voltage needed to operate the photomultiplier tube is obtained from a half-wave rectifier followed by a conventional choke and capacitor filtering system. The filtered output is stabilized by a string of 5651 voltage reference tubes.

In order to insure proper firing, one of them is shunted by a high resistance. The output is fed into a potentiometer circuit with a precision circular rheostat. A switching arrangement provides two scanning ranges, and the rheostat is fitted with a calibrated dial set to give one volt per division. The range of scanning extends from 570 to 870 volts. The complete circuit diagram is found in Figure 5, and a top view of the apparatus is shown in Figure 6.

2d. Pulse Amplifier: - The requirements needed for an output of constant amplitude pulses are less severe than in the case of varying amplitude. The amplification need not be linear. The amplifier may overload so long as it does not produce positive overshoot. The output stage does not have to handle

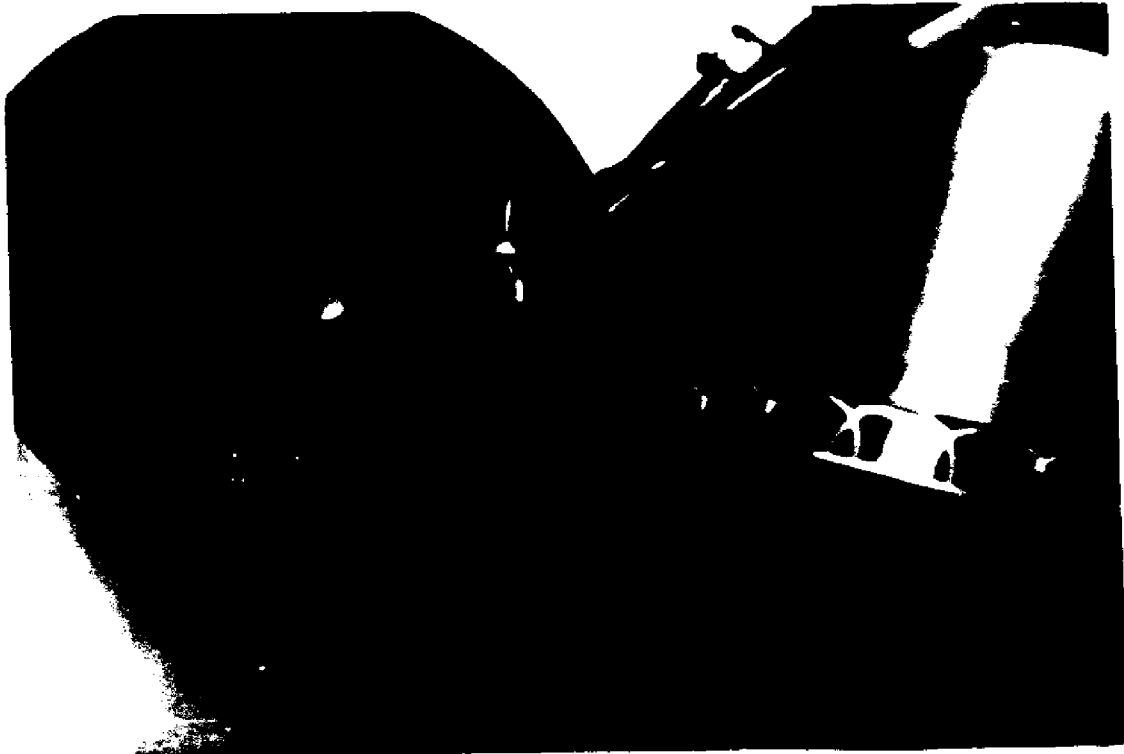


Figure 4. Photomultiplier Base Assembly

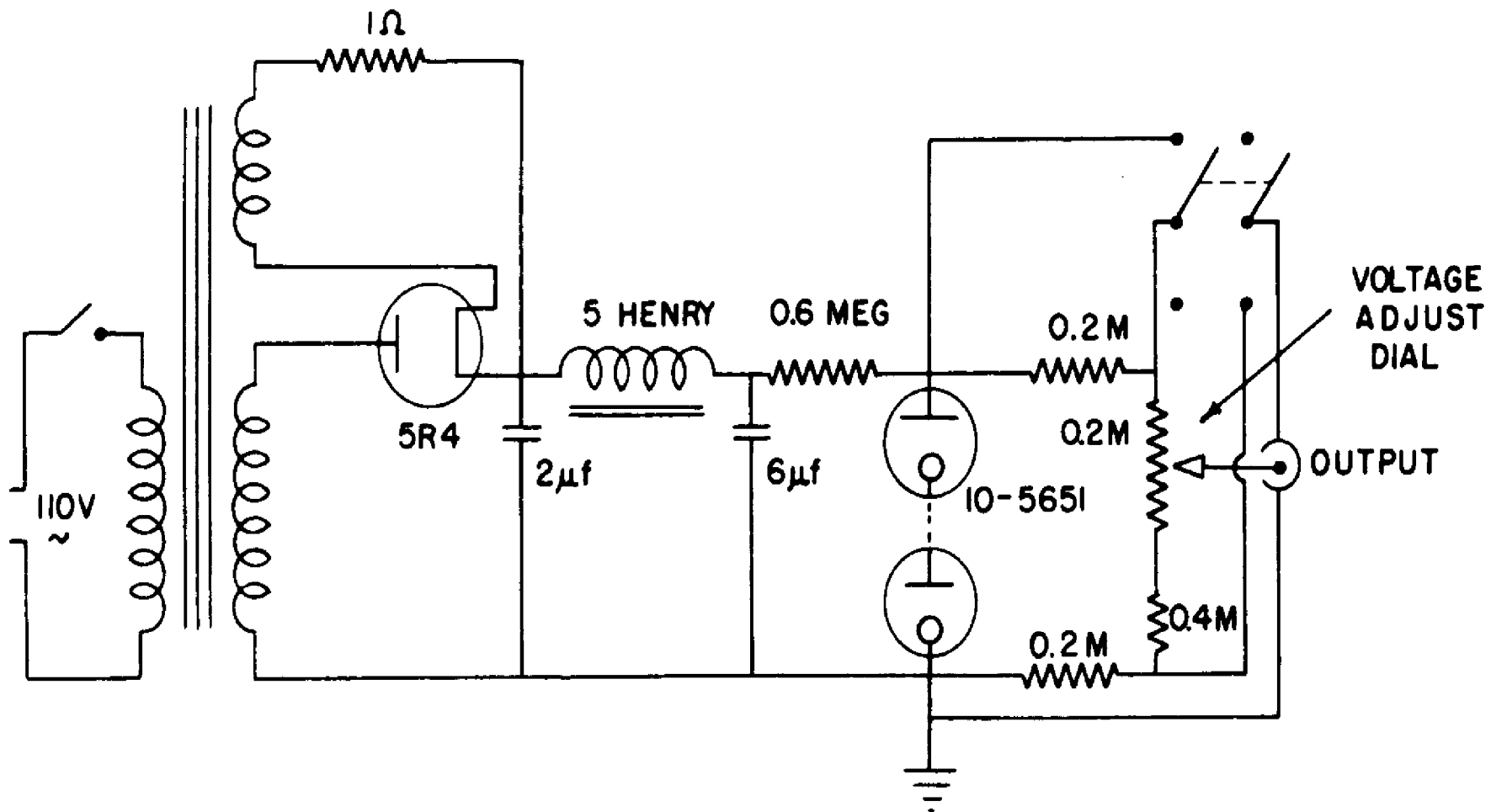


FIGURE 5 HIGH VOLTAGE SCANNING SUPPLY

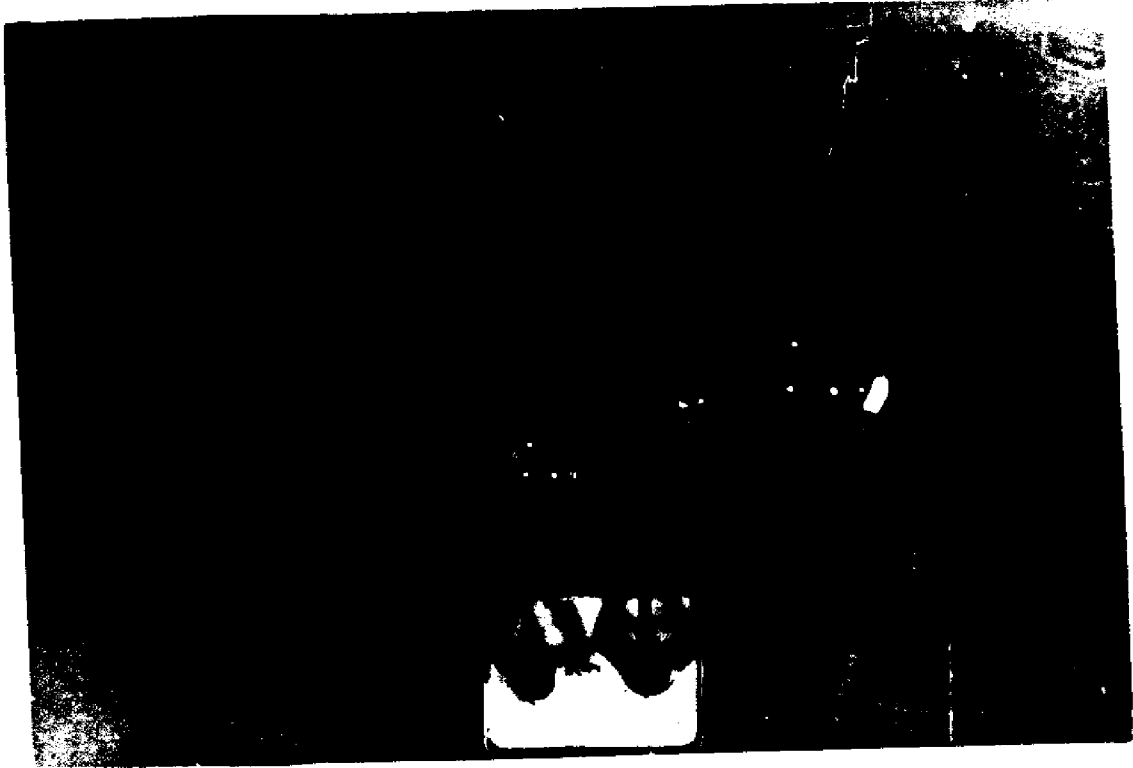


Figure 6. Top View of Scanning Supply

pulses above 20 volts in height, because the threshold can be set arbitrarily below such a figure. The amplifying circuit in this instrument is shown diagrammatically in Figure 7. It consists of three resistance coupled amplifying stages employing the high mu 6AH6 type pentodes. A negative feedback system employing germanium diodes is included for the reduction of spurious responses to excessive pulse height.

2e. Single Channel Pulse Height Analyzer: - The pulse height analyzer consists of an upper gate, a lower gate, a univibrator for each of these, and a discriminator output stage. The complete circuit diagram is shown in Figure 8. The gates are of identical construction, each consisting of two cathode coupled 6AK5 pentodes. The grids of the second pentodes are connected to a constant voltage supply, which is regulated by a 5651 voltage reference tube. The grid of the lower gate is kept at a lower voltage than that of the upper gate by means of a voltage dividing network, which is adjustable. This determines the slit width or "window" of the pulse selector.

Pulses which exceed the base line of the gates are fed into Schmitt trigger circuits constructed with 6J6 duo-triodes. The trigger circuits are adjusted as univibrators having a pulse length of two microseconds. Every pulse entering the circuit sets off the switching

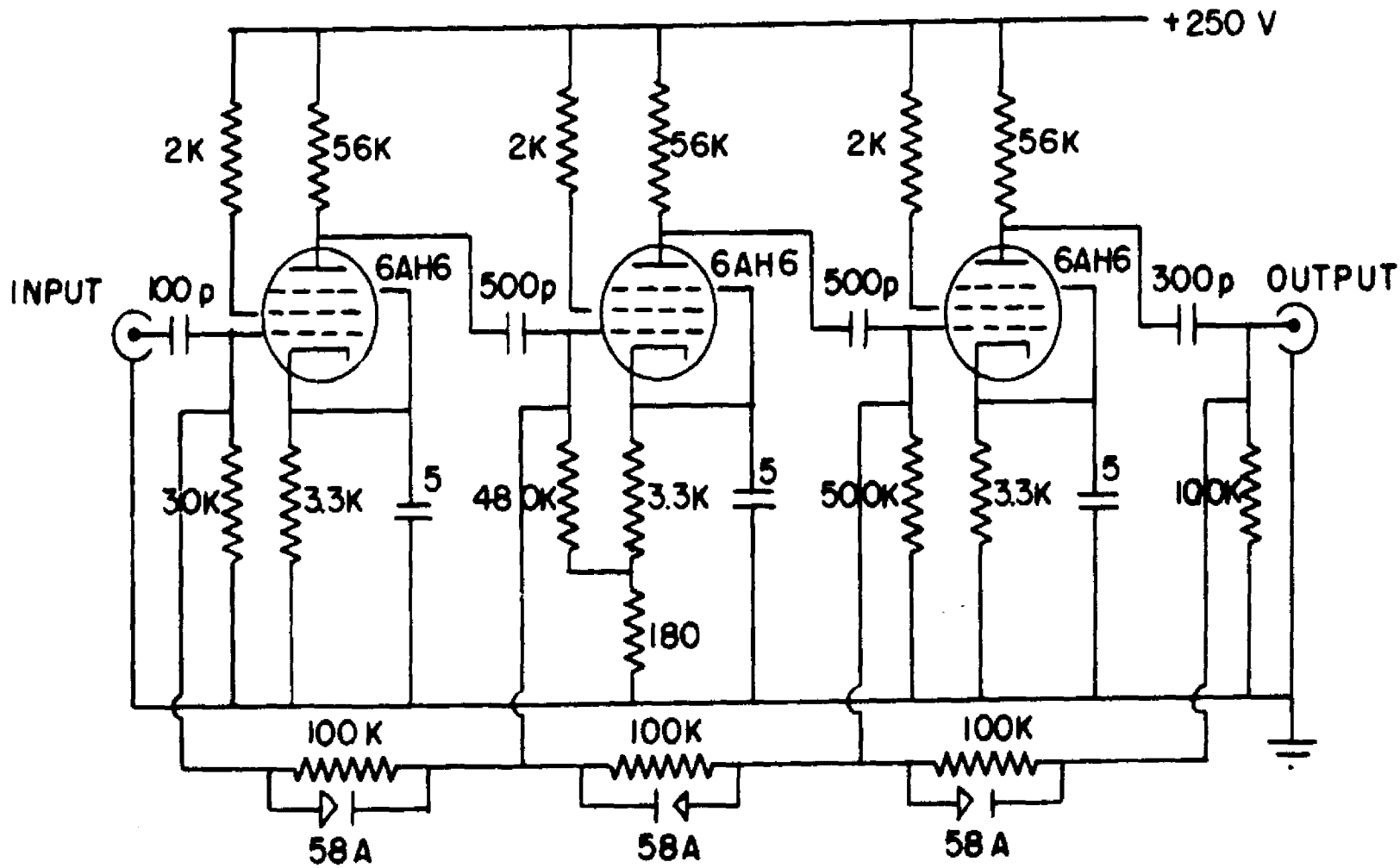


FIGURE 7 POLARIZED PULSE AMPLIFIER

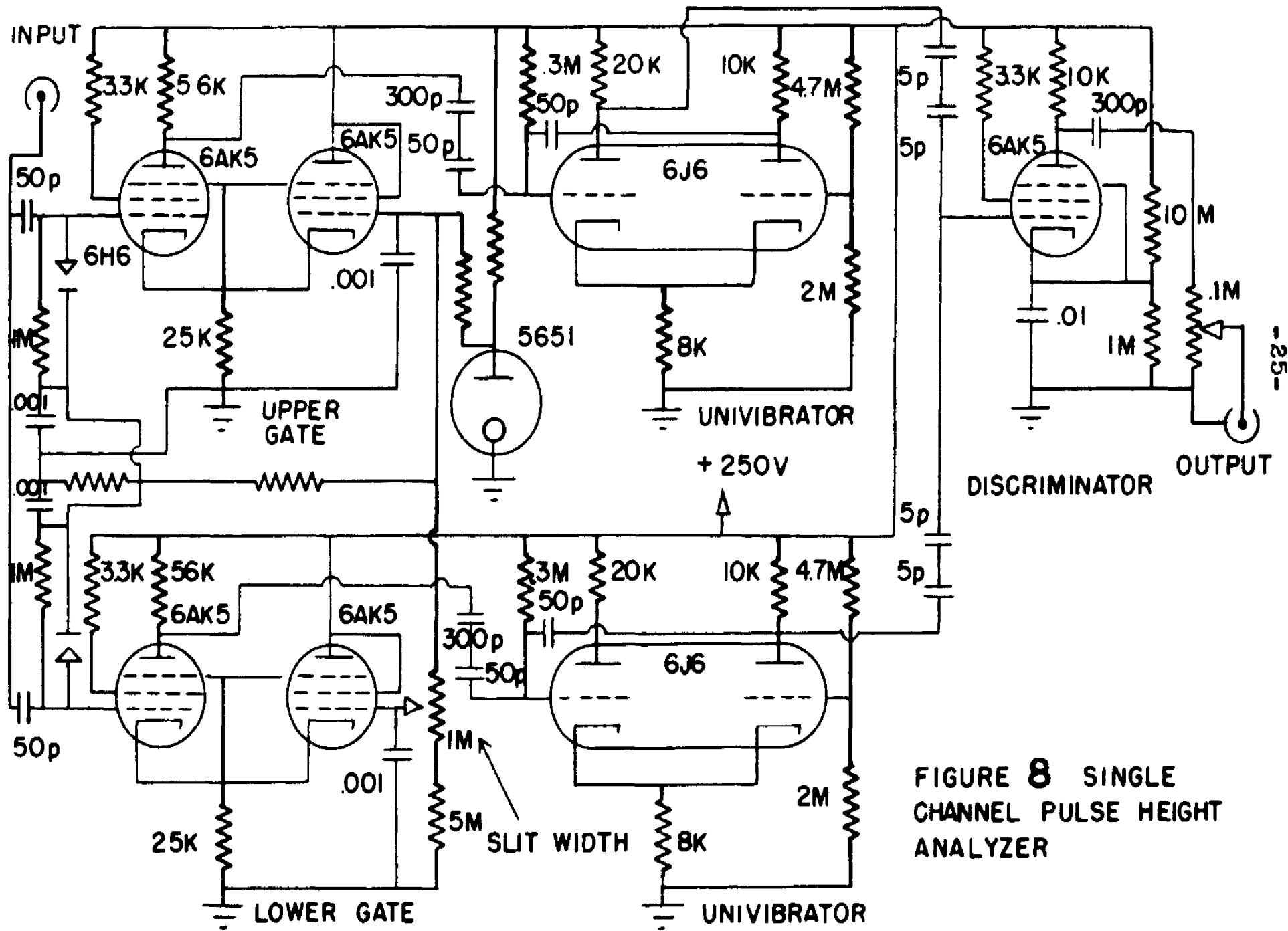


FIGURE 8 SINGLE
 CHANNEL PULSE HEIGHT
 ANALYZER

action which is fed back by means of 50 mmf capacitors. In case of the lower gate, the 2 microsecond pulse is taken off the second plate in form of a positive signal. In case of the upper gate, the pulse is taken off the first plate as a negative signal. Both pulses are fed into the control grid of the 6AK5 discriminator through very light coupling of 2.5 mmf. This is necessary to prevent retriggering among the univibrators themselves. The discriminator stage is biased considerably beyond cut-off. If a positive signal is received from the lower univibrator, the grid voltage is raised above cut-off and the pulse transmitted to the output. If a positive and a negative pulse are received together the grid voltage remains stationary and no signal is transmitted. The discriminator operates with sufficient integrating action so that the slight time difference which occurs between the start of the lower pulse and that of the upper pulse is not transmitted through the tube. The output pulses are differentiated and passed through an adjustable voltage divider that acts as output level setting. A picture of the instrument wiring is shown in Figure 9.

2f. Power Supply: - The power required to run the amplifier and the pulse height analyzer is taken from a full-wave rectifier regulated by two VR 150 voltage regulators in series. After regulation, the supply



Figure 9. Wiring of First Model Analyzer

is split into two sections which are isolated from each other by filter networks. One branch supplies the amplifier and gating circuits, while the other one supplies power to the univibrator and discriminator sections. The circuit diagram is shown in Figure 10.

3. Operation of the First Model

The first model scintillation spectrometer is operated by adjustment of the high voltage supply feeding the photomultiplier tube. The threshold of the gating circuits as well as the window width remain constant. This mode of operation has some distinct advantages over the alternative method of changing the threshold. In the first place, since the threshold voltage remains constant, the apparatus has an inherently higher stability. The window is constant, which automatically yields a constant instrument resolution percentage. The scanning range is very large because the voltage setting varies approximately as the logarithm of the gamma ray energy rather than being linearly proportional to it. The more modest design requirements of the apparatus have already been pointed out.

The model has been in operation for over one year. It is found necessary to let the instrument warm up for several hours, as initial drifts are considerable.

Once in stable operation, reproducible results are obtained. Nevertheless, calibrations are constantly

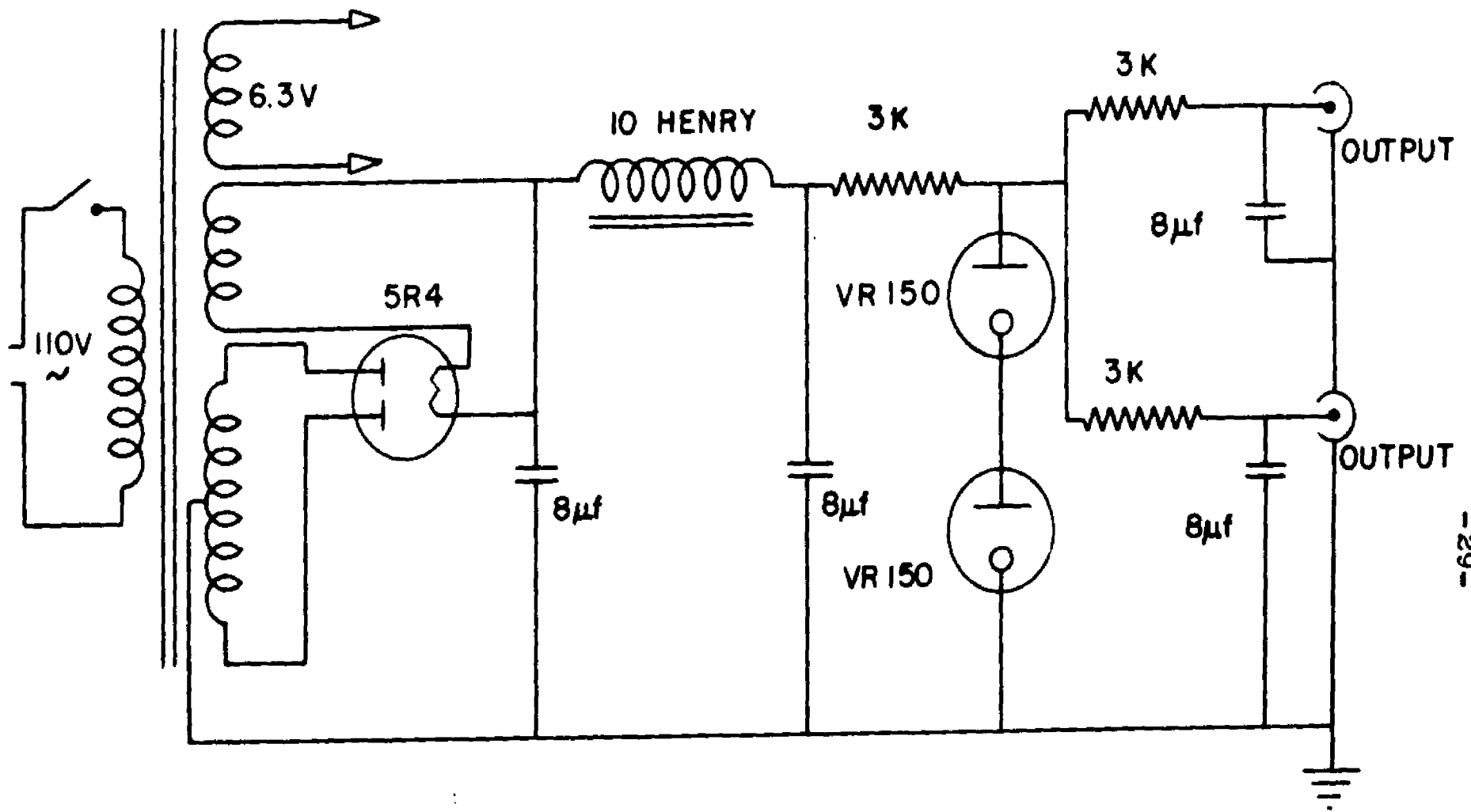


FIGURE 10 REGULATOR POWER SUPPLY

carried out. A typical calibration curve is shown in Figure 11. It is seen that the calibration is almost logarithmic, showing the typical expansion of the range at low energies.

A detailed study of the photopeaks and the Compton distribution has been carried out with the instrument to examine its behavior in the measurement of continuous energy electromagnetic radiation. The list of radioactivities for this research and the pertinent data are shown in Table I. The experimental curves obtained are shown in Figures 12 to 18. In these graphs, the energy scale is shown in terms of the dial voltage scale of the high voltage supply. The corresponding energies can be found from the calibration curve.

It may be concluded from the results that the principal energy spread of the photopeaks is due to fluctuations occurring in the multiplication of electrons in the initial stages of the photomultiplier. The Compton distribution may show one or more peaks depending on the crystal size and the type of shielding employed. It is observed that the Compton distribution varies with the energy of the gamma radiation and that some of the peaks are sufficiently sharp to be confused with photopeaks. This makes it necessary to proceed with caution in the interpretation of the experimental curves. The pulse height distribution on the photopeaks

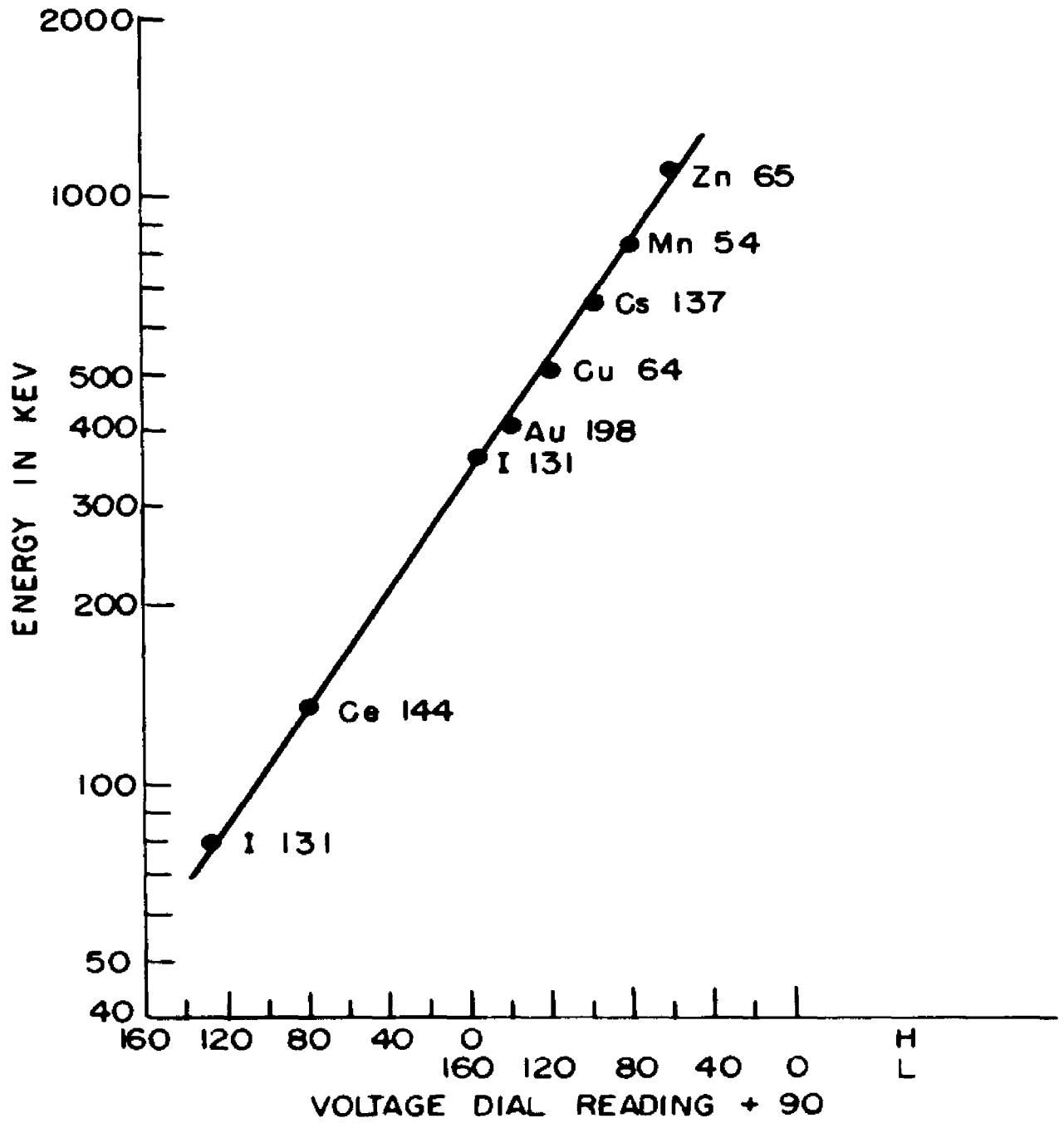


FIGURE 11 ENERGY CALIBRATION

TABLE I

Gamma Ray Emitters for Use in Calibration

<u>Isotope</u>	<u>Half-life</u>	<u>Gamma Ray Energies in kev</u>
Zn-65	250 days	1114, 511
Mn-54	310 days	835
Cs-137	37 years	662
I-131	8 days	637, 364, 284, 80
Cu-64	12.8 hours	511
Au-198	2.7 days	411
Ce-144	290 days	134

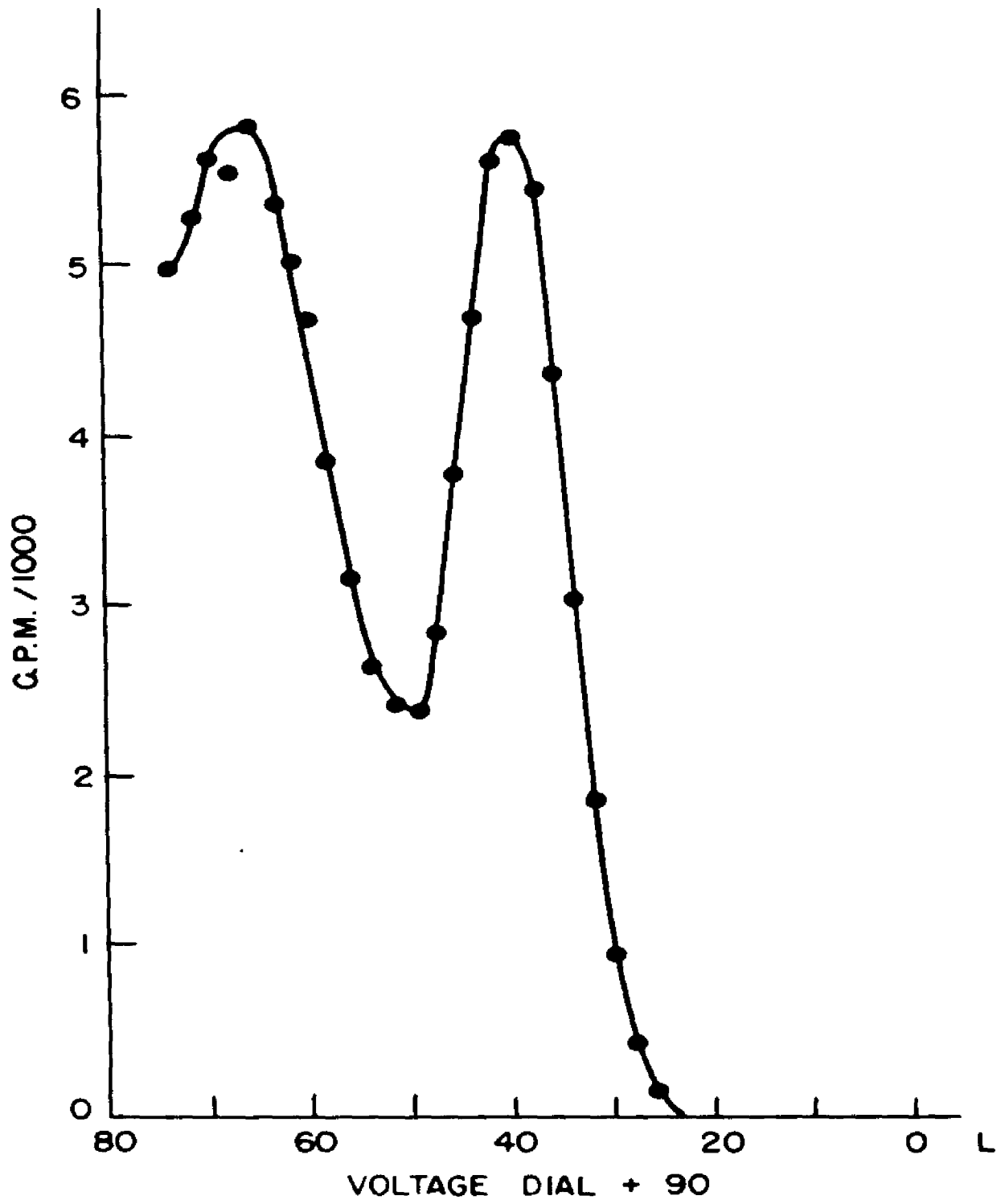


FIGURE 12 SPECTROGRAM OF Zn 65

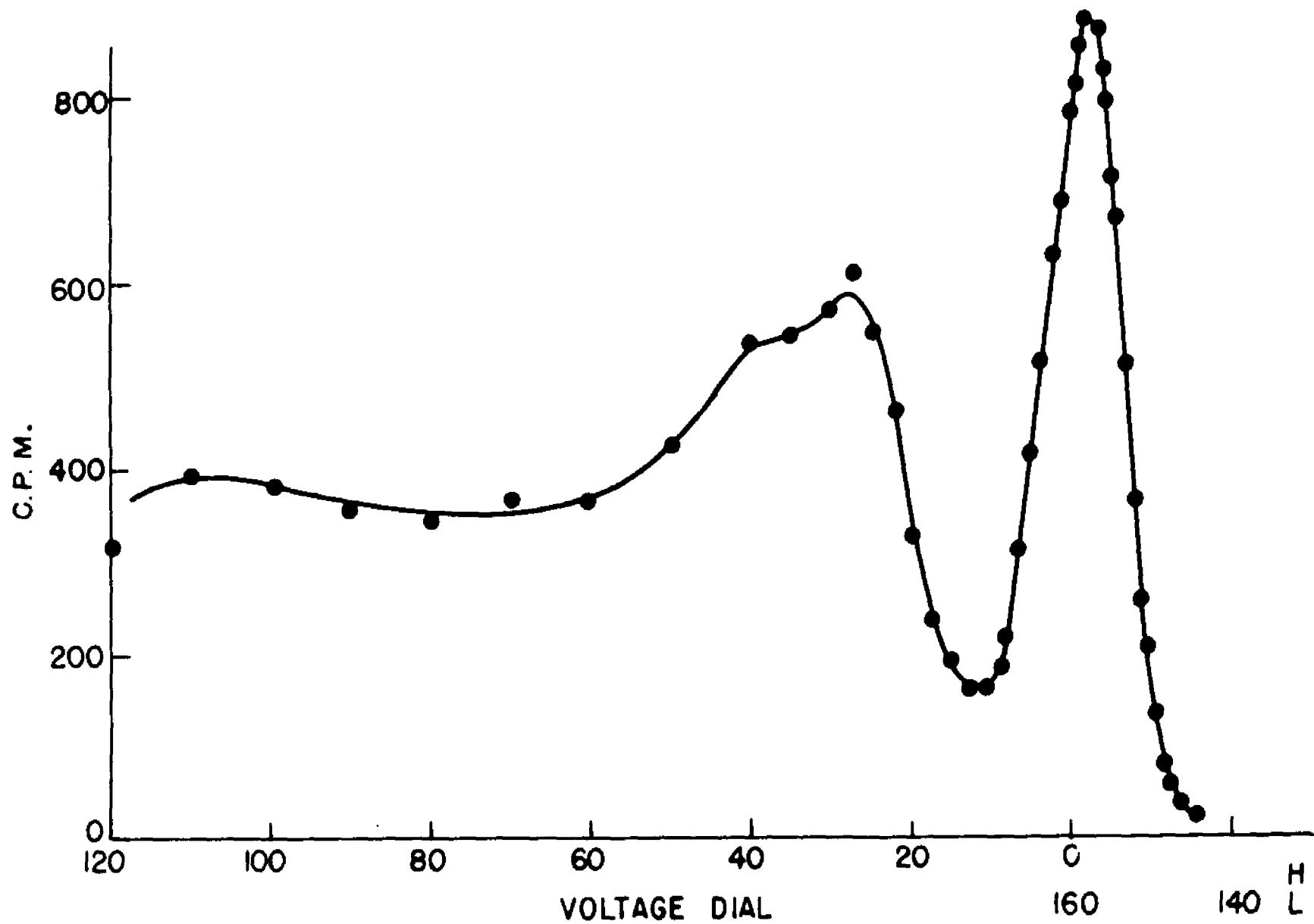


FIGURE 13 SPECTROGRAM OF Mn 54

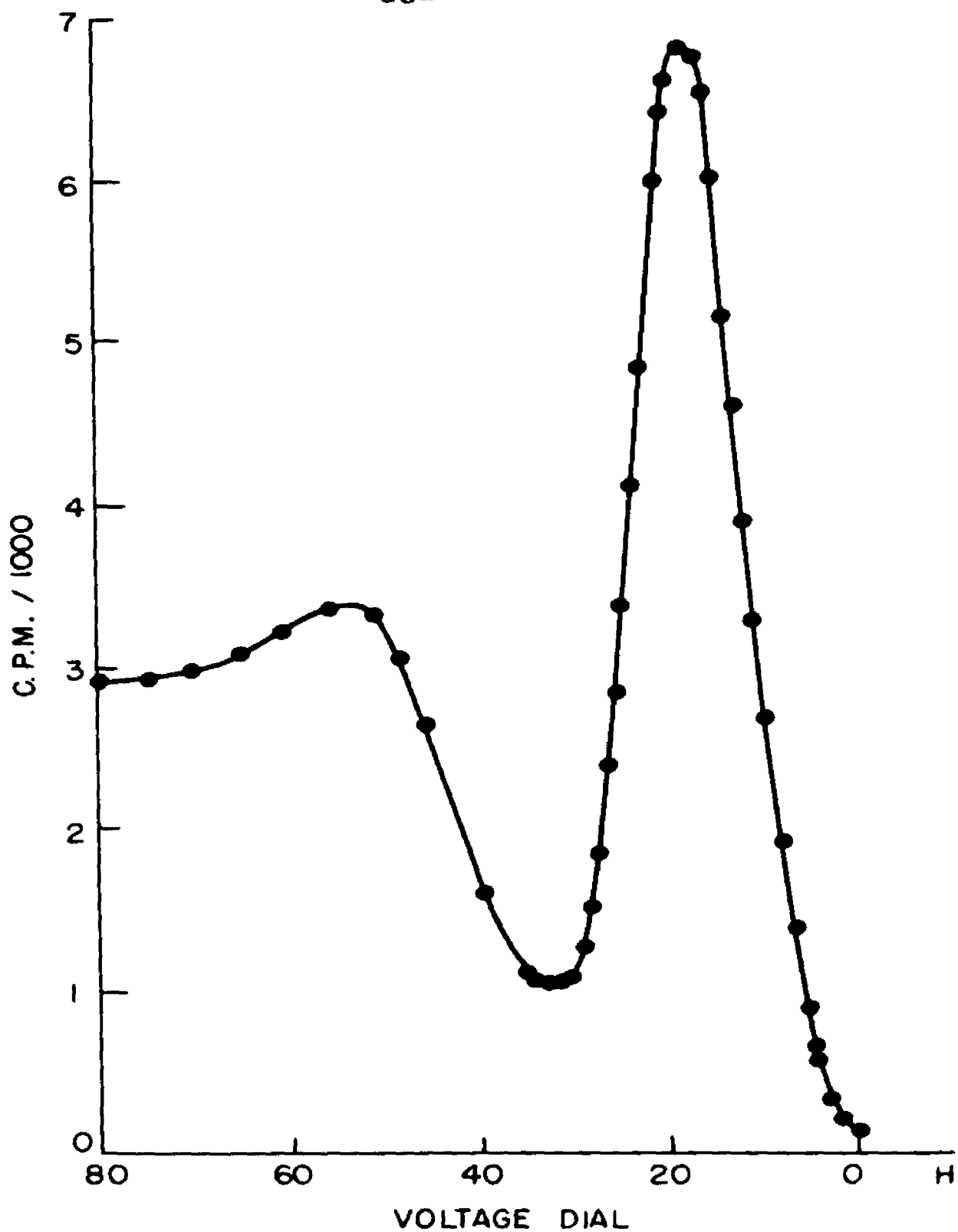


FIGURE 14 SPECTROGRAM OF Cs 137

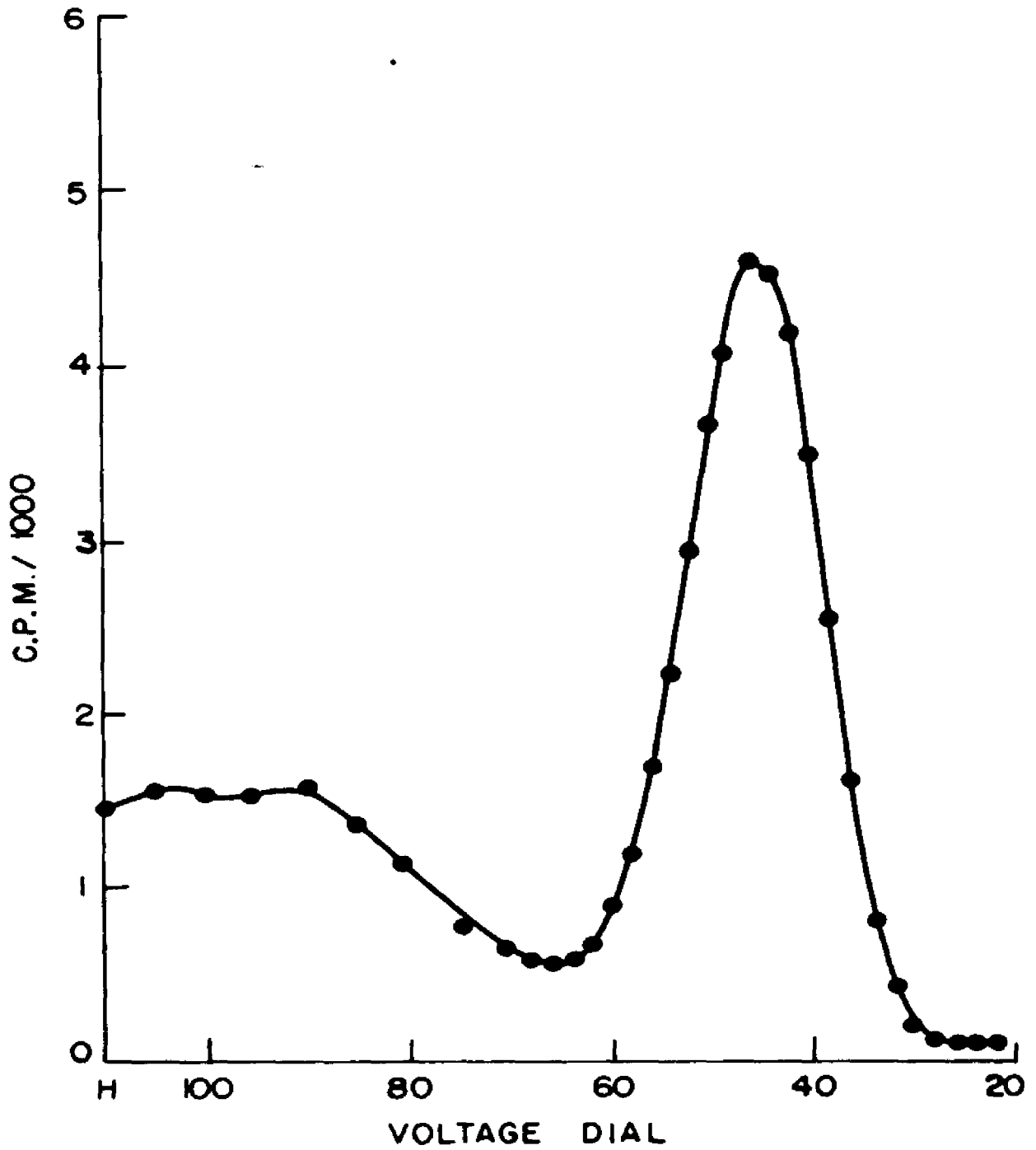


FIGURE 15 SPECTROGRAM OF Cu 64

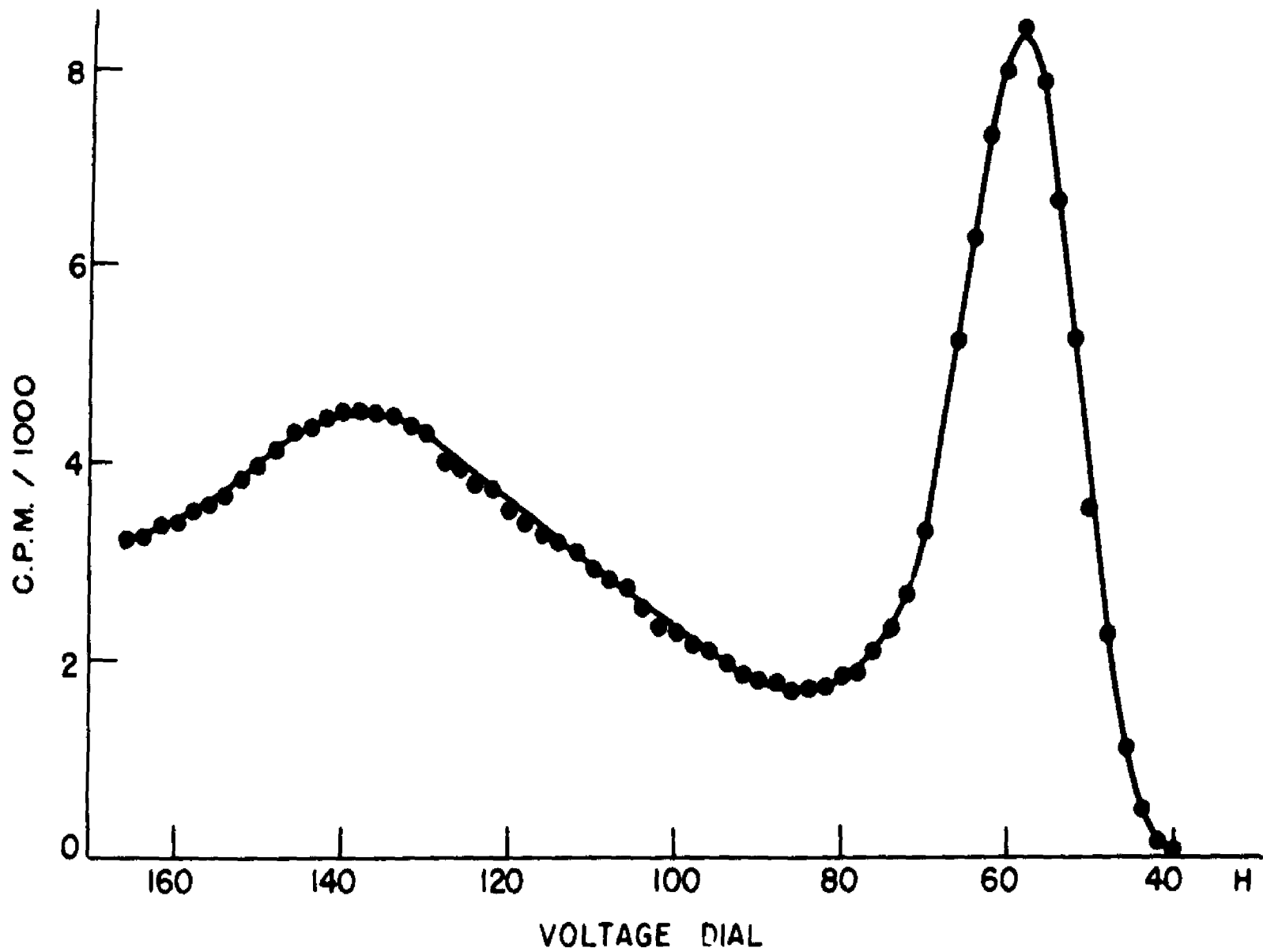


FIGURE 16 SPECTROGRAM OF Au 198

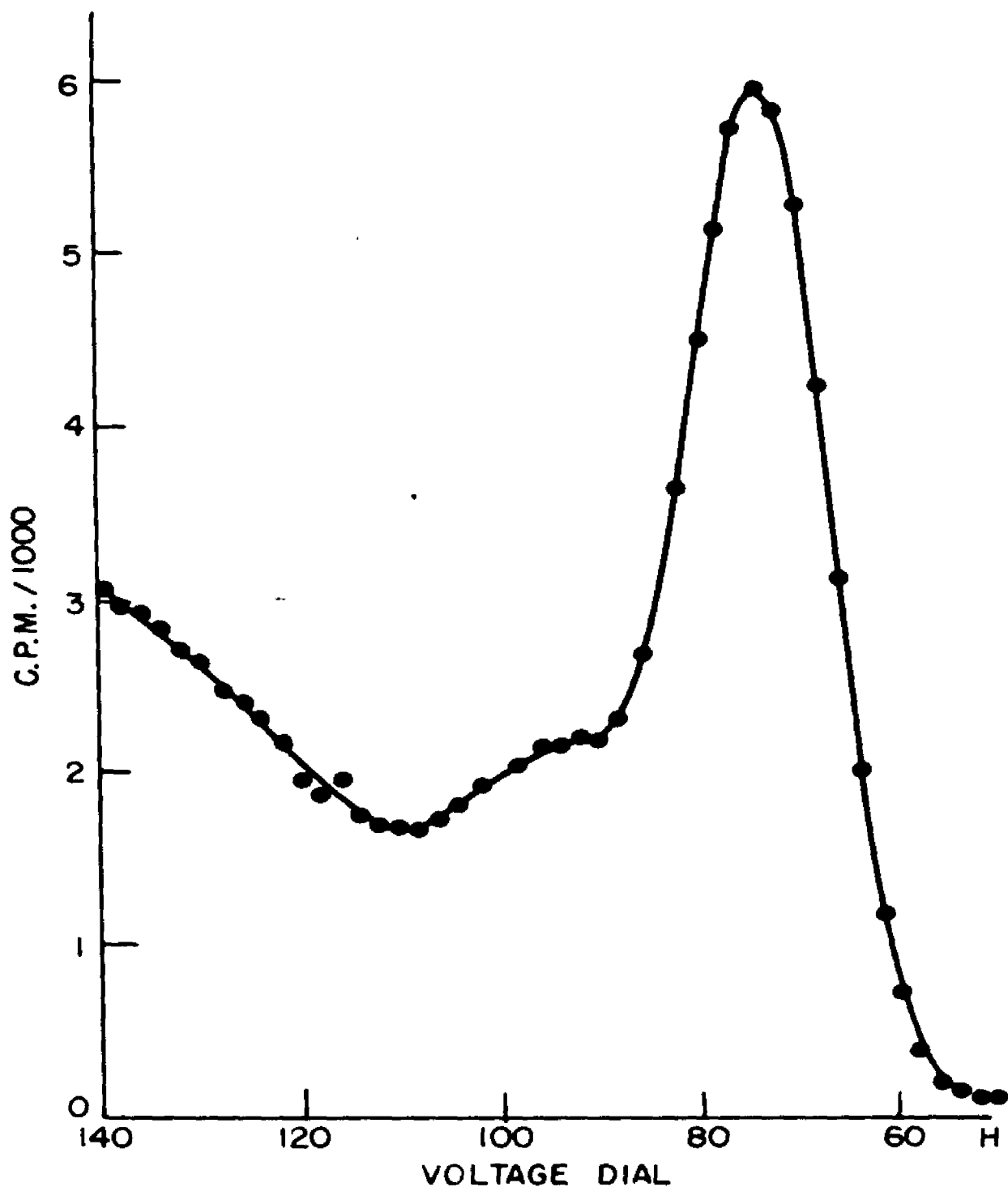


FIGURE 17 SPECTROGRAM OF THE I 131, 364 AND 284 KEV GAMMAS

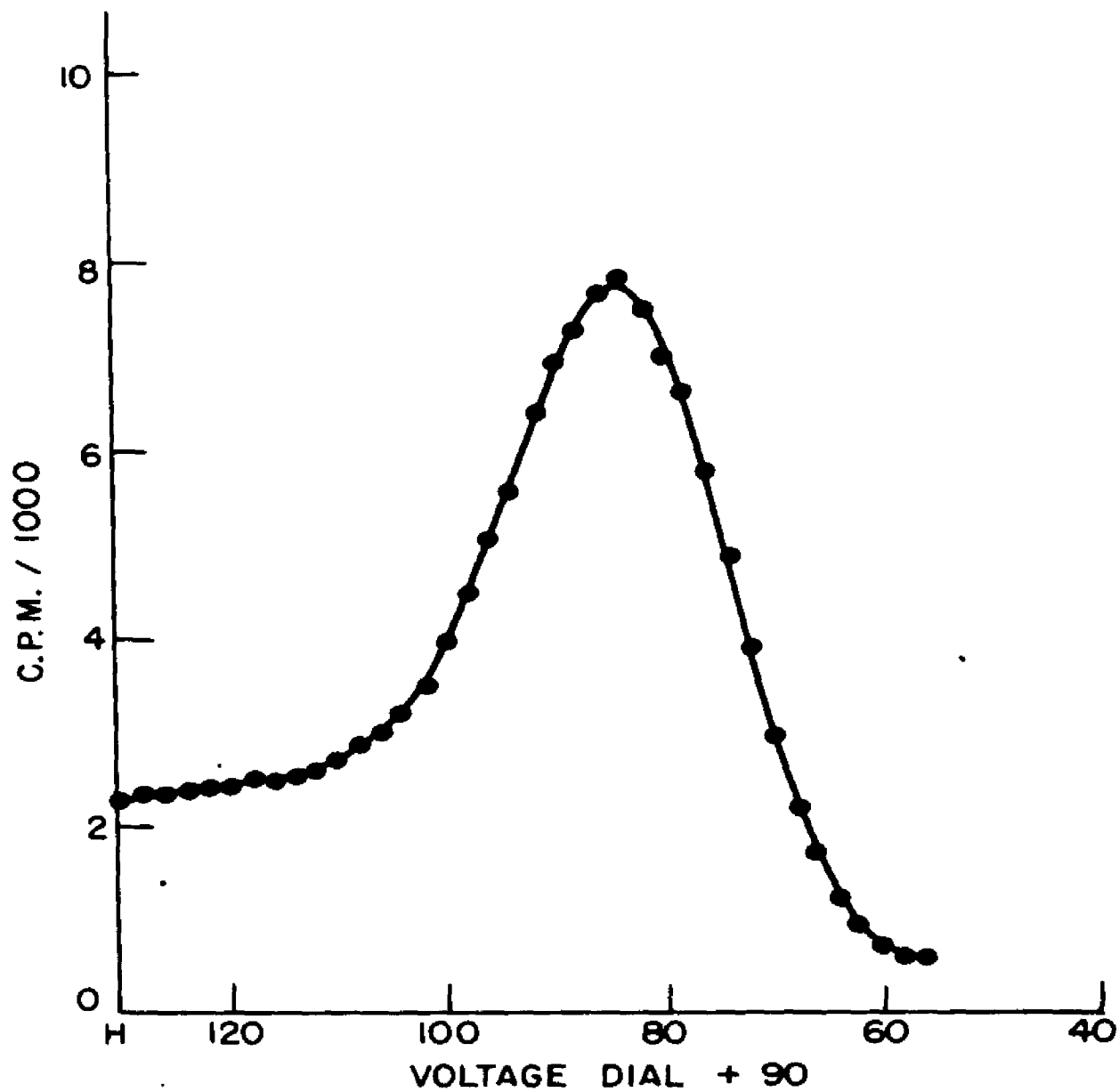


FIGURE 18 SPECTROGRAM OF Ce 144

is almost symmetrical, which makes it possible to analyze compound photopeaks even if they are not resolved completely by the natural resolving power of the instrument. This condition is shown in Iodine-131 in Figure 17, and in unpurified Barium-133 in Figure 19. It can also be observed that the Compton distribution is reduced to tolerable levels below the energy of annihilation radiation. The low energy peaks in Ba-133 and Ce-144 show almost no Compton distribution at all.

4. Design of the Second Model Scintillation Spectrometer.

Shortly after the first model had been in operation, preliminary plans were drawn up to design an improved instrument. Certain features were to be incorporated aside from technical improvements. The instrument was to be self-contained, stable in operation, to be operated either logarithmically or linearly, easily adjustable so that it could be operated by persons not familiar with its construction.

Among the technical improvements, it was to contain the largest available crystal, factory mounted and hermetically sealed. An amplifier was to be designed for linear amplification of pulses up to one hundred volts in amplitude. The analyzer was to incorporate a "window" amplifier, and discriminating

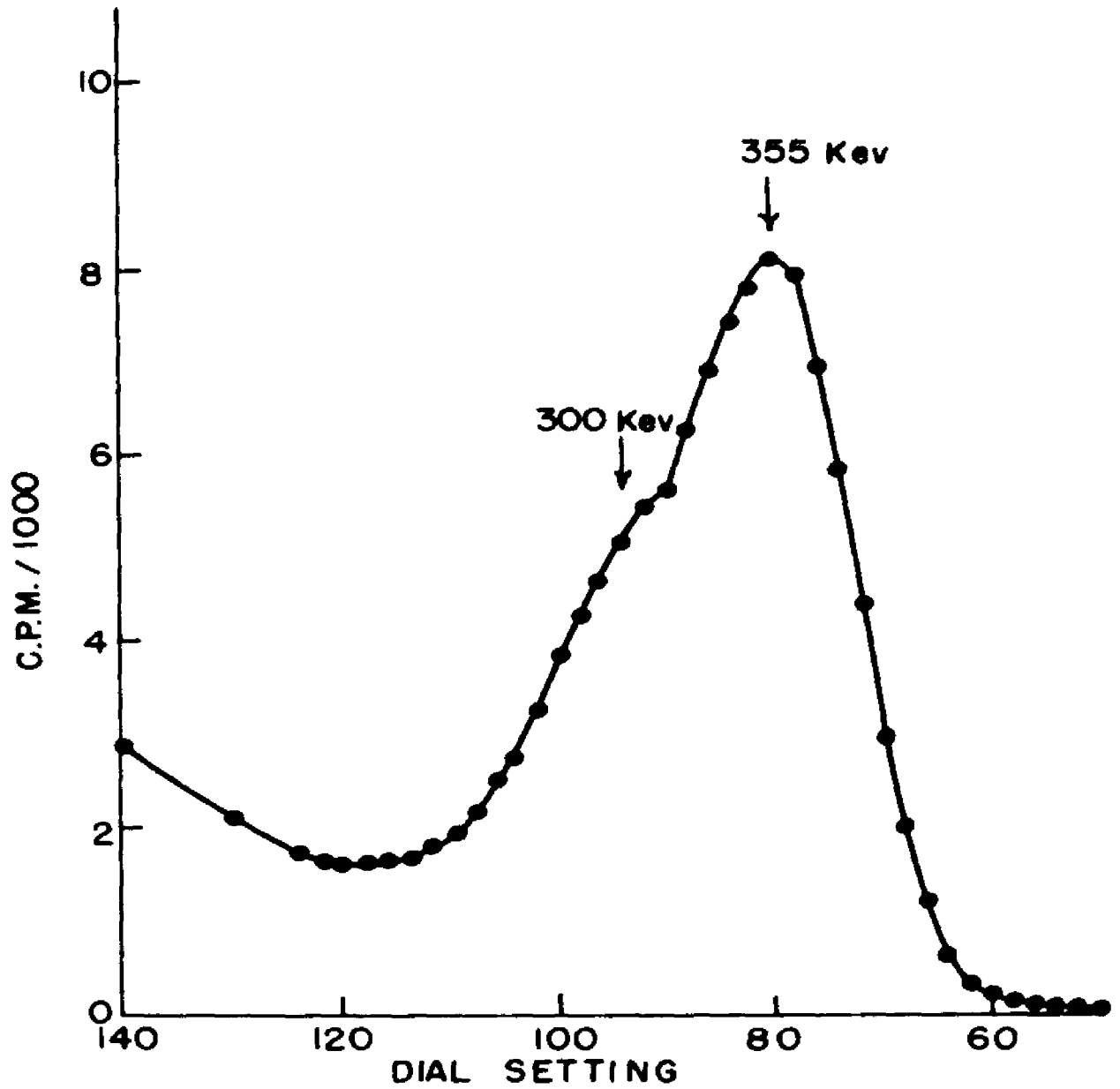


FIGURE 19 SCINTILLATION SPECTROGRAM OF BARIUM 133

circuit making use of the gated-beam tube, type 6BN6, with a transfer characteristic whose discontinuity at the conduction point is exceptionally sharp. Another feature in the design of the base-line discriminator was to be a constant current tube for discriminator stabilization against instantaneous drift due to the accumulation of excessive charge.

4a. Crystal Mounting and Photomultiplier Base:-

The scintillator is a mounted crystal of thallium activated sodium iodide 1.5 inches in diameter and one inch long, purchased from the Larco Nuclear Instrument Company. The conduction of light from the crystal window to the photo-cathode is aided by a film of silicon grease between the glass surfaces. The photomultiplier mounting and voltage dividing network is identical with the earlier model except that one watt resistors are used. It has been observed that these are freer from spurious noise under high voltage strain than one-half watt resistors.

4b. High Voltage Supply:- The high voltage supply is similar to the previous model in that it consists of a half-wave rectifier. The regulation is improved by the use of an electronic feedback regulating system instead of a string of voltage regulating tubes. The design is kept as simple and elementary as possible in order to insure long time stability. A voltage divider

feeds a correction signal into the control grid of a 6AG5 pentode, whose cathode is kept at a constant potential by means of a voltage regulator tube. The current needed to operate the voltage regulating tube is taken from a regulated 300 volt supply, which ordinarily supplies power to the amplifier and the analyzer. The amplified signal is taken from the plate of the 6AG5 and fed to the grid of a 7B4, which acts as variable series resistor in the high voltage line. The output voltage is put into a potentiometer circuit consisting of a 300,000 ohm helipot and fixed resistors in series. The adjustment of the helipot is brought out on the front panel so that high voltage scanning is possible for logarithmic operation of the instrument. A voltmeter in parallel with the photomultiplier indicates the applied voltage at any time. The circuit diagram is shown in Figure 20.

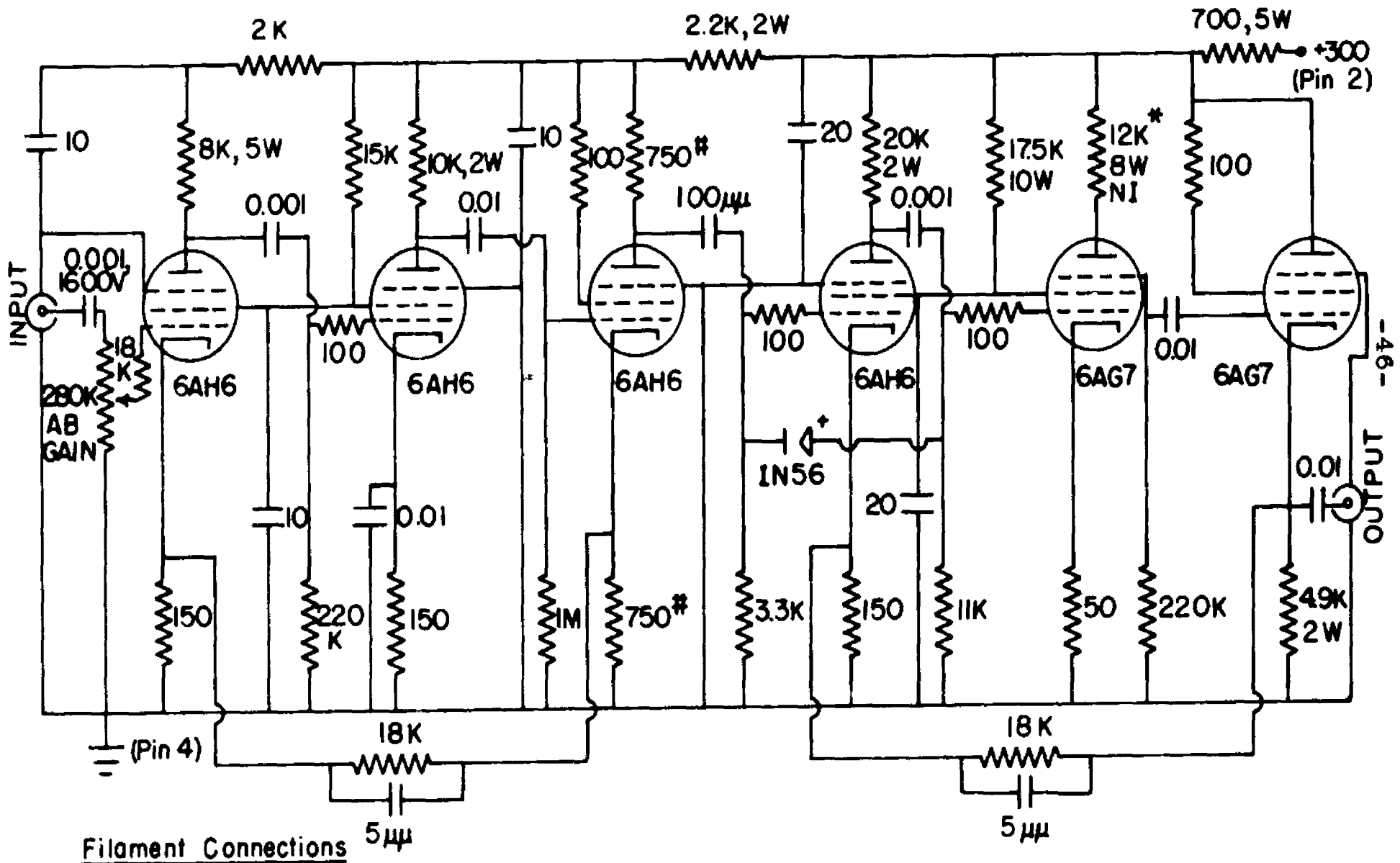
4c. The Linear Pulse Amplifier: - The linear amplifier consists of two separate feed-back loops coupled through a phase-inverter stage and leading out through a cathode-follower. The first feed-back loop consists of two stages of resistance coupled 6AH6 tubes. The feedback signal is taken from the cathode resistor of the phase inverter stage. This stage also provides decoupling between the first and the second feed-back loops. In the construction of the amplifier,

the two feed-back loops are electrically shielded from each other. The second feed-back loop consists of a resistance coupled 6AH6 stage followed by a resistance coupled 6AG7 stage. The output is taken to a cathode-follower which also supplies the feed-back signal for the second loop. A crystal diode in the last 6AH6 stage suppresses overshoot from overloading pulses. The circuit diagram for the amplifier is shown in Figure 21. A picture of the chassis is shown in Figure 22. It is seen that the amplifier chassis is separately constructed from the main chassis of the analyzer. This is done to facilitate repairs in case of a breakdown. A small electric fan mounted on the main chassis provides cooling air to insure that the temperature of the crystal diode does not exceed the tolerance of 50 degrees C.

4d. Pulse Height Analyzer: - The pulse height analyzer designed for use with this instrument is essentially based on the circuit diagram of the Los Alamos analyzer designed by Johnstone (13). It is modified to generate negative rather than positive output pulses.

The base line discriminator and expander amplifier diagrams are shown in Figure 23. The base line discriminator is similar in design to the upper and lower gate circuits of the first model. The constant-current

LINEAR AMPLIFIER



6AH6's: Pin 3 to gnd, Pin 4 to B
 6AG7's: Pin 2 to gnd, Pin 7 to B

FIGURE 21

* 4- 3.3K, 2W in series
 # Matched



Figure 22. (Top) Linear Amplifier Chassis with Photomultiplier. (Bottom) Amplifier Mounted on analyzer Chassis.

WINDOW AMPLIFIER

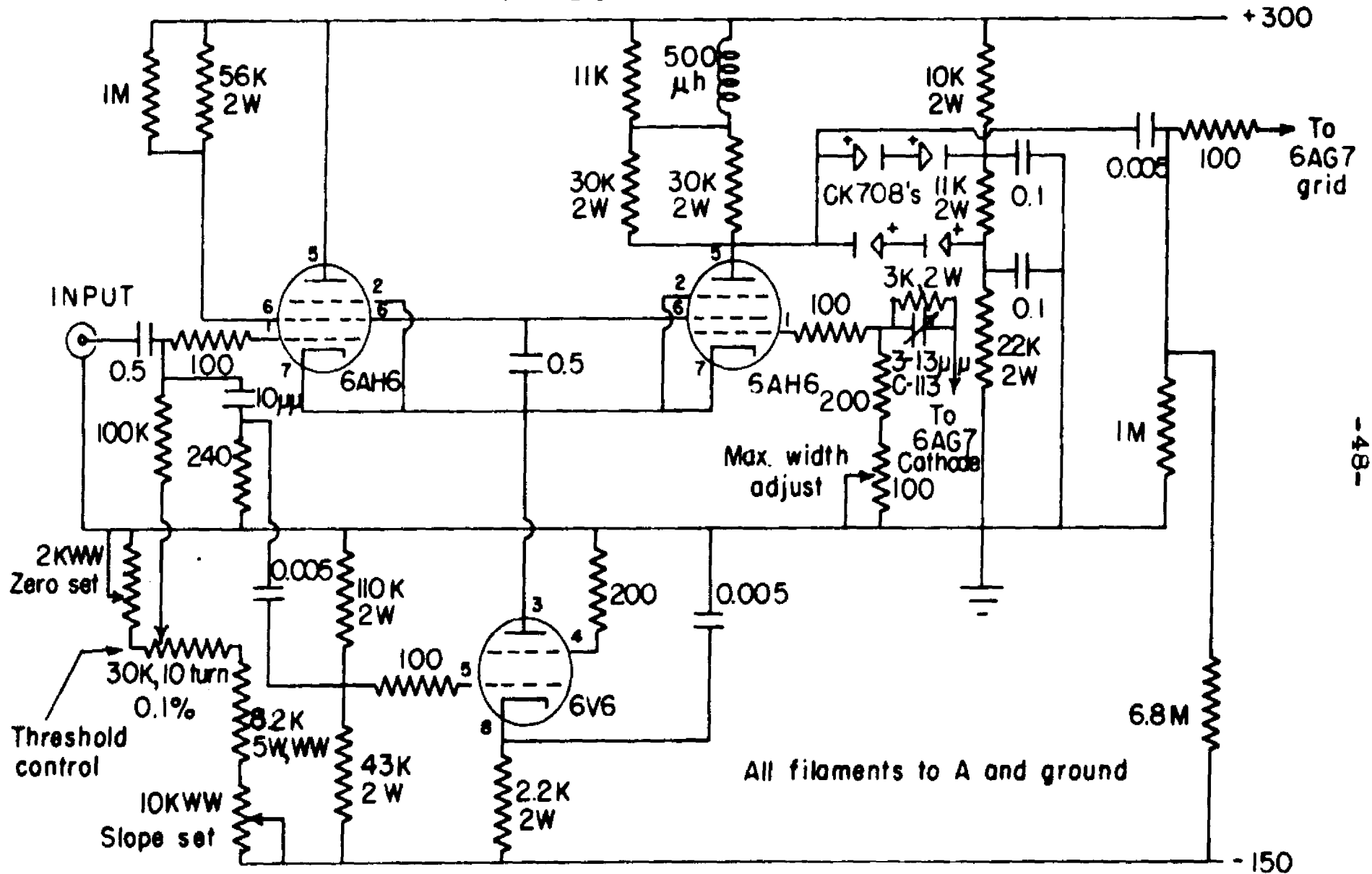


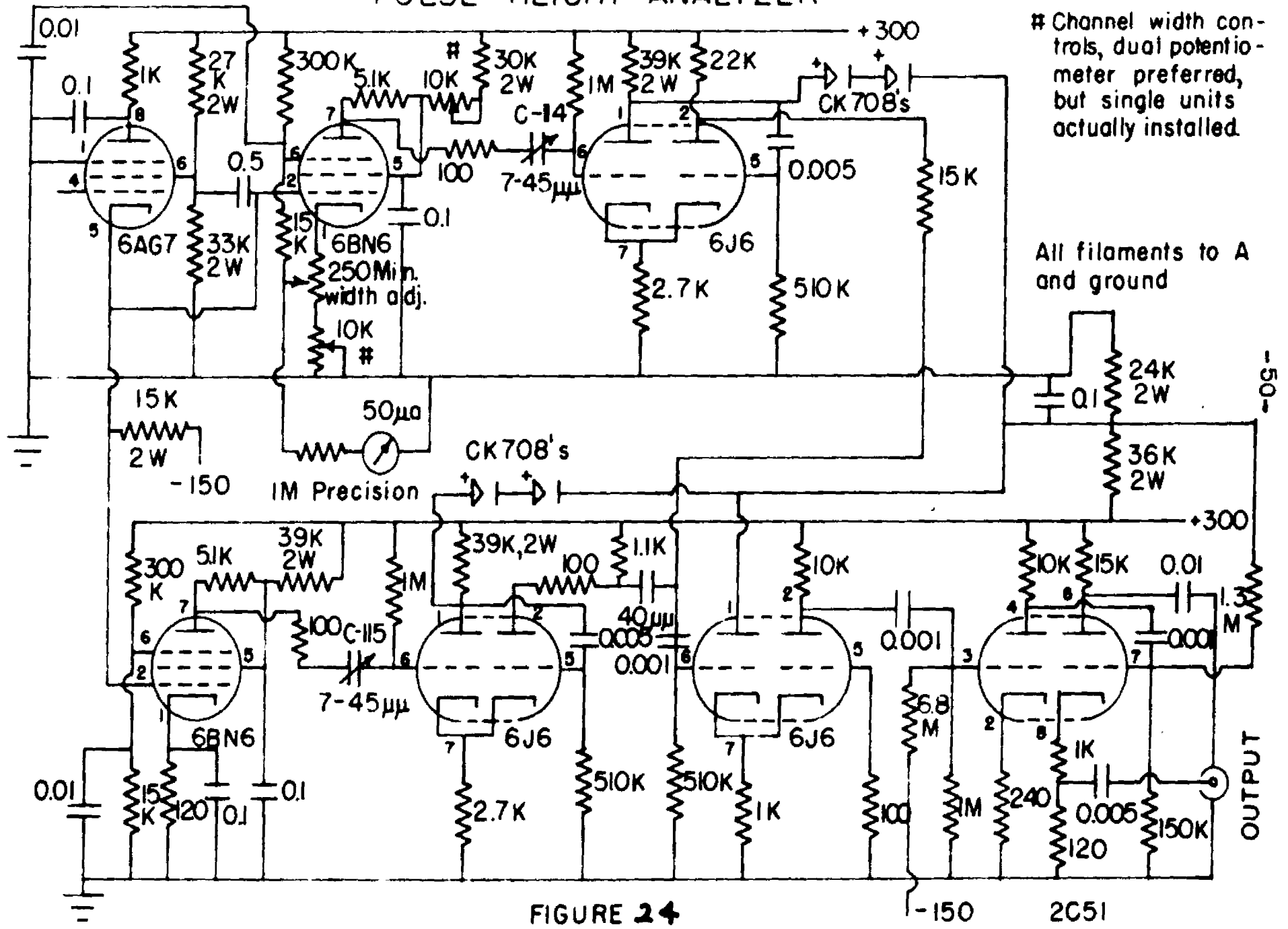
FIGURE 23

tube in the cathode circuit of the base line discriminator derives its signal from the compensating RC network leading to the control grid. This increases its plate current instantaneously by an amount equal to the grid-cathode displacement current. Any disturbing accumulation of charge at the cathodes is thereby prevented. The threshold setting is adjustable by means of a helical potentiometer between zero and one hundred volts.

The portion of the pulse which is passed by the discriminator is amplified about ten times by means of the 6AG7 pentode, which constitutes the window amplifier. A limiter network incorporating crystal diodes is provided for the prevention of over and undershoot due to excessively high pulses.

A detailed diagram of the level selectors and anticoincidence circuits is shown in Figure 24. A lower-level discriminator, and an upper-level, or window width, discriminator, are both connected to the output of the expander amplifier. Type 6BN6 gated-beam tubes are employed in both sections. The window width is determined by the difference in potential at which the tubes operate. Two synchronized potentiometers raise the cathode and plate by equal voltages, so that the window width is independent of the tube characteristics. A voltmeter, which indicates the channel width setting, is incorporated in the circuit.

PULSE HEIGHT ANALYZER



Pulses that actuate the 6BN6 tubes are passed through to trigger univibrators set to generate pulses of 3 microsecond duration. The pulse from the lower gate is differentiated by means of an RC network. The signals are mixed and drive the anticoincidence and amplifying circuit employing a 6J6 duo-triode. When both univibrators operate, the signal never goes below the base line since the upper level pulse predominates over the differentiated pulse from the lower level univibrator. If the lower gate operates alone, a reverse signal is generated at the end of the pulse. It is this part of the pulse alone, which passes through the 6J6 and is amplified. A phase inverter and cathode follower, type 2C51, shapes the pulse and provides a low output impedance. A picture of the chassis is shown in Figure 25.

4e. Regulated Power Supplies: - The power required to operate the pulse amplifier and the pulse height analyzer is taken from a full-wave rectifier, which is regulated by means of a two tube difference amplifier employing a 5651 voltage reference tube. The negative voltage required for the pulse height analyzer is obtained from a conventional stabilized negative power supply. The circuit diagrams are shown in Figures 26 and 27. The wiring of the instrument is shown in Figure 28. Figure 29 gives a front view of the entire

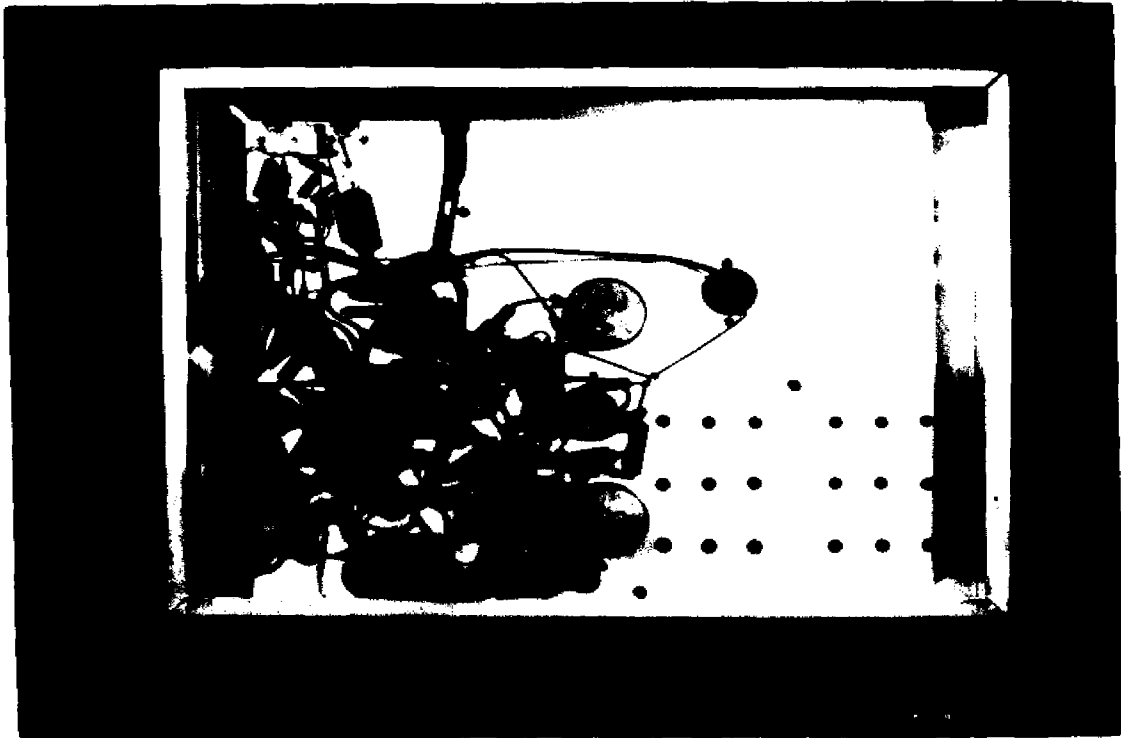


Figure 25. Second Model Pulse Height Analyzer
Chassis

300 VOLT SUPPLY

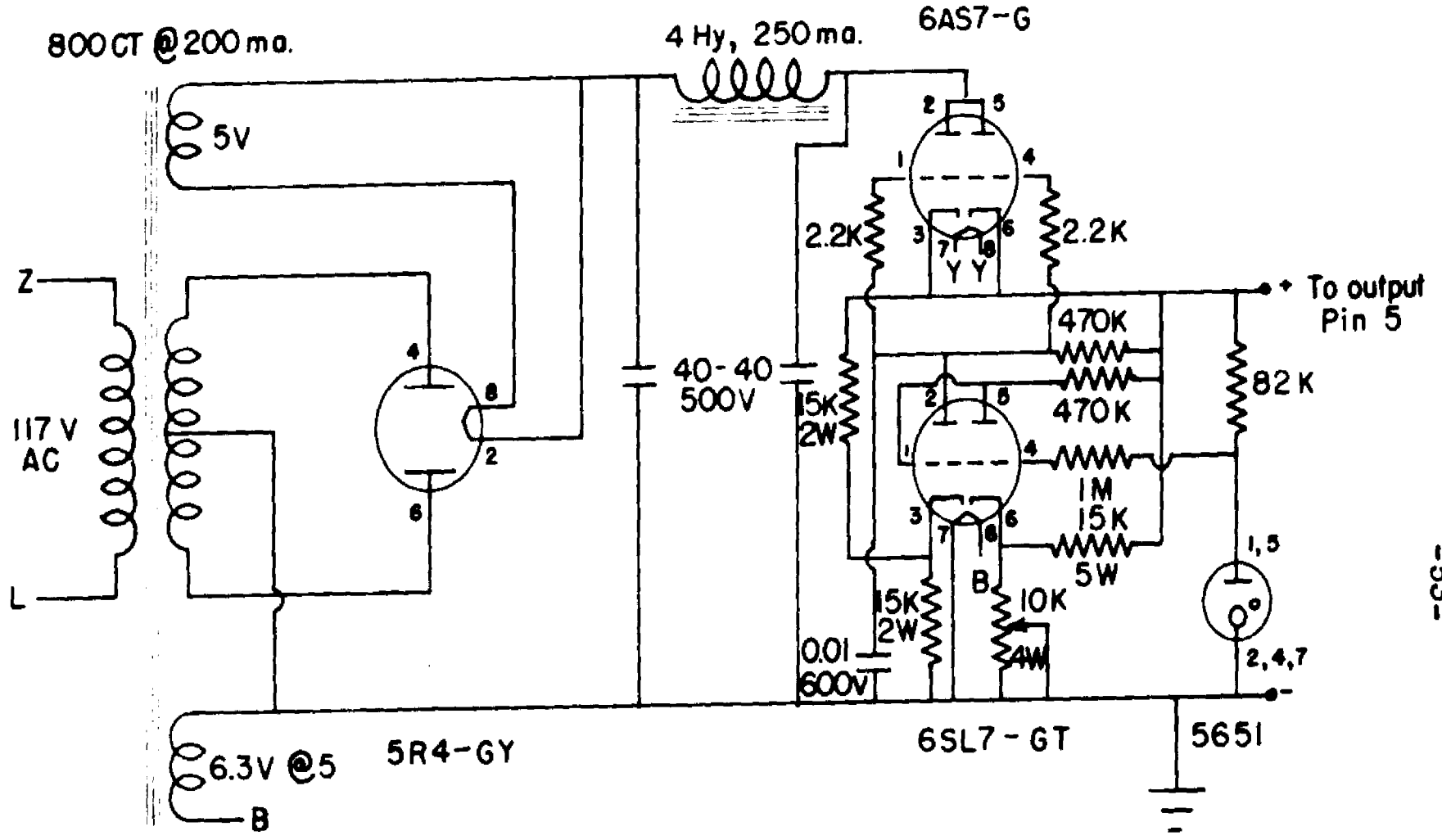


FIGURE 26



Figure 23. Wiring of Power Supplies

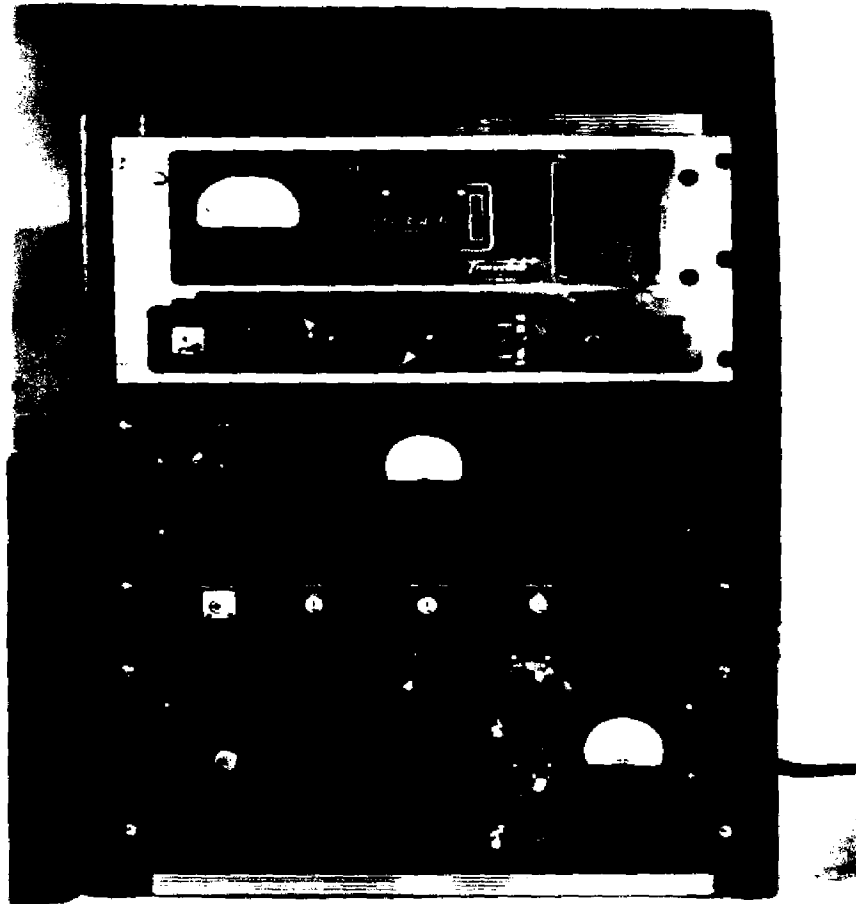


Figure 29. Front View of Panel

scintillation spectrometer assembly. The top third is a Tracerlab decade scaler. The power supplies are located behind the center panel, while the amplifier and pulse height analyzer are mounted behind the lowest panel.

5. Operation of the Second Model

5a. General Operation: - The final model precision scintillation spectrometer can be operated either logarithmically or linearly. In all the following experiments, the instrument is operated linearly. This is based on the circumstance that in the theory of radiative electron capture, the formulae are worked out on the basis of equal energy increments rather than on constant percentage increments.

Similar to the first model, it is necessary to let the instrument warm up for several hours in order to eliminate short term drifts. After that time, however, the operation is exceptionally stable. In fact, calibrations can be reproduced to within 0.5 per cent after a period of one month. The channel width is set at 2 volts in all measurements, and the actual channel width is measured empirically by means of a pulse generator as shown in Figure 30. The correction for this variation is taken into account automatically in the method of total efficiency correction employed in the measurements. The total empirical half-width at various

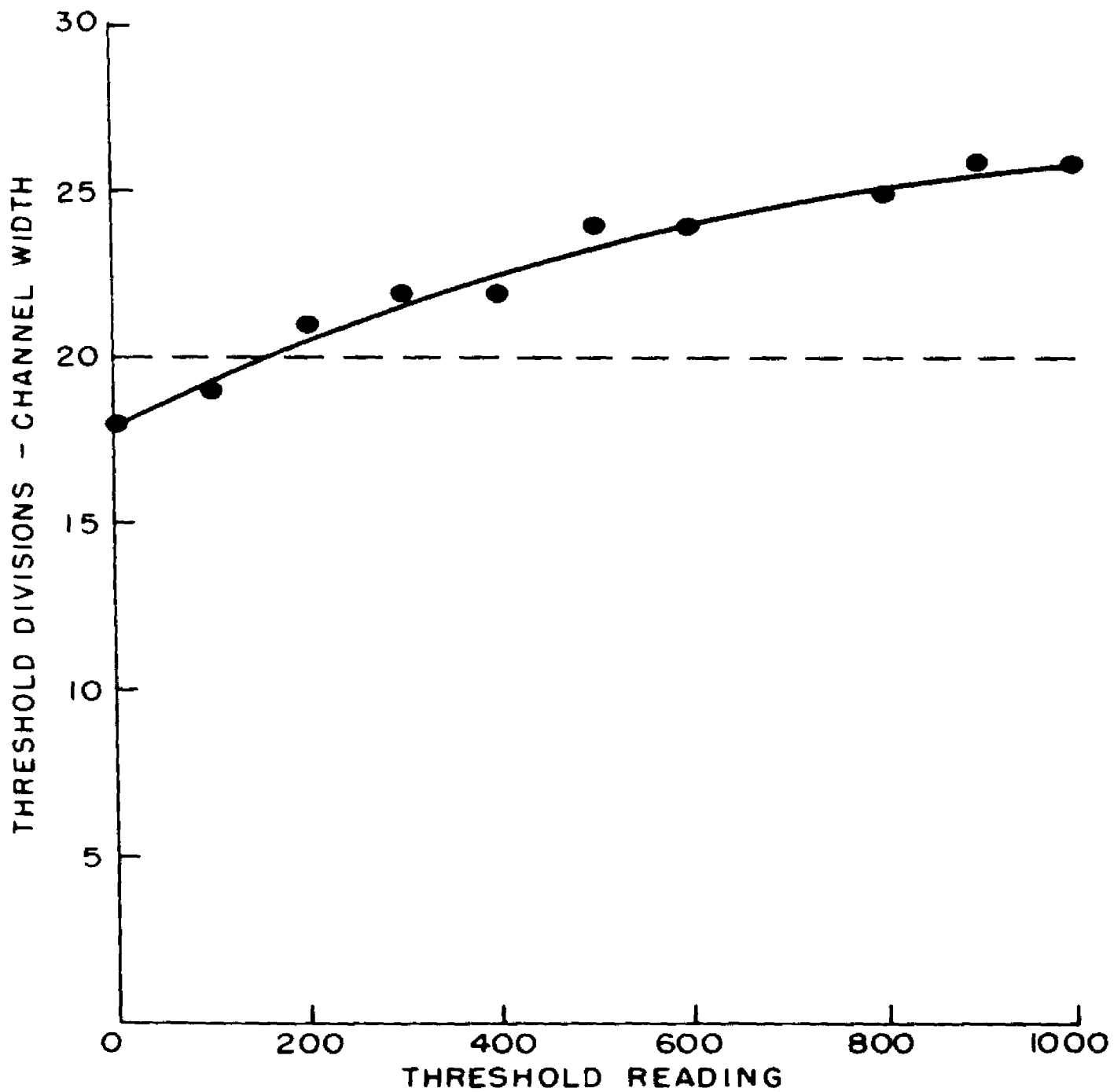


FIGURE 30 EMPIRICAL DETERMINATION OF CHANGE IN CHANNEL WIDTH AT A SETTING OF 2 VOLTS.

energies is shown in Figure 31.

5b. Calibration: - For calibration purposes, a number of radioactive sources are utilized which emit well known gamma radiation. These are listed in Table II, together with their half-lives and gamma ray energies. An energy calibration curve is shown in Figure 32. It is seen that the calibration is exactly linear in this range. The calibration curve does not go through (zero,zero) because of the bias potential on the grid of the first 6AH6. This bias potential is about three volts, or 30 dial divisions on the threshold scale, since each dial division corresponds to 0.1 volt threshold change.

5c. Overall Efficiency Determination: - The overall counting efficiency is needed for the proper analysis of continuous energy electromagnetic radiation. The determination of the efficiencies has been carried out empirically by means of calibrated gamma ray sources. The radioactivities concerned are listed in Table III. The calibration is based on the relative beta ray activity observed with a G.M. counter. Each beta ray activity is compared by absorption measurements with a standard source of Co-60 whose absolute disintegration rate is known.

The beta ray absorption data are shown in Figure 33. From the extrapolated activity at zero absorber

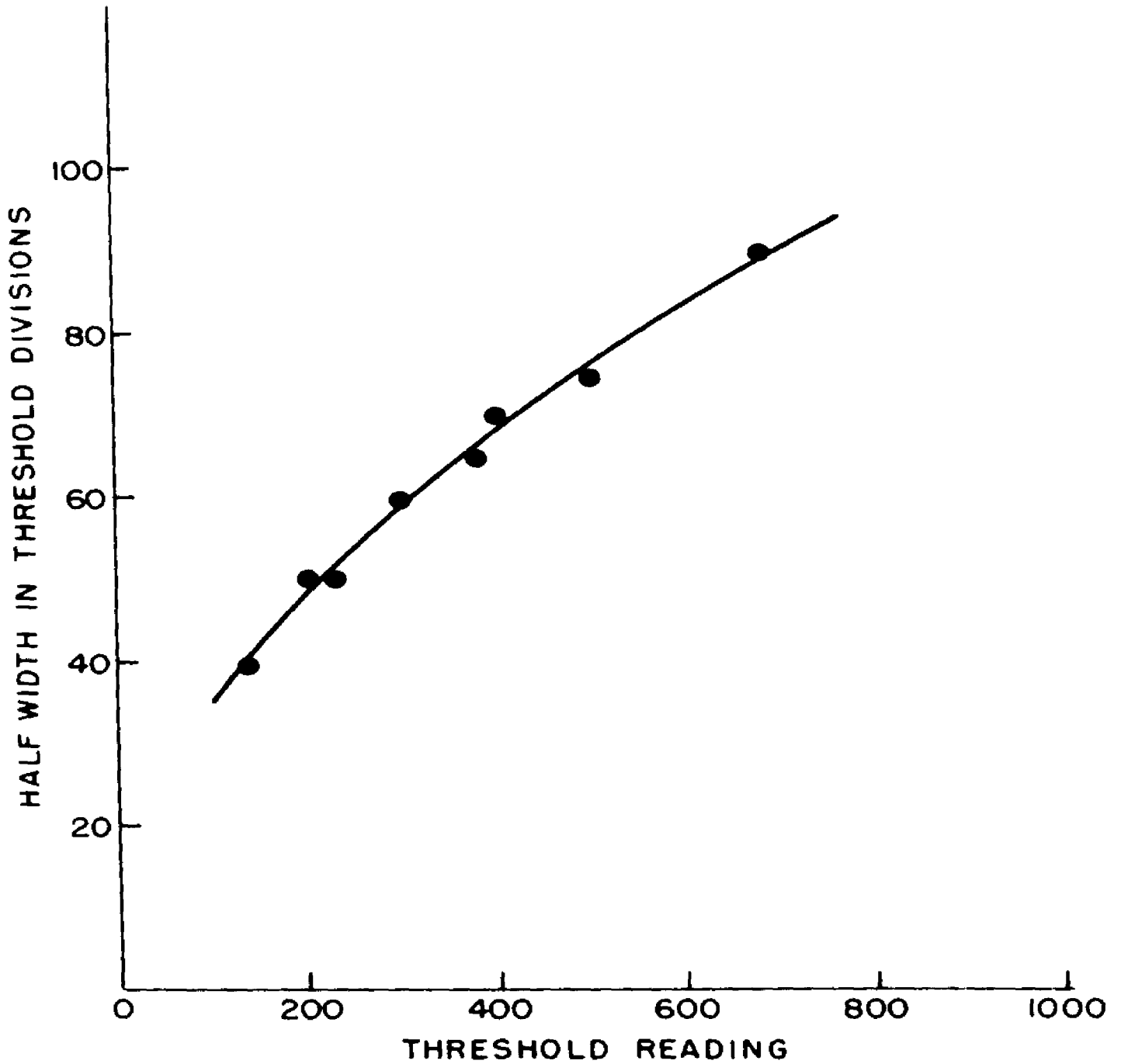


FIGURE 31 TOTAL HALFWIDTH FOR GAMMA RAYS

TABLE II

Gamma Ray Emitters Used for the
Energy Calibration

<u>Isotope</u>	<u>Half-life</u>	<u>Gamma Ray Energies in kev</u>
Co-60	5 years	1320, 1160
Zn-65	250 days	1114, 511
Mn-54	310 days	835
Cs-137	37 years	662
I-131	8 days	637, 364, 284, 80
Au-198	2.7 days	411
Hg-203	46 days	279, 69

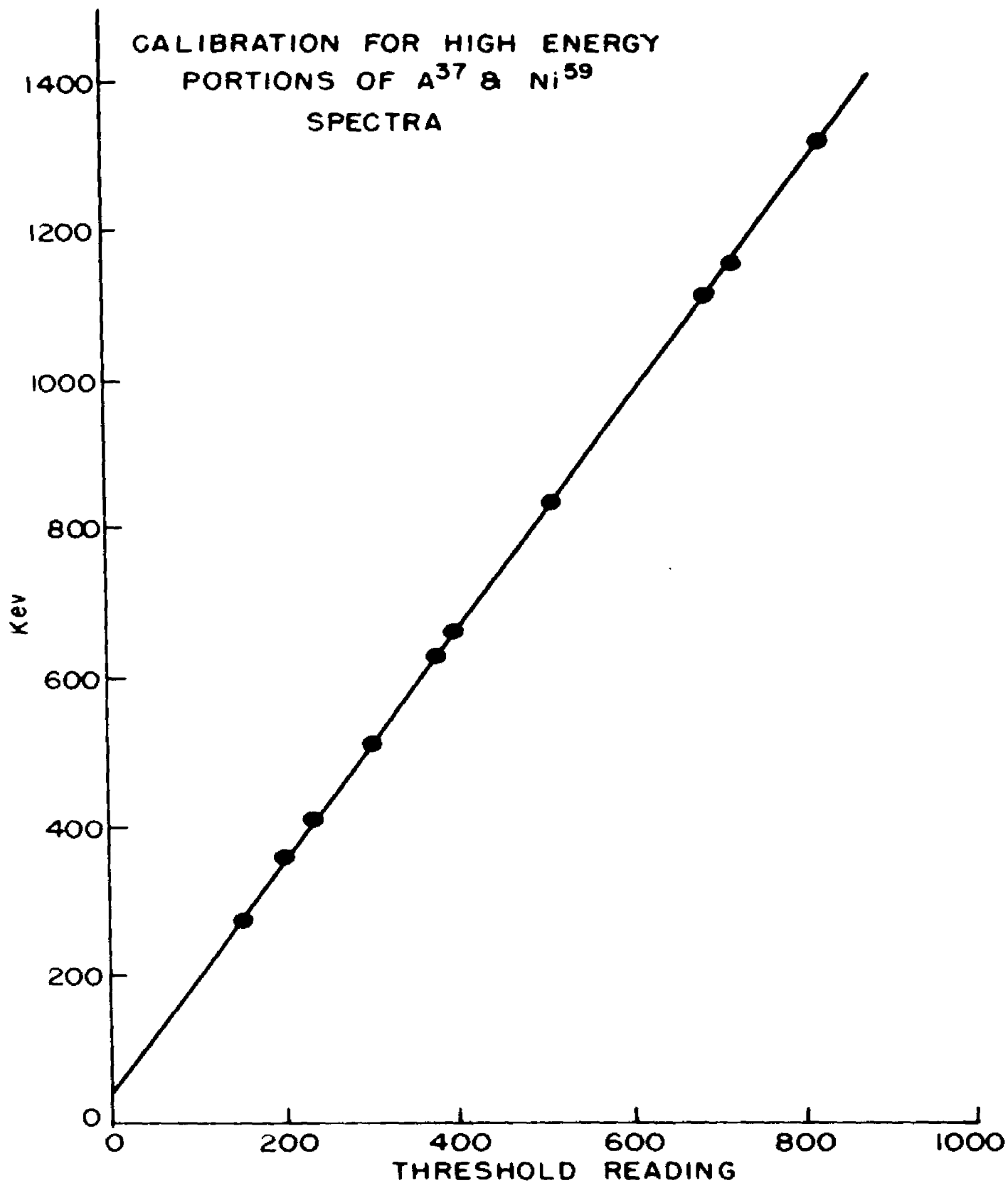


FIGURE 32

TABLE III

Beta Ray Emitters Used for the Determination of the Detection Efficiency of the Crystal

<u>Isotope</u>	<u>Half-life</u>	<u>Beta ray Energy</u>	<u>Remarks</u>
Co-60	5 years	0.31 Mev	100 per cent of gammas
Lu-65	250 days	0.32 Mev	4 per cent of gammas
Cs-137	37 years	mostly 0.55 Mev	131 per cent of gammas
I-131	8 days	mostly 0.6 Mev	1000 per cent of 637 kev gamma 125 per cent of 364 kev gamma
Lu-198	2.7 days	0.96 Mev	100 per cent of gammas

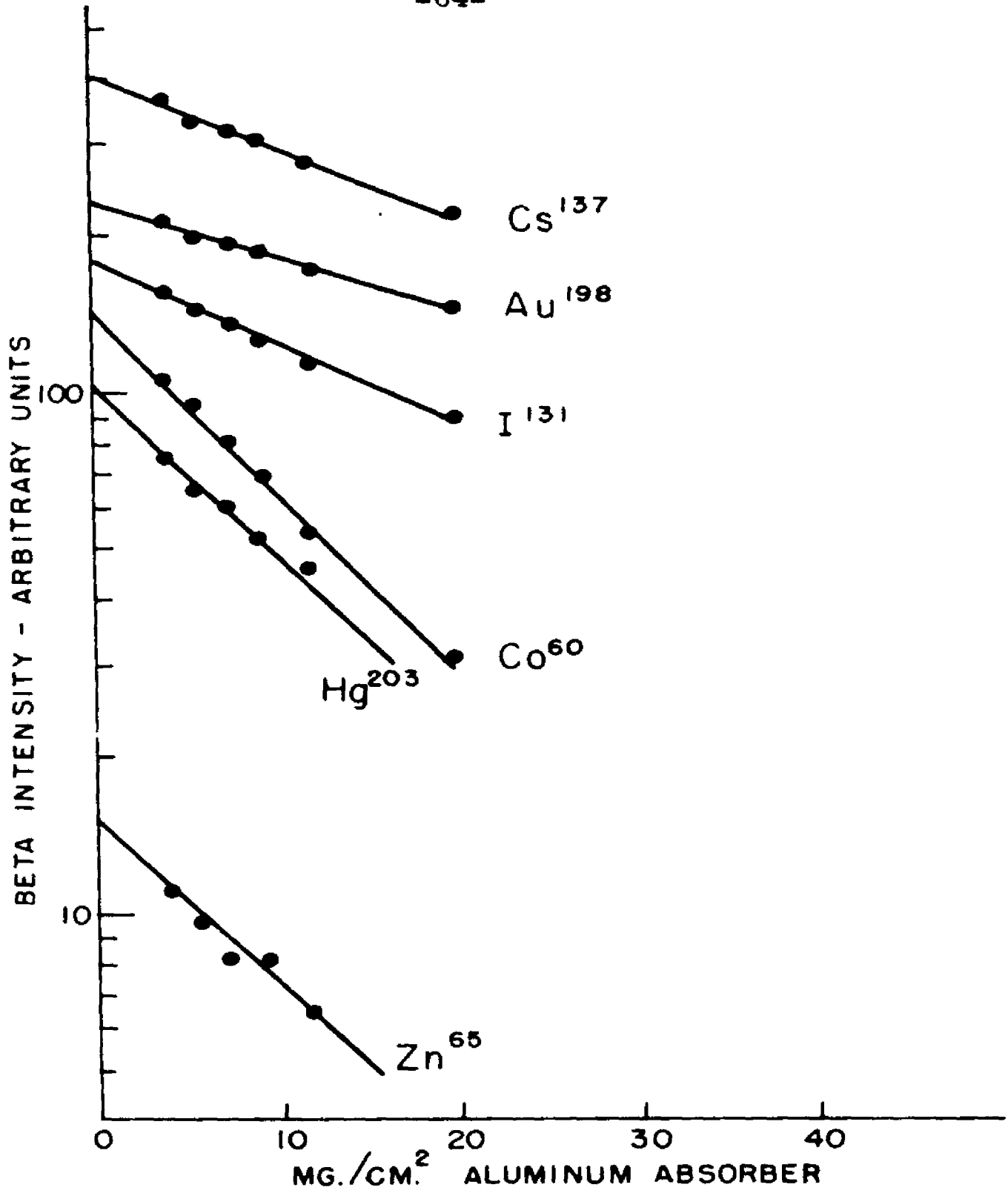


FIGURE 33 BETA RAY ABSORPTION FOR STANDARDIZATION OF GAMMA RAYS.

thickness, the gamma ray activity of each source is calculated. This is compared to the area under each photopeak corresponding to that particular gamma ray as measured in the scintillation spectrometer. The gamma ray peaks are shown in Figures 34 to 39. The normalized intensities are multiplied by the energies of the gamma rays respectively, and plotted in Figure 40. This then represents the empirical correction curve. It is of interest to note that the measurements of Engelkemeir (14) and the calculations and measurements of Maeder (15) agree with the results obtained here.

The empirical correction curve is almost a constant when multiplied by the energy. This leads to an interesting simplification in the analysis of the linear plot data. Since the theory requires that I , the intensity, be divided by E , the energy, and the efficiency curve requires that I be multiplied by E , the linear plot analysis results simply from taking the square root of I . This is true only in the region for which the efficiency is inversely proportional to the energy. As can be seen from the curve, this occurs between 320 and 1160 keV.

6. The Correction for Compton Scattering

The correction for Compton scattering is based on the empirical Compton scattering for monoenergetic

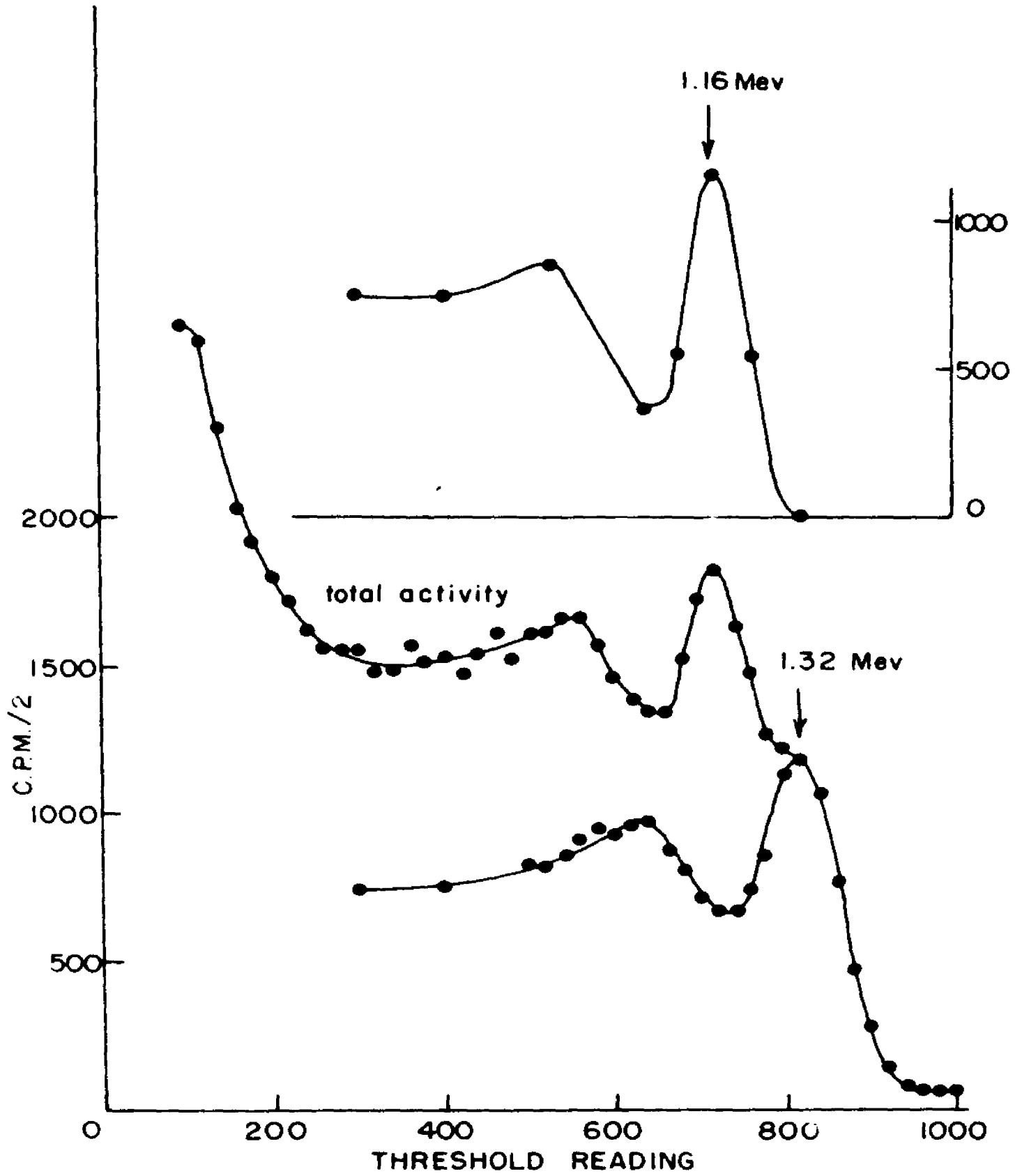


FIGURE 34 Co^{60} GAMMA RAY SPECTRUM.

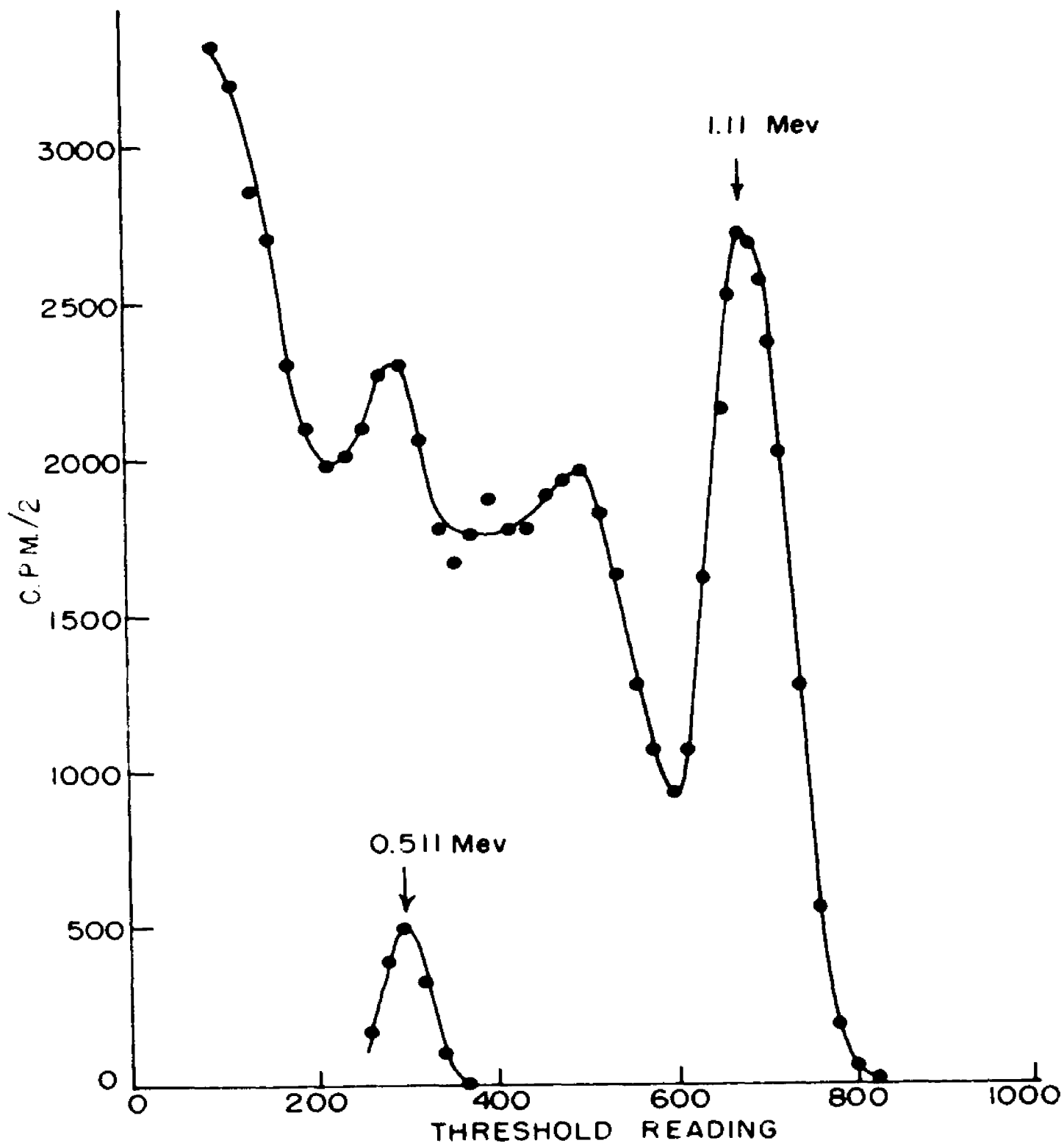


FIGURE 35 Zn^{65} GAMMA RAY SPECTRUM.

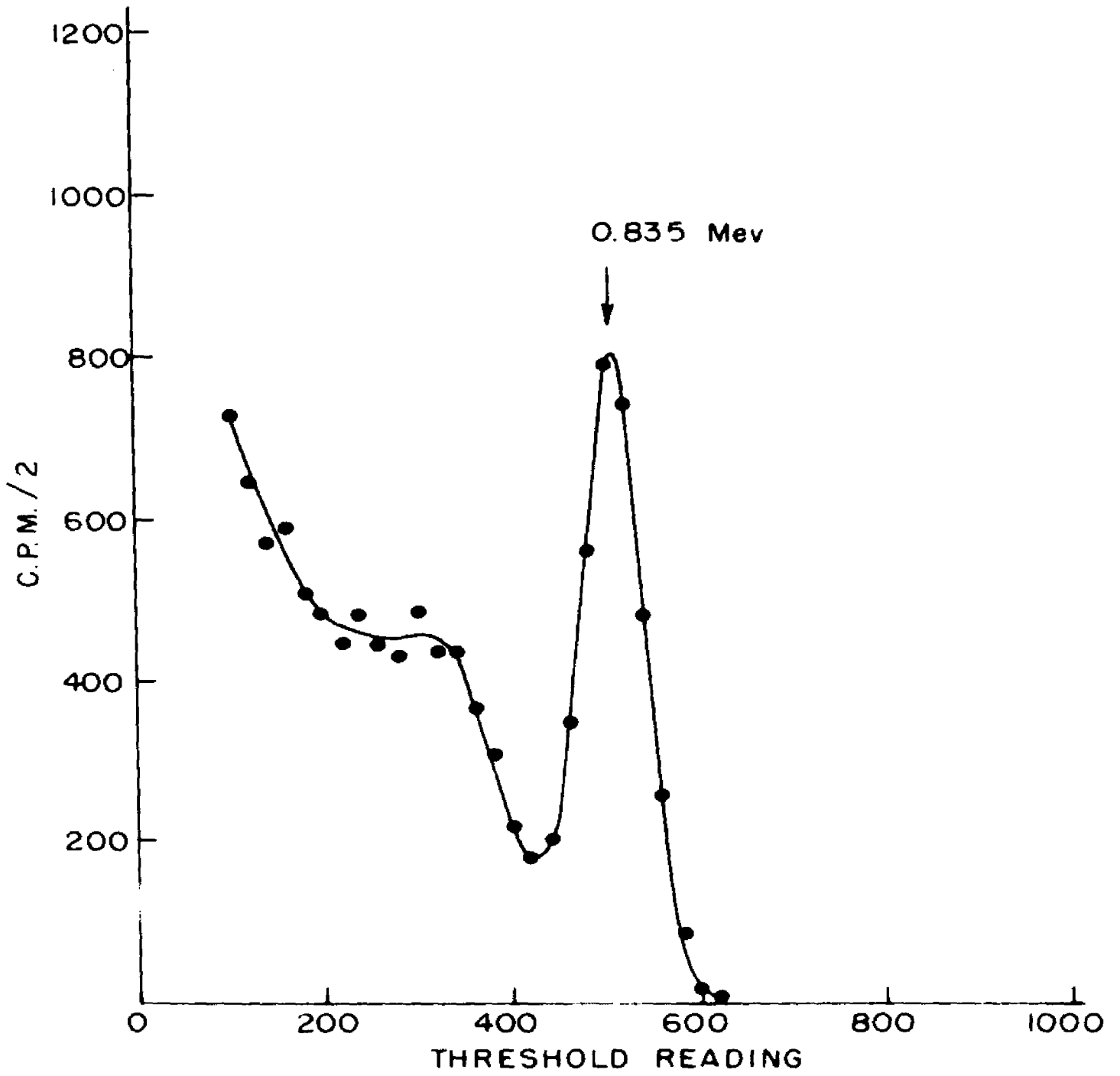


FIGURE 36 Mn^{54} GAMMA RAY SPECTRUM.

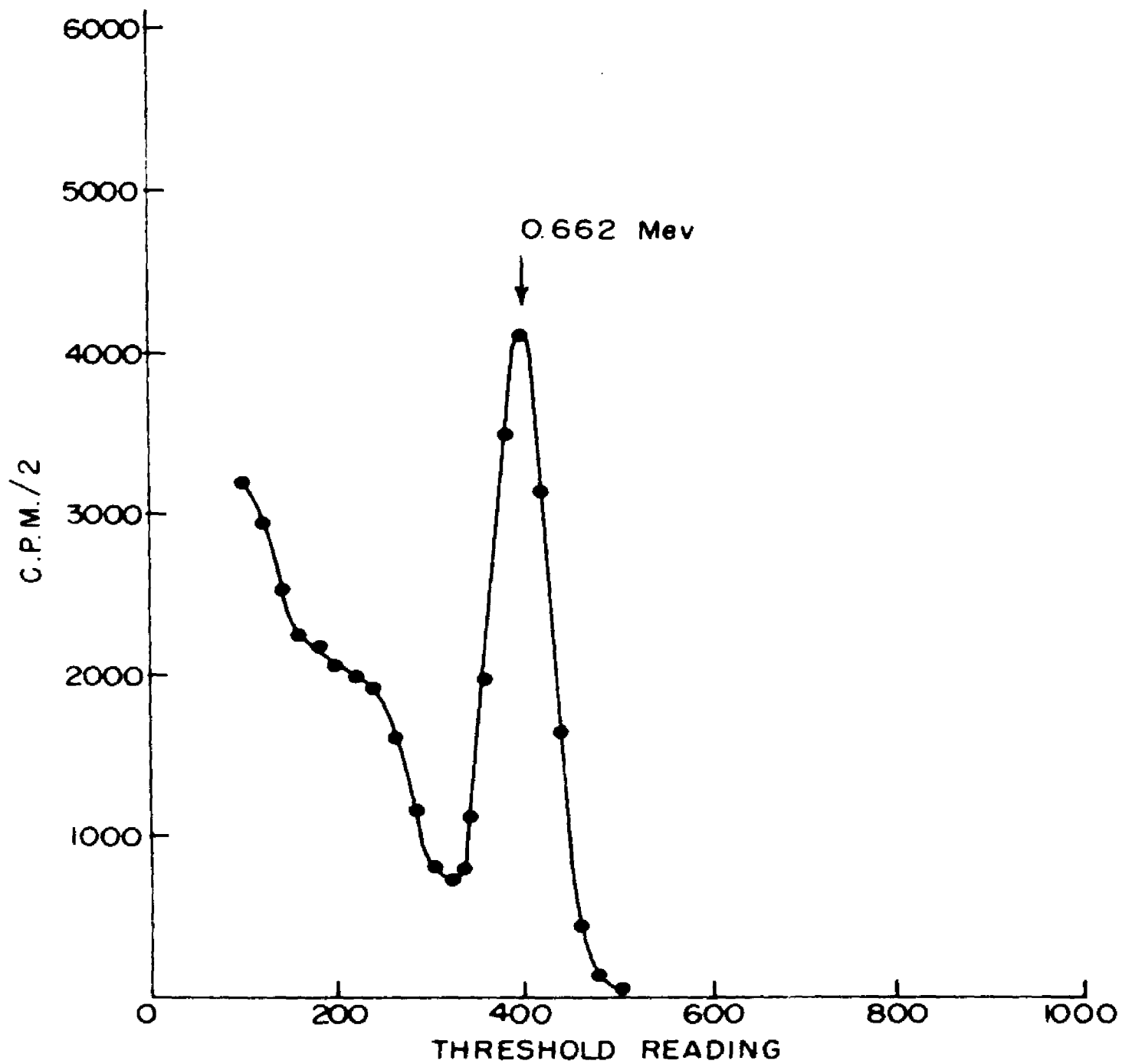


FIGURE 37 Cs^{137} GAMMA RAY SPECTRUM.

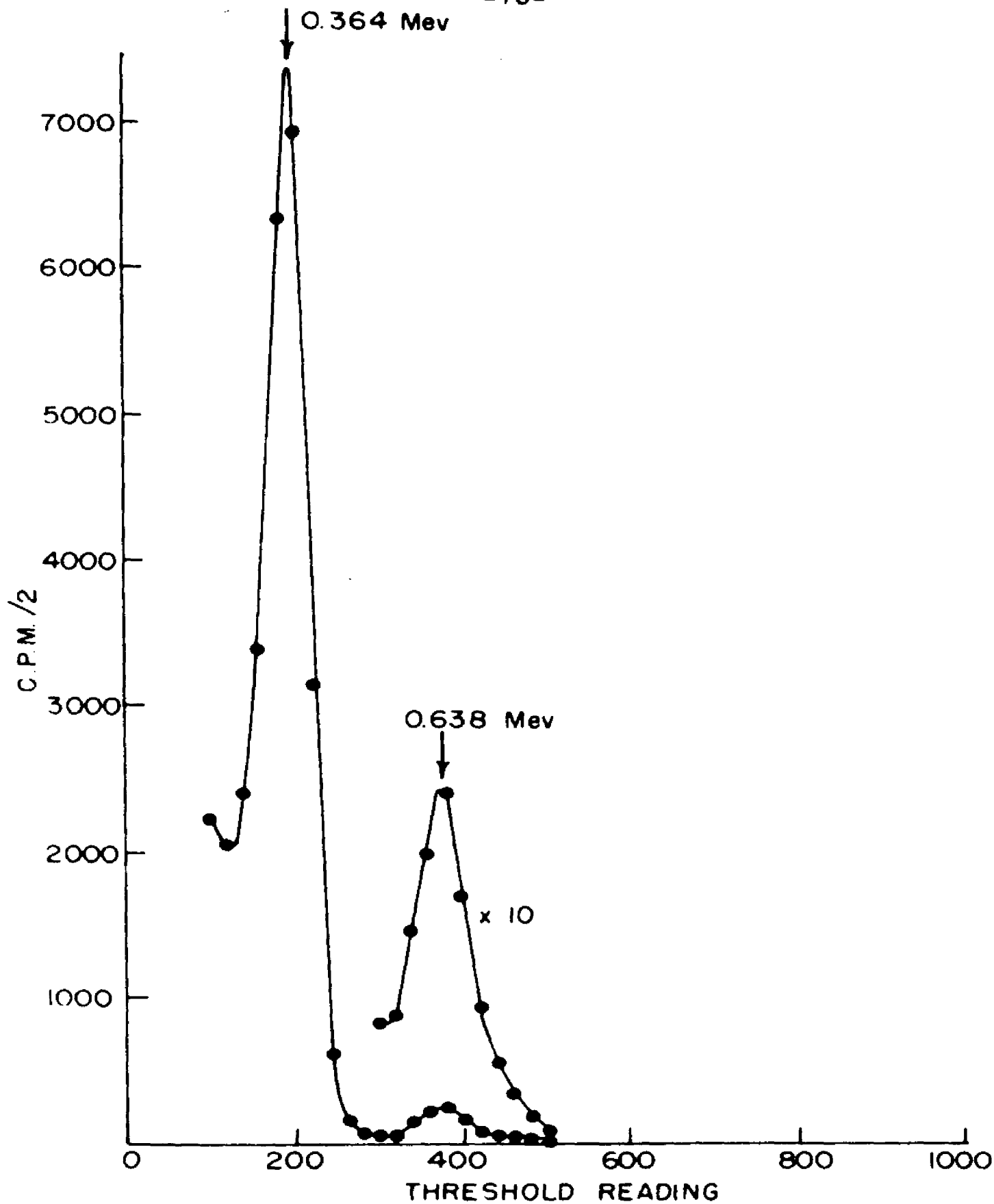


FIGURE 38 I^{131} GAMMA RAY SPECTRUM.

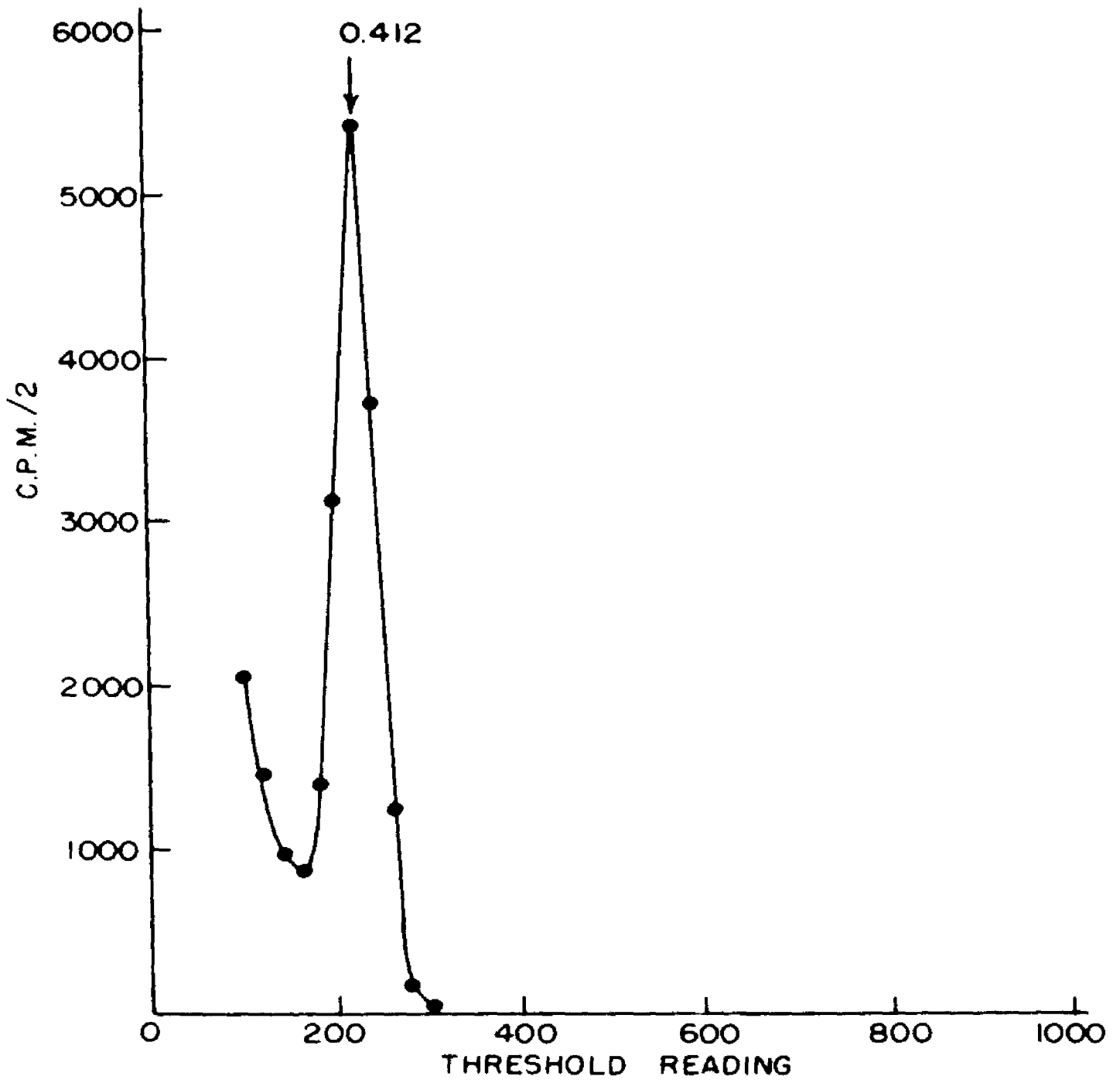


FIGURE 39 Au¹⁹⁸ GAMMA RAY SPECTRUM.

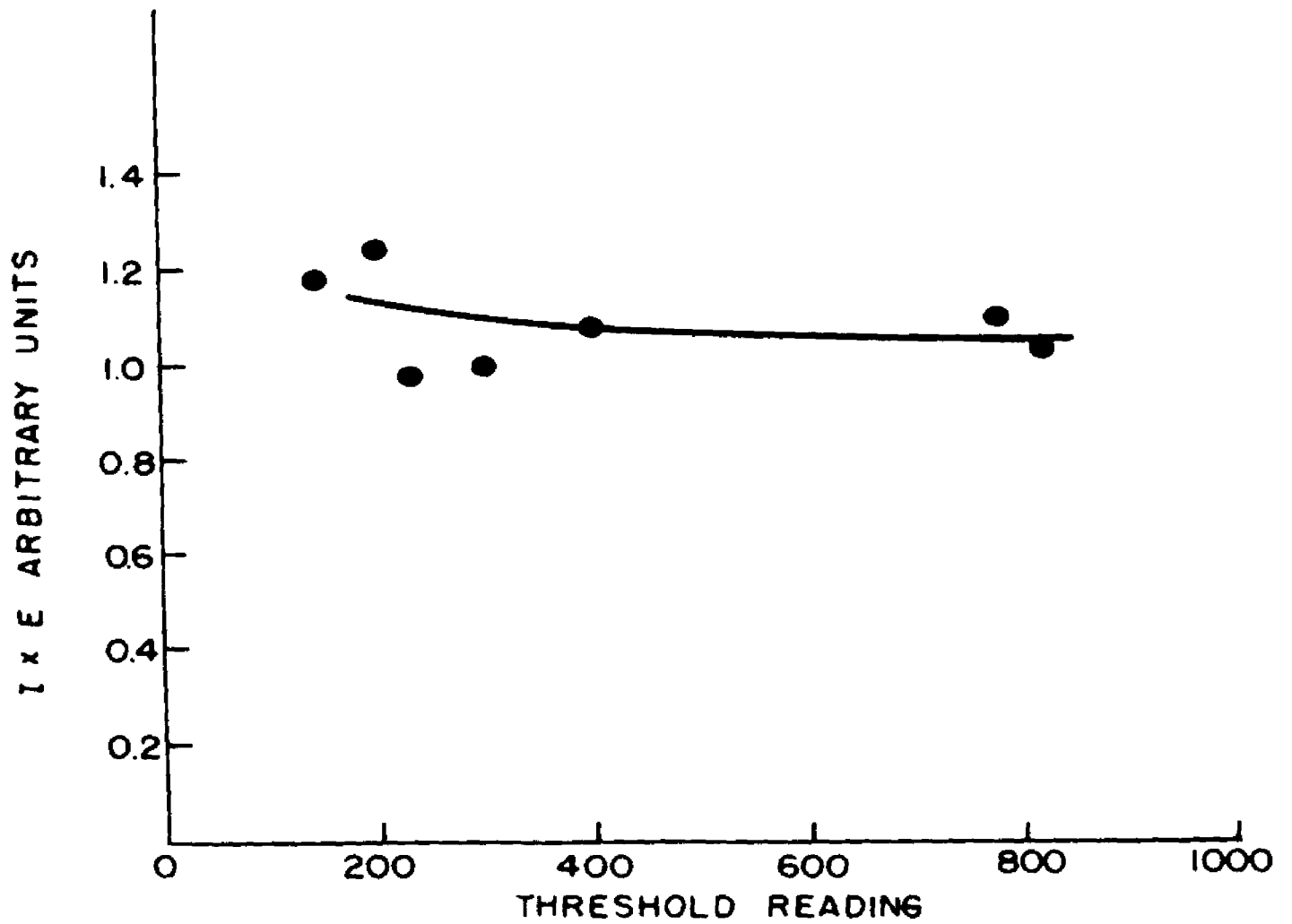


FIGURE 40 NORMALIZED CORRECTION FOR DETECTION EFFICIENCY.

electromagnetic radiation in this particular instrument. The amount of Compton scattering picked up by the crystal is evident from the calibration curves presented in the section on scintillation spectrometer operation. This varies with energy, with geometry, and with crystal dimensions. In order to apply a correction for the scattering to continuous distribution electromagnetic radiation, the experimental curve is divided into sections, each of which represents the equivalent of a monoenergetic radiation curve in its energy range. In other words, the continuous radiation curve is split into sections each of which is the equivalent of the leading edge from a gamma ray distribution.

The analysis is initiated at the high energy end of the continuous energy distribution. The first gamma ray contribution is subtracted from the total curve. The intensity of the gamma ray substituted thus represents the average intensity throughout the region of its application, which is the empirical half-width at that energy. The corrected points do not, therefore, represent any measured or calculated points for that particular energy. They represent the average intensity for the particular energy range for which the gamma ray is applied.

The second highest contribution is then matched to the remainder of the continuous radiation curve.

After its subtraction, the third matching takes place, and so on, until the entire curve is analyzed in this fashion. At each new subtraction, the intensity of the gamma ray required to match the leading edge of the remainder represents the intensity of the continuous radiation in that range. Applications of such an analysis are shown in Figures 44 and Figure 49. The effect of this Compton correction on the intensity distribution is evident from Figures 45 and 46. Figure 45 represents a linear plot for a continuous radiation curve before the Compton correction while Figure 46 shows the same distribution after the correction is applied.

A. EXPERIMENTAL RESULTS ON RADIATIVE CAPTURE

1. INTRODUCTION

The measurement of continuous energy electromagnetic radiation is accomplished in the same manner as the measurement of discrete gamma rays. The instrument operates within a set window or channel, the width of which is adjustable. Superimposed on the resolution value introduced by the window of the pulse analyzer is the inherent statistical distribution in the pulse height introduced by the variation of electron emission from the photocathode and multiplication in the early stages of the photomultiplier.

In the interpretation of the empirical counting rates, the effect of these resolution characteristics must be taken into consideration. In addition to the resolution effects, the escape of degraded radiation from the crystal should be taken into account. This occurs due to the Compton effect and is the origin of the Compton distribution observed for high energy measurements. One reason why the effect is negligible at low energies is that secondary radiation is of such low energy that the chance of secondary and tertiary interaction is high. Thus the entire energy of the gamma is generally dissipated inside the crystal.

2. The Measurement of Iron-55

The experimental intensity distribution of purified Fe-55 is shown in Figure 41. This curve was taken with the first model pulse height analyzer. A repetition of the measurement with the second model analyzer yielded identical results. The curve was analyzed by the method of a linear plot as described in section C. Such a linear plot is shown in Figure 42. The endpoint energy is 217 ± 10 kev. This may be compared to the result of 217 ± 10 kev obtained from the (p,n) threshold energy on manganese. The linear plot is straight within experimental error down to an energy of 80 kev.

3. The Measurement of Argon-37

The experimental intensity distribution of A-37

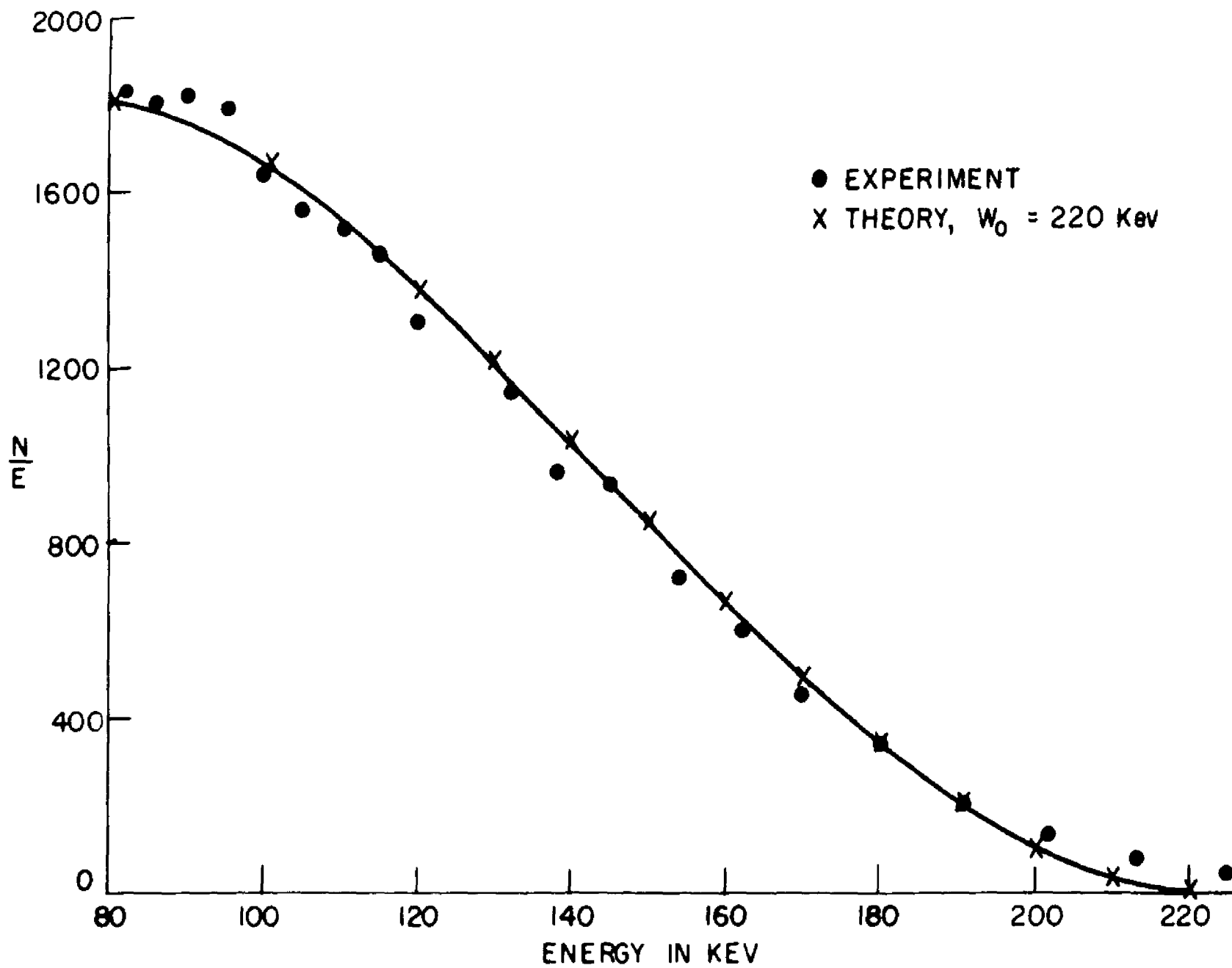


FIGURE 41 EXPERIMENTAL AND CALCULATED SPECTROGRAM OF Fe 55

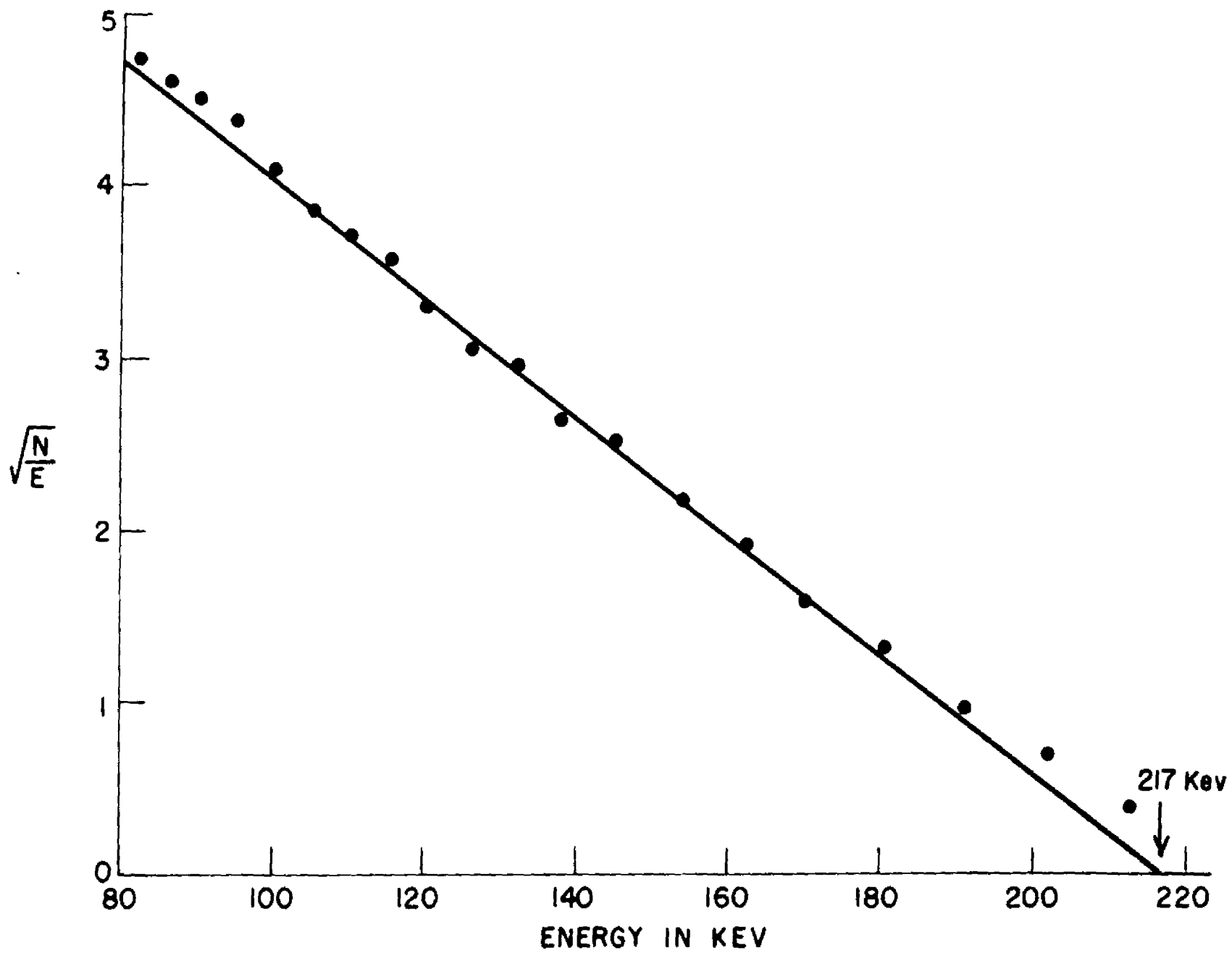


FIGURE 42 LINEAR PLOT FOR Fe 55

extracted from irradiated calcium is shown in Figure 43. This curve was taken with the second model pulse analyzer. Because the energy of the endpoint is well into the range where Compton distribution plays an important role, an analysis was made which corrects for the occurrence of the Compton effect.

The correction graph is shown in Figure 44. The results from this correction are then used to prepare a linear graph shown in Figure 46. As previously pointed out, each point on this graph represents a region of one half-width experimentally observed in that particular energy range. The endpoint of the linear plot is 815 ± 20 kev. This is to be compared with 814 ± 2 kev, obtained from the (p,n) reaction on chlorine-37. The experimental curve is a straight line down to an energy of 320 kev. Below this energy, the correction due to variation in efficiency has not been determined.

4. The Measurement of Nickel-59

The experimental intensity distribution of purified Ni-59 is shown in Figures 47 and 48. Figure 47 was taken with the first model analyzer while Figure 48 was taken with the second model pulse analyzer. In the case of Ni-59 the correction necessary for Compton scattering is somewhat larger than in the case of A-37. The analysis of the experimental curve is shown in Figure 49. A linear plot of the corrected data is

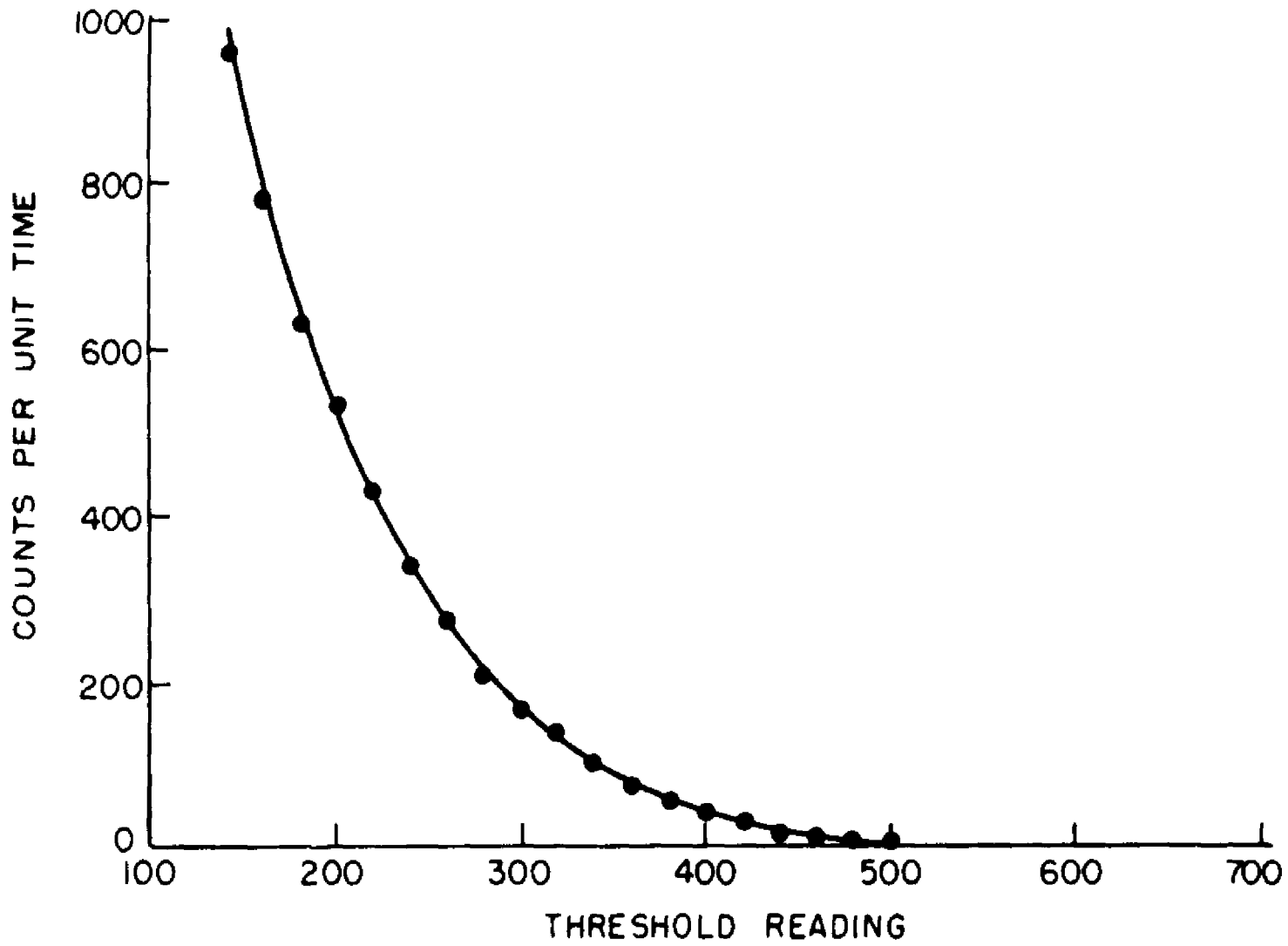


FIGURE 43 HIGH ENERGY PORTION OF ARGON 37 SPECTRUM

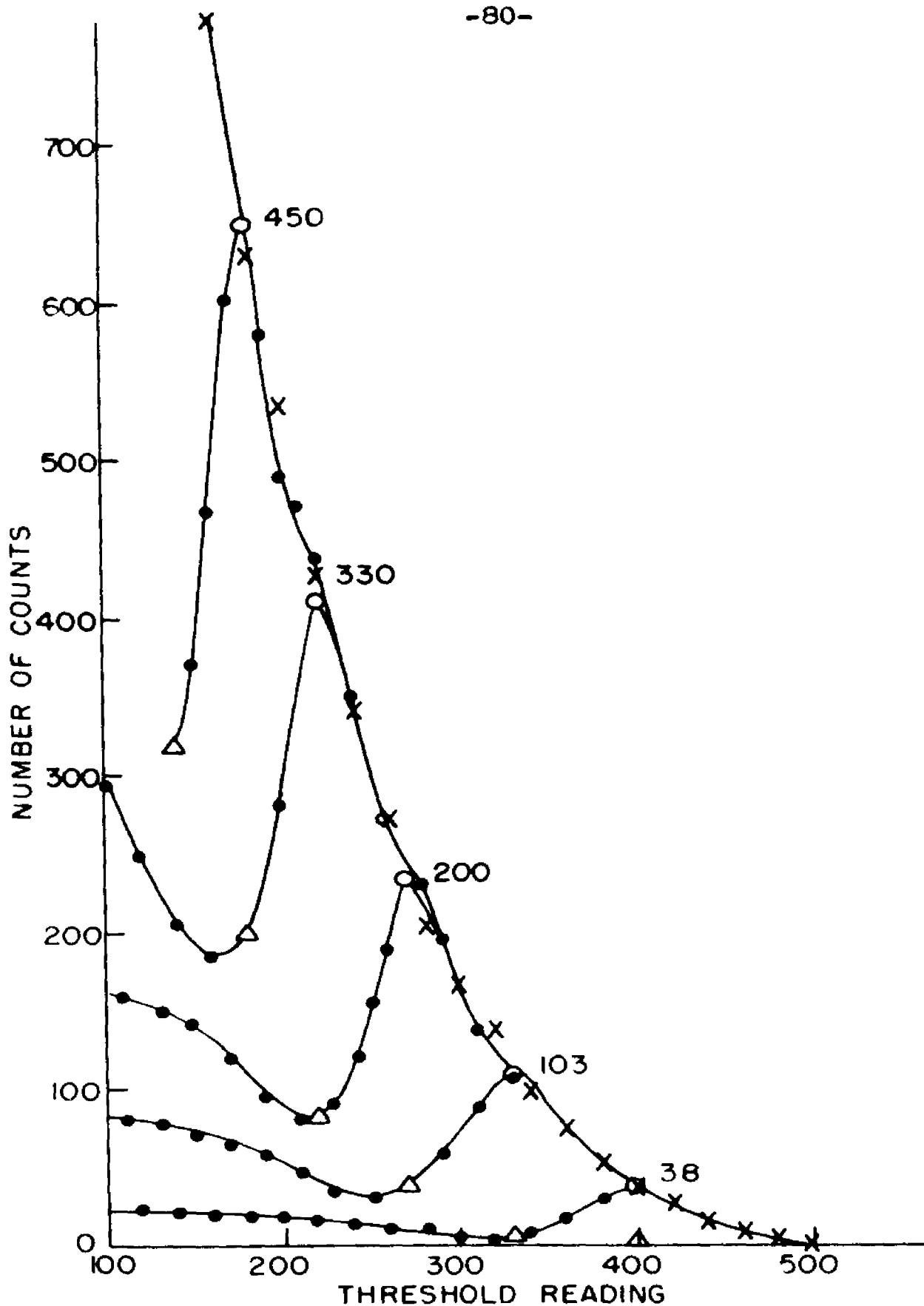


FIGURE 44 COMPTON SCATTERING ANALYSIS FOR ARGON 37 RADIATION.

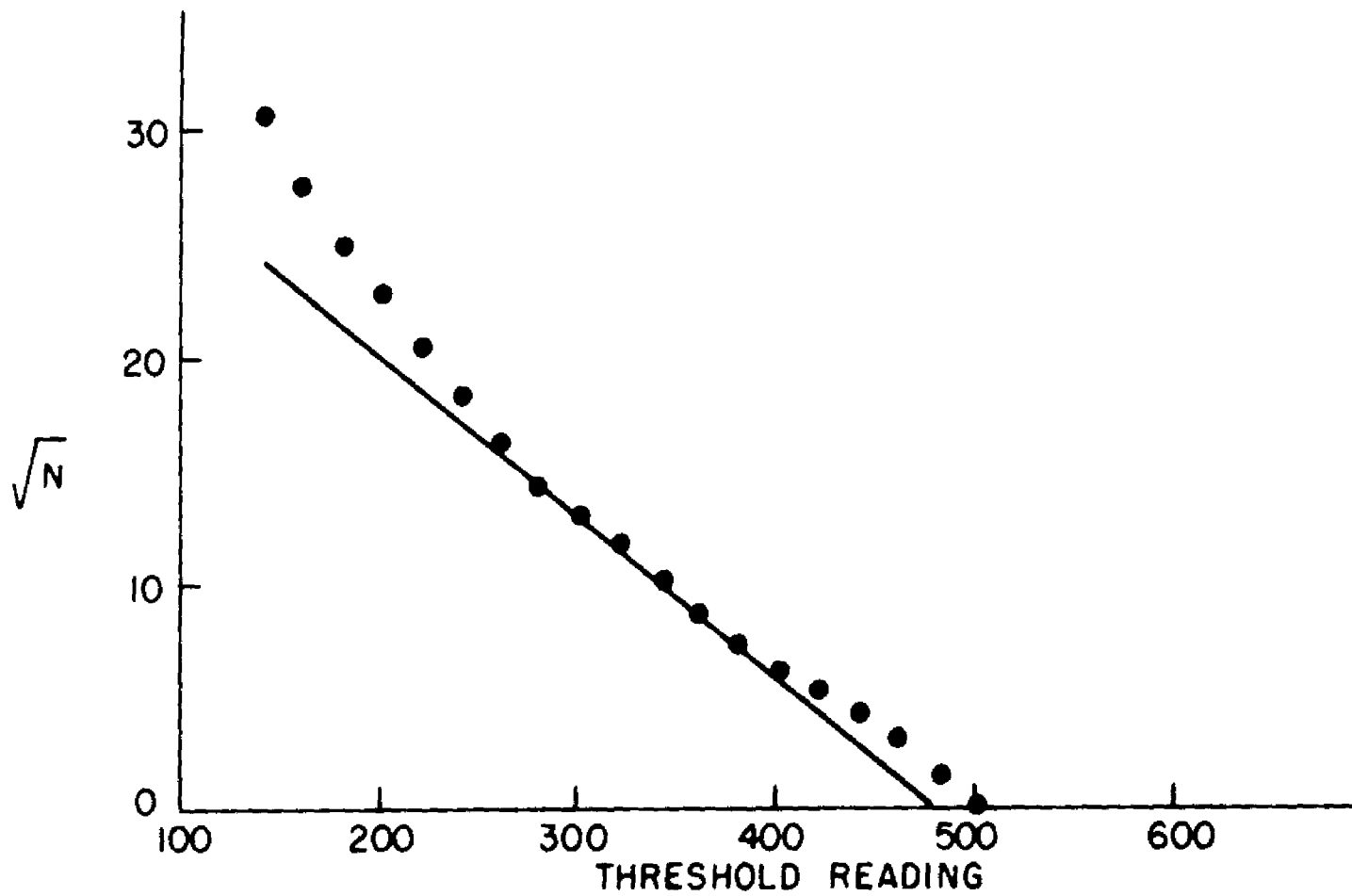


FIGURE 45 LINEAR PLOT OF ARGON 37 NOT CORRECTED FOR COMPTON SCATTERING.

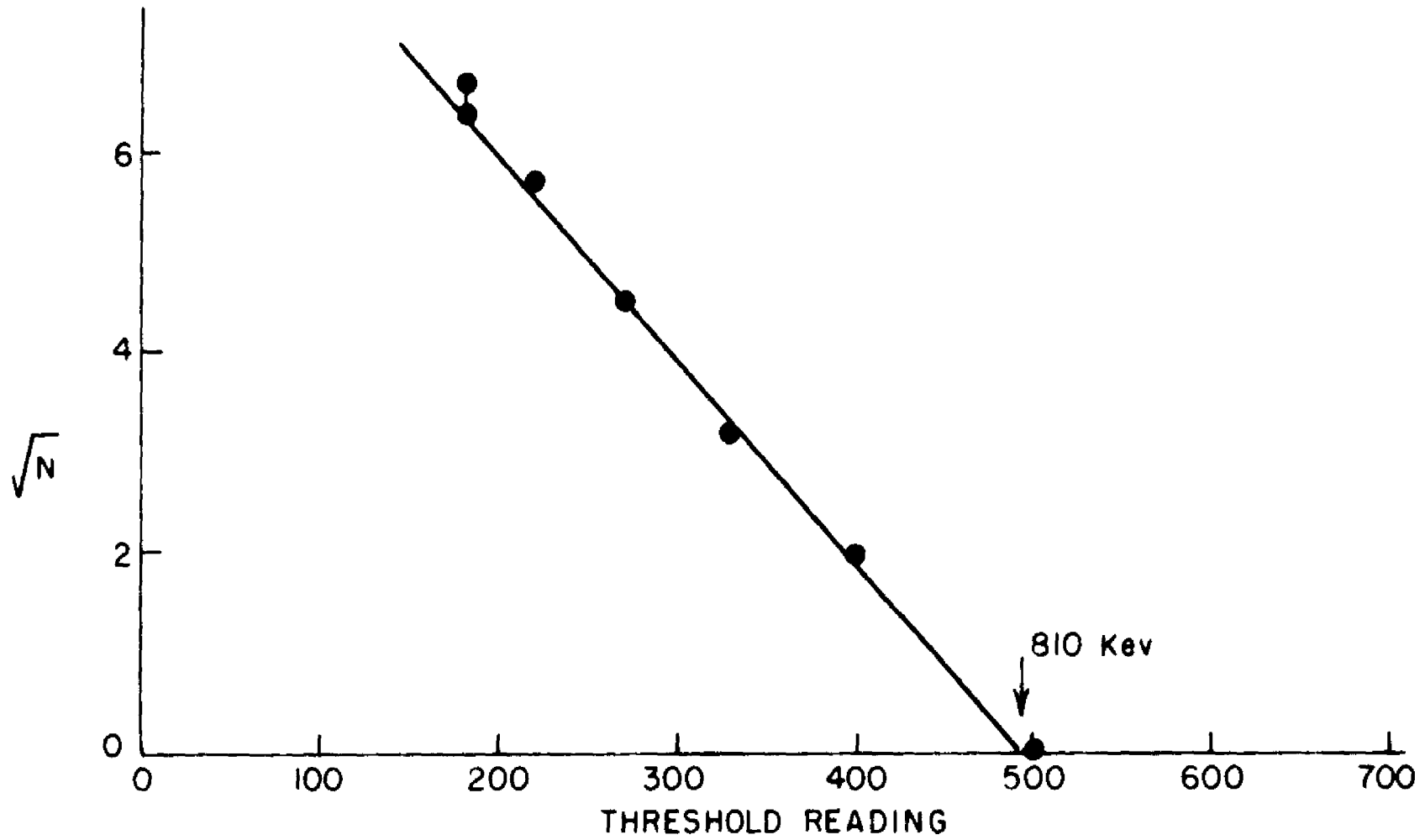


FIGURE 46 LINEAR PLOT OF ARGON 37 AFTER COMPTON CORRECTION.

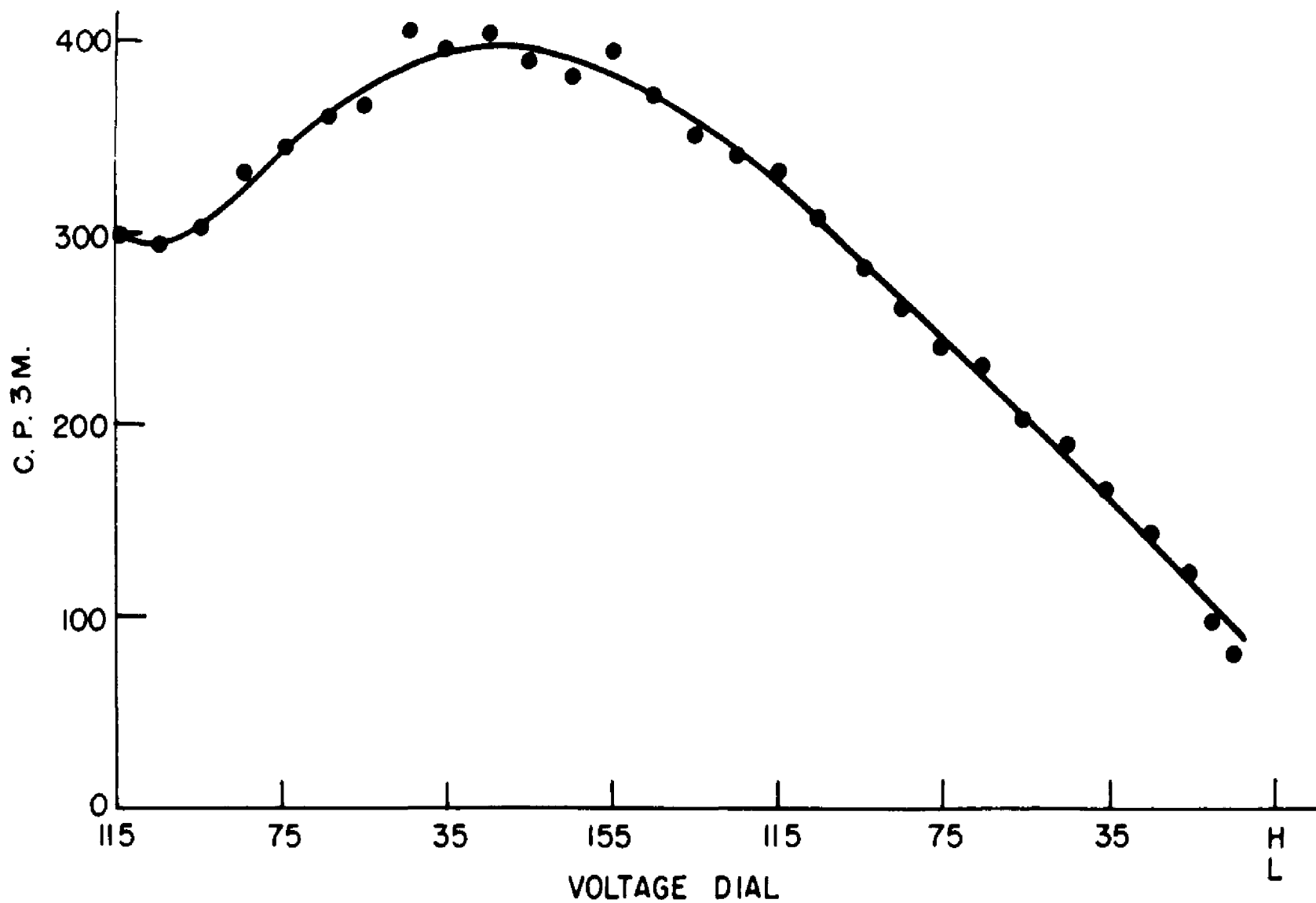


FIGURE 47 MEDIUM ENERGY RANGE OF Ni 59 SPECTRUM

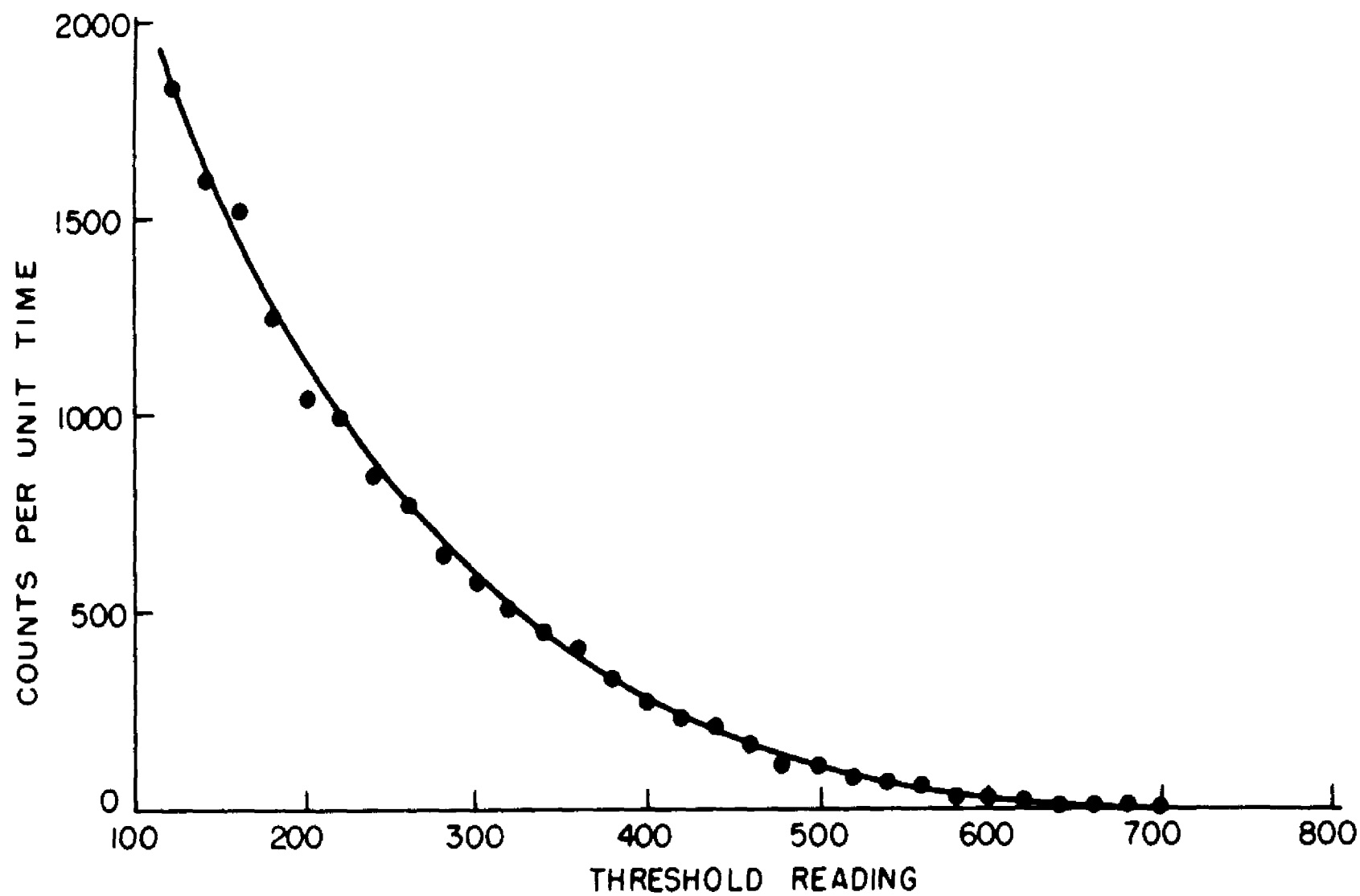


FIGURE 4 B HIGH ENERGY PORTION OF NICKEL 59 SPECTRUM

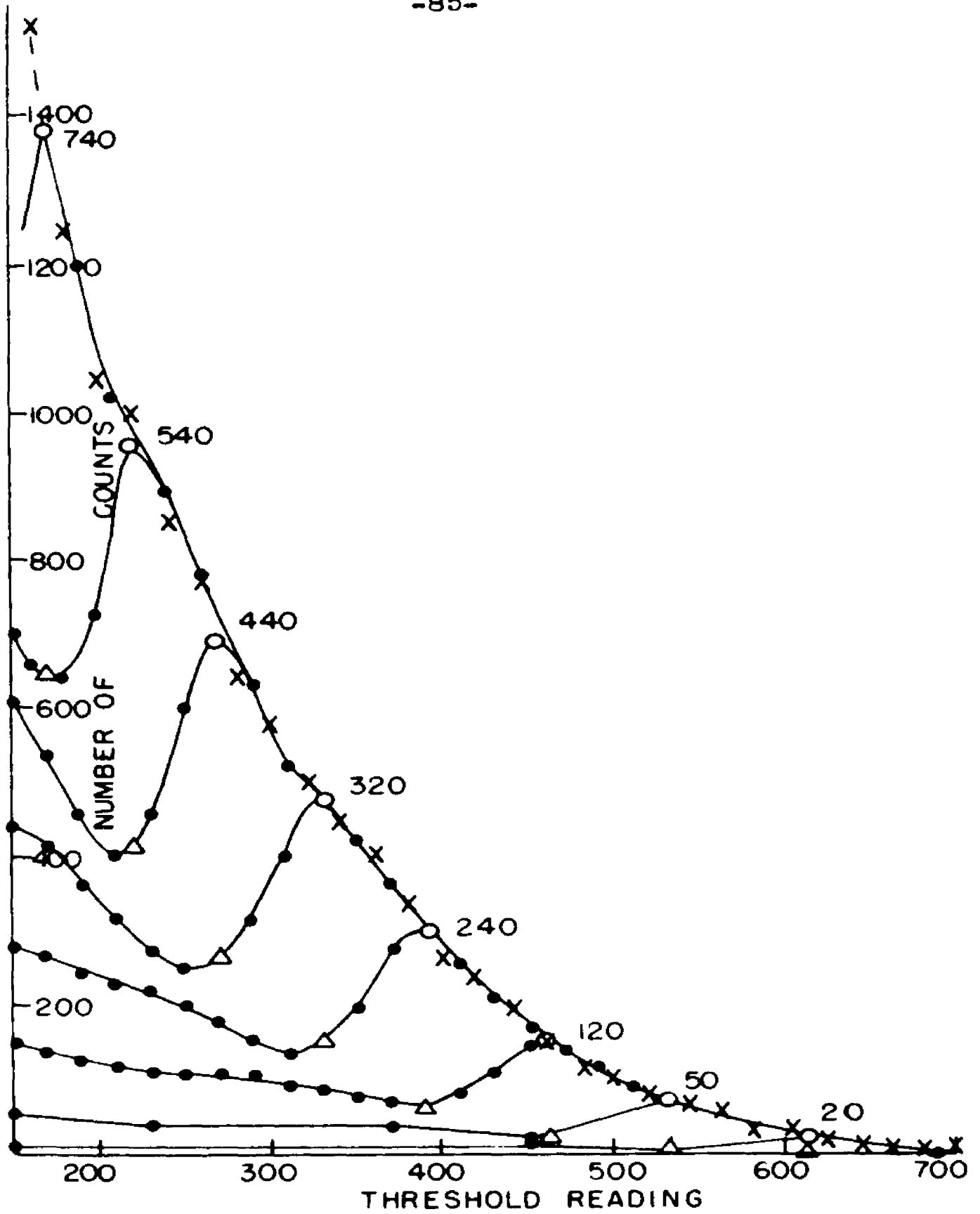


FIGURE 49 COMPTON SCATTERING ANALYSIS FOR NICKEL 59 RADIATION.

shown in Figure 50. An endpoint of 1065 keV \pm 30 keV is obtained. The curve is found to be straight in the linear plot down to the lowest energy for which the efficiency correction is evaluated.

F. DISCUSSION OF RESULTS

The results obtained for the Fe-55, A-37 and Ni-59 endpoint energies are in agreement with the values expected from the (p,n) reaction thresholds. The Mn-55 (p,n) Fe-55 Q value has been reported by Stelson and Preston (16), who obtain a value of -1.006 ± 0.01 MeV for their measurements. This gives 224 keV for the transition energy, and 217 keV \pm 10 keV for the endpoint of the radiative capture spectrum. This is to be compared to the value of 217 ± 10 keV obtained in the present measurements. Other values reported in the literature vary from 200 to 227 keV (9,12). In the section on theory it was pointed out that at energies not exceeding the K shell binding energy by a large amount, the linear plot analysis does not hold. If we assume an arbitrary figure of ten times the binding energy below which the linear plot is not expected to be valid, the experimental data should agree with the linear plot above 70 keV. This is borne out by the results of Fe-55, which show agreement with the linear plot within the experimental errors down to 80 keV.

The Cl-37 (p,n) A-37 threshold has been reported

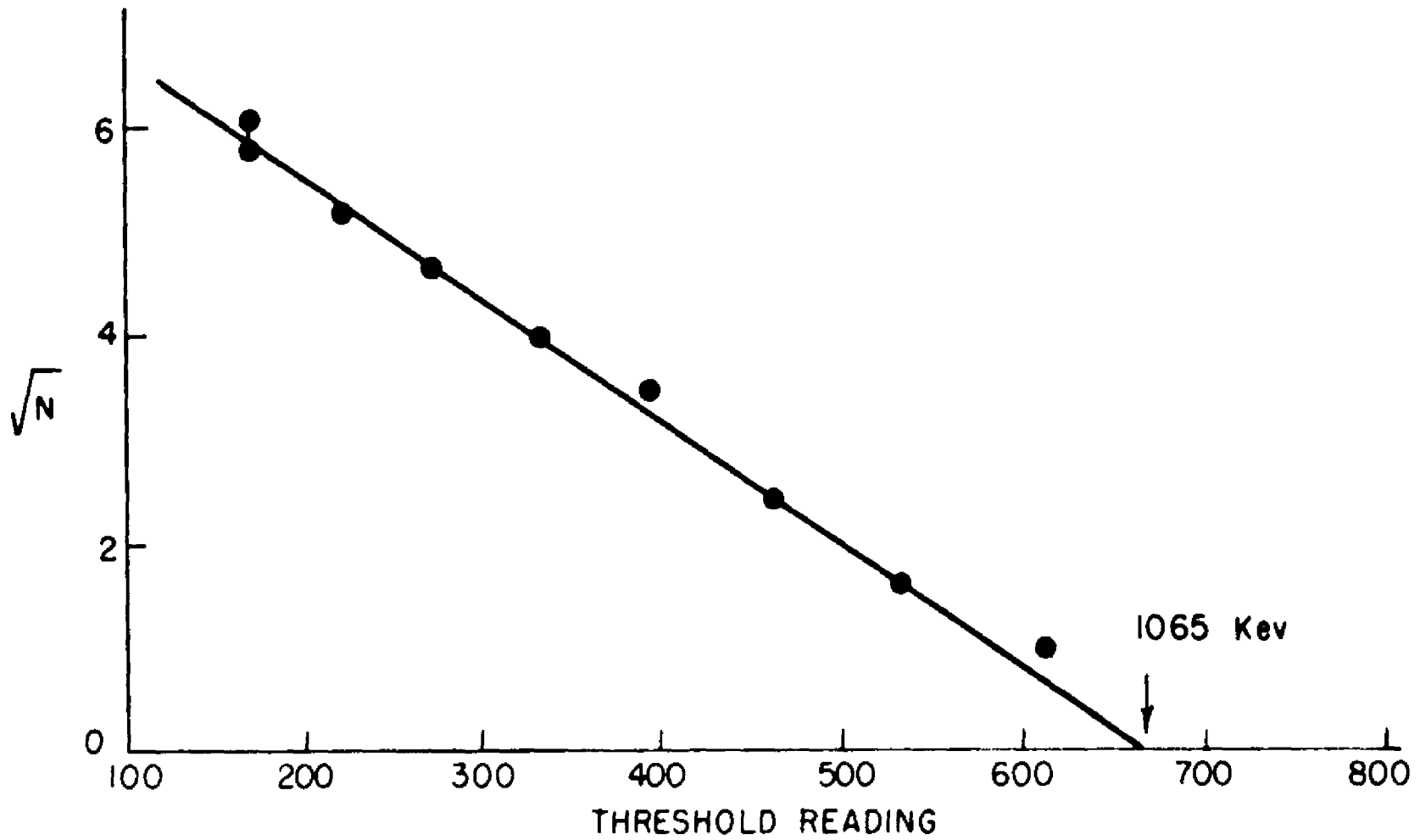


FIGURE 50 LINEAR PLOT OF NICKEL 59 AFTER COMPTON CORRECTION.

by two independent groups (17,18), both of which obtain a value of 814 kev for the expected endpoint of the radiative electron capture spectrum. The error quoted is ± 4 and ± 2 kev. The measurements on the radiative spectrum of A-37 made by Anderson, Wheeler, and Watson (10) show an endpoint of 815 ± 15 kev. These authors show from the ft value of the A-37 disintegration, that the transition is allowed, and consequently, the theory of Morrison and Schiff (3), and of J. M. Jauch (5), is expected to hold. Since they do not apply any correction for Compton scattering to their data, agreement with the linear plot is obtained only down to an energy of 500 kev.

In the present measurements, agreement with the linear plot is obtained down to 460 kev without making any correction due to Compton effect. The difference is believed to be due to the fact that the above mentioned authors use a calculated efficiency curve, whereas in the present work, an empirical efficiency correction was used as obtained from actual measurements of gamma ray response for calibrated samples of radioactivity.

The application of the Compton correction method straightens out the experimental curve down to an energy of 320 kev, which is the lower limit for which the present work was carried out. The endpoint energy

obtained from the final graph is 815 kev in agreement with the threshold data as well as the previous measurements on the radiative spectrum.

The success obtained with the measurements on A-37 gives strong support to the validity of the various correction factors applied to the experimental data in the present measurements. Since the endpoint of A-37 is not far removed from the endpoint energy of Ni-59, it is expected that the application of the same correction technique to the spectrum of Ni-59 represents a valid method of analysis. The comparison with the linear plot will then show whether or not the theory holds in the case of the Ni-59 spectrum which arises in a forbidden rather than an allowed transition.

The Co-59 (p,n) Ni-59 threshold has been measured by McCue and Preston (19) who give a Q value of $-1.857 \text{ Mev} \pm 3 \text{ kev}$. This results in a transition energy of 1073 kev and an endpoint energy of $1066 \pm 3 \text{ kev}$ for the radiative capture spectrum. The direct measurement of this value in the present investigation gives a value of $1065 \pm 30 \text{ kev}$ for the endpoint energy.

The disintegration of Ni-59 to the ground state of Co-59 is believed to involve a change in spin of two units. The nuclear spin of Co-59 has been measured experimentally as $7/2$. The nuclear spin of Ni-59 has not been determined experimentally. According to the

single-particle shell model with strong spin-orbit coupling a spin of 3/2 is predicted for the 31st neutron in Ni-59.

The Gamow-Teller selection rules for beta decay allow first-forbidden or second-forbidden transitions for a spin change of two units. In the present case, it is possible to estimate the forbiddenness from the observed half-life and transition energy of the decay. An approximate expression for the f_k^L value has been given by Bethe and Bacher (20). It is:

$$f_k^L = \frac{2\pi}{9} (Z/137)^5 \frac{W^2 (L-1+W)^2}{12.3^2 \dots (2L-1)^2 L}$$

where Z is the atomic number, W the transition energy and L the forbiddenness.

The following results are obtained for f_k^L :

First forbidden: 4.8×10^{-3}

Second forbidden: 5×10^{-6}

Third forbidden: 4.3×10^{-10}

The experimental half-life of the Ni-59 disintegration is given by Brosi, Borkowski, Conn and Gries (21) as 7.5×10^4 years. Friedlander (22) gives an approximate value of 2.3×10^5 years, and H. W. Wilson (23) a revised value of 6.9×10^4 years. All these values have been calculated from cross-section yield measurements.

Combining the experimental half-life value with the calculated f values, gives the following set of ft values:

First forbidden: 1×10^{10}

Second forbidden: 1.1×10^7

Third forbidden: 1×10^3

Ft values for electron capture are found to be about 5×10^6 for first forbidden transitions, 5×10^8 for second forbidden transitions, and higher for third forbidden transitions. It is seen from the above calculation, that the best agreement is obtained for the second forbidden transition.

Since the transition energy in Ni-59 is greater than $2mc^2$, it is expected that positron disintegration occurs. Knowing that the disintegration is second-forbidden, it is possible to calculate approximately what the branching ratio of positrons to orbital electron capture should be:

The ratio of beta emission to electron capture (K+L) is given by:

$$\frac{\text{Beta}}{K+L} = \frac{B_2}{B_c(2)}$$

$$\text{where } B_2 = \frac{1+s}{2} \frac{f_2}{f_0} f_0 \quad s = \left(1 - \frac{Z^2}{137^2}\right)^{1/2}$$

$$\text{and } B_c(2) = \frac{\pi}{2} (2W^6 g_k^2 + W^6(2g_l^2 + 2f^2) + 30W^4 4g_r^2)$$

$$\text{where } g_k^2 = 5 \times 10^{-2}$$

$$g_1^2 = 4 \times 10^{-3}$$

$$f^2 = 5 \times 10^{-6}$$

$$g_r^2 = 3 \times 10^{-4}$$

These formulas and values are those given by Marshak (24). The evaluation of the ratio f_2/f_0 is accomplished by means of the calculated values of f_1/f_0 published by Davidson (26), and the ratio f_1/f_2 is calculated by evaluating his \bar{C}_1 and \bar{C}_2 .

The energy available for the positron decay is 55 kev. From Davidson's formulas, the ratio f_2/f_0 is 1.65×10^{-5} . The value of f_0 is 2.5×10^{-6} as taken from the tables of Feenberg and Trigg. This yields a value of 2×10^{-11} for B_2 .

$B_c^{(2)}$ can be found from straight substitution in the above formula, and the result is 8.1.

The ratio of positrons to electron capture is:

$$\frac{\text{Beta}}{K+L} = \frac{20 \times 10^{-12}}{8.1} = 2.5 \times 10^{-12}$$

The experimental search for positrons is shown in Figure 51. The upper limit of positron occurrence in this attempt is 4.3×10^{-5} . A separate attempt has been made by S. E. Singer (12), who obtains an upper limit of 2×10^{-5} . The best previous attempt is reported by H. W. Wilson (23), who attains an upper limit of 1×10^{-4} .

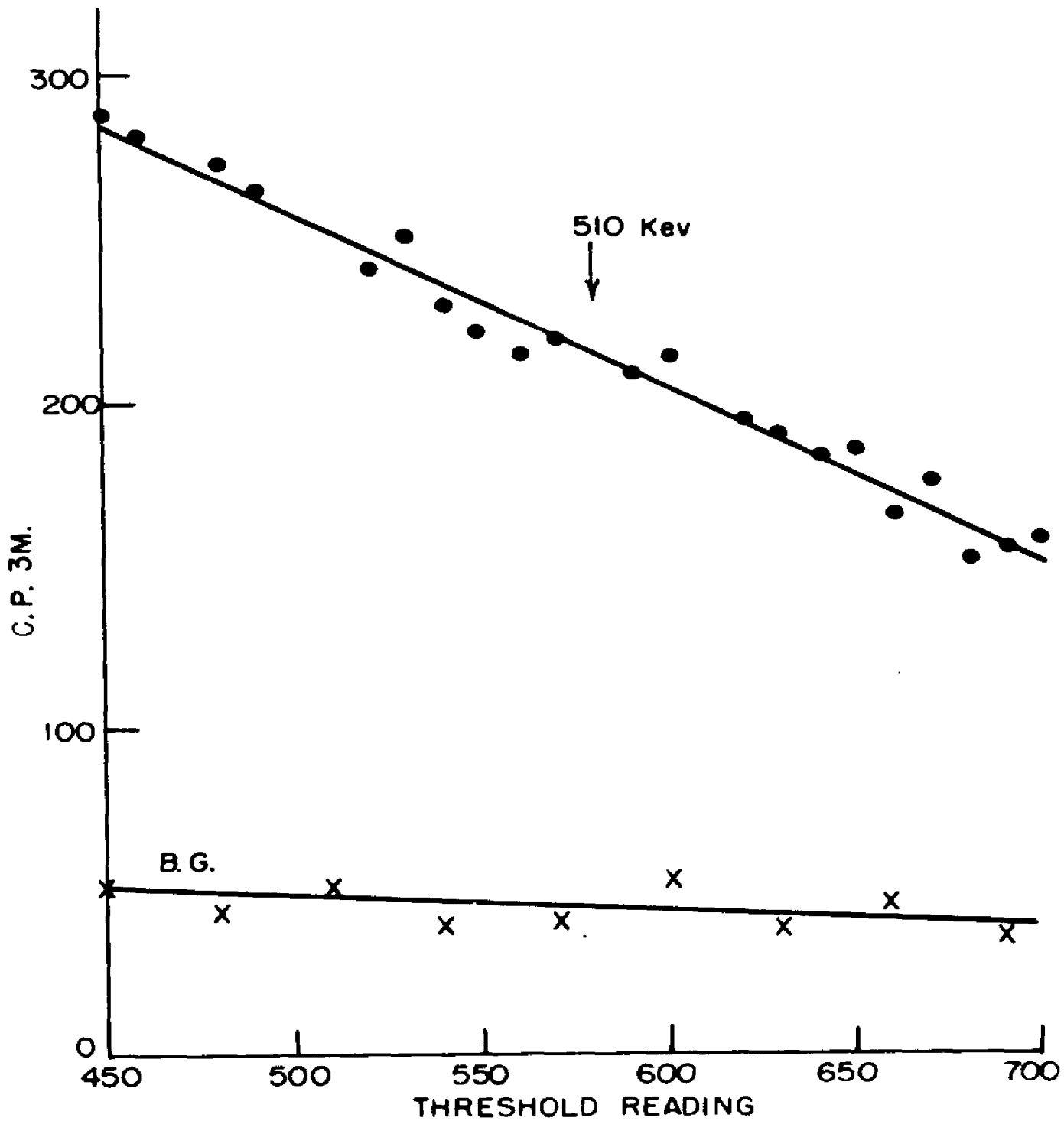


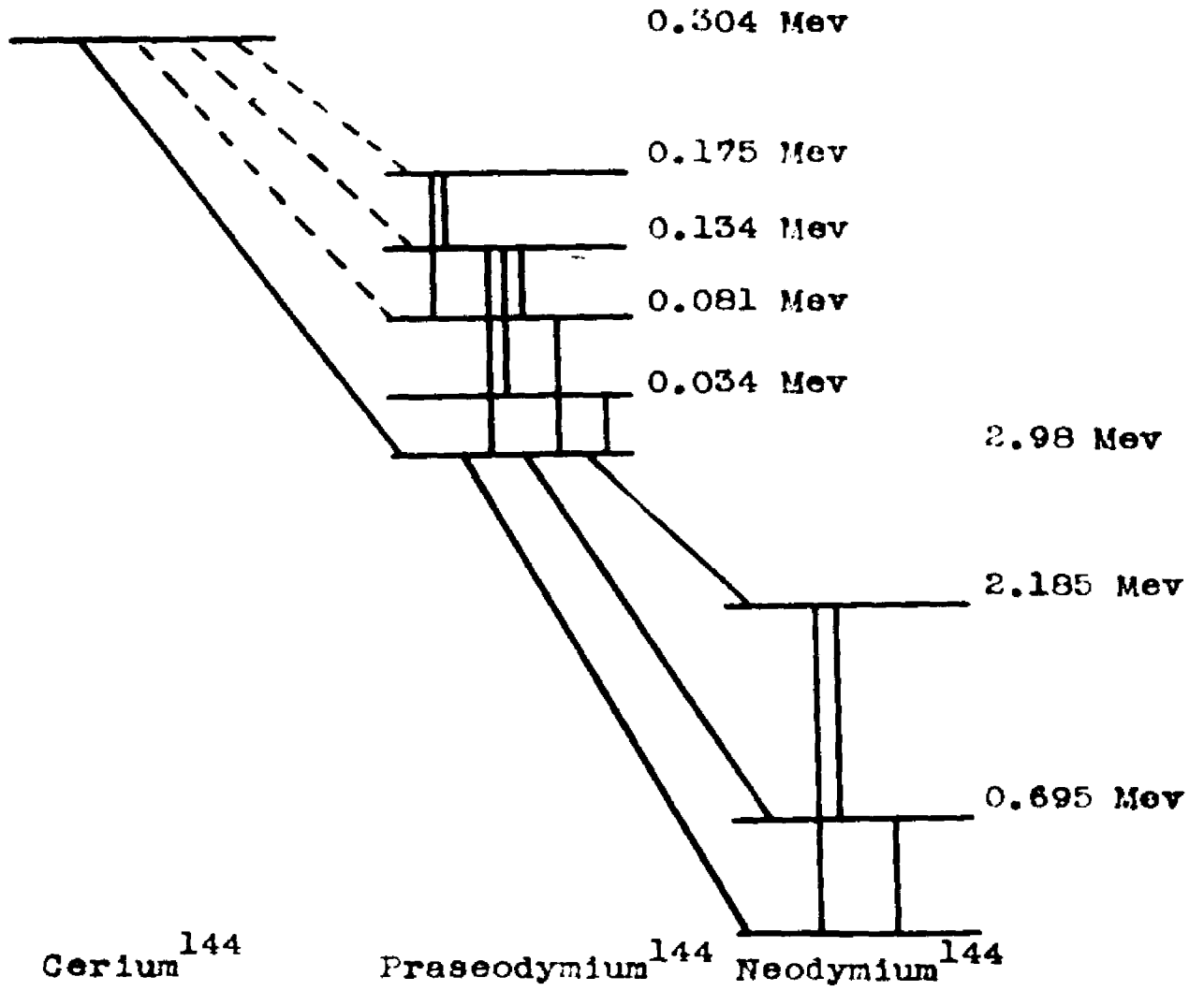
FIGURE 51 POSITRON SEARCH IN Ni 59

II. THE NUCLEAR SPECTRA OF Ce-144 AND ITS DECAY PRODUCTS

A. INTRODUCTION

The nuclear radiations of the Ce-144 and Pr-144 beta disintegration have been of extensive interest in the field of nuclear spectroscopy. This interest is in part due to the large fission yield and long half-life of Ce-144, which make this isotope particularly easy to obtain, and easy to work with. The most recent information regarding the nuclear radiations is collected in the isotopic table of Hollander, Perlman, and Seaborg (27), whose decay schemes for Ce-144 and Pr-144 are largely an extension of the combined energy level decay scheme proposed by Porter and Cook (28). The comparatively complex structure of low energy levels existing in Pr-144 was first shown from internal conversion lines observed in a photographic spectrograph by Emmerich, John, and Kurbatov (29).

Alburger and Kraushaar (30) were able to show from angular correlation measurements carried out between the 695 kev and the 1480 kev gamma rays, that the energy levels of 2185 kev and 695 kev in Nd-144 are related to the (0+) ground state by the spin relation 1-2-0. An energy level diagram showing all levels reported by the preceding authors is reproduced in Figure 52.



Cerium¹⁴⁴

Praseodymium¹⁴⁴

Neodymium¹⁴⁴

Figure 52

. The Beta and Gamma Transitions in the Disintegration of Ce-144 and Pr-144.

Since the beta decay chain occurs between two even-even nuclei whose spins and parities are presumed to be zero and even, respectively, a certain amount of symmetry is expected to exist in the beta ray structure of these species. That this is not entirely supported by the experimental evidence, has already been pointed out in the literature (28). A clarification of the branching ratios and relative intensities of the various internal conversion lines may shed possibly further light on the theoretical discrepancy which is observed in the ft values of the ground to ground transitions of these decays.

B. MODE OF DECAY

Cerium-144, generally obtained as fission product, disintegrates by beta emission to Pr-144 with a half-life of approximately 290 days. About seventy per cent of the decay has been found to lead directly to the ground state of Pr-144 with an endpoint energy of 304 kev, while the remainder excites several levels, the most intense of which is 134 kev above the ground state. Others have been reported at 175, 81, and 34 kev. No direct measurements have been made on the inner beta spectra which should occur to feed these levels.

The disintegration of Pr-144 occurs with a half-life of 17.5 min., principally to the ground state of Nd-144 by the emission of a 3 Mev beta ray. A small

fraction of the decay leads to excited states of 2185 kev and 695 kev in Nd-144, but the branching ratio of the associated beta rays is not well known. The relative intensity of the gamma rays has been measured by Alburger and Kraushaar (30).

C. EXPERIMENTAL RESULTS

1. Internal Conversion Lines

The internal conversion electrons in Pr-144 and Nd-144 were measured in a photographic permanent magnet spectrograph of the type described by Emmerich (31). In order to improve the momentum resolution over previous measurements, the defining slit width was reduced from six to three millimeters. This decreased the luminosity of the instrument, so that stronger sources and longer exposures were needed than for the work previously described (29). Special care was taken to prepare a line source as narrow as possible. The final width of the source was 0.25 millimeters. The measurements were taken with various magnetic field strengths, but the best results were obtained with a field of 114 gauss which covered an energy range of 15 to 150 kev.

The internal conversion line intensities were determined with a recording type photodensitometer and analyzed according to the method of Rutledge, Cork, and Burson (32). A typical densitometer graph is shown in Figure 53. The energies and the relative

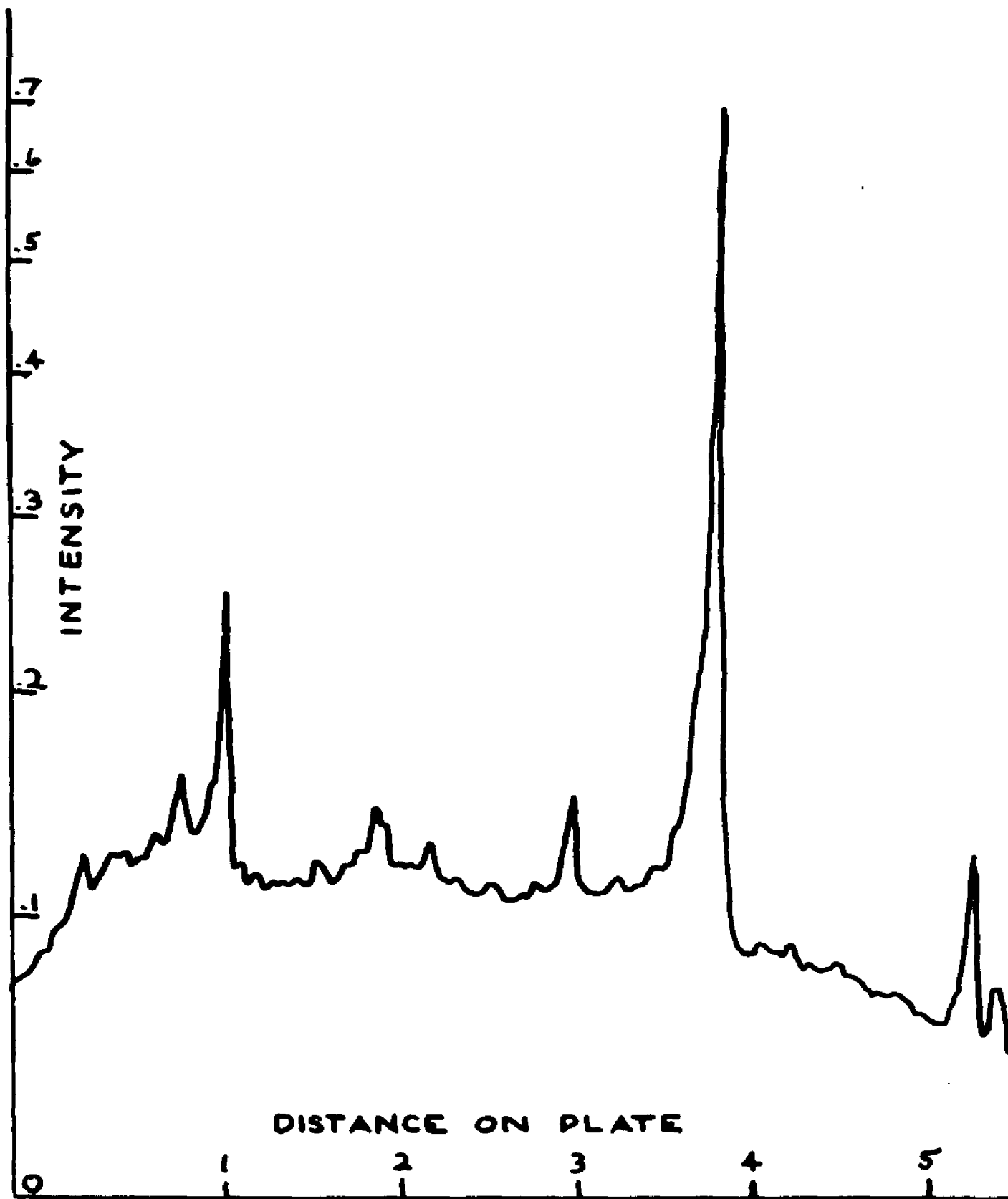


Figure 53 . Photodensitometer Reading of the Internal Conversion Lines Recorded on a Photographic Plate in the Permanent Magnet Spectrograph.

intensities of the lines are found in Table IV, where the intensity of the 92 kev K line of the 134 kev transition is taken to be 100. The lines are organized according to the associated gamma rays, the energies of which are indicated to the nearest kev. These energies are in agreement with those of the previous determinations made. Also shown are the K/L and L/M shell ratios, where these can be determined, as well as the lowest allowed multipoles determined from the shell ratios.

The 134 kev and 81 kev transitions were first identified as occurring in the disintegration of Ce-144 by Emmerich, John, and Kurbatov (29). Since then, they have been investigated extensively and little doubt remains at this time regarding their energy and their K/L shell ratios. The 100 kev and 34 kev transitions are believed to be in cascade across the 134 kev energy gap. These transitions are of much lower intensity than the former two, and information leading to their multipole assignment is not so easily available. The L conversion line of the 100 kev transition is covered up by the much more intense K line of the 134 kev transition, and the K/M ratio is the only ratio available at this time. For the 34 kev transition, only the L/M ratio is formed, since the transition energy is less than the K shell binding energy. Neither of these ratios can be utilized for the prediction of the multipole

TABLE IV

Internal Conversion Lines in the
Disintegration of Ce-144 and Pr-144

Line Energy in kev	Relative Intensity	Assignment Element,	Gamma Energy in kev	Shell-Ratio K/L	L/M	Multipole Radiation	
92.2	100*	Pr	K	134	8	4	M1
127.8	12		L				
133.1	3		M				
33.5	49	Pr	K	81	5	9	M2
74.0	9		L				
79.2	1		M				
27.0	11	Pr	L	34		3	
32.5	4		M				
58.7	4	Pr	K	100			
99.0	1		M				
46.6	3	Pr	L	53			
34.2	11	Pr	L	41		11	
39.6	1		M				
52.7	7	Pr	K	94			
88.0	trace		L				
16.8	4	Nd	K	60	1		
53.3	4		L				
29.2	12	Pr	L	Auger		2	
34.2	6		M				

*The intensities of the internal conversion lines are expressed in per cent of the 92 kev line.

assignment at the present time in terms of theoretically derived ratios or empirical curves. The only statement which can be made is that the sum of their spin changes is one, and that one of them involves a change in parity. From the relative intensities in Table IV, it appears as if the 34 kev transition is the stronger of the two. The 46 kev transition observed by Keller and Cork (33) would support this assignment, although the present measurements do not allow the positive identification of this gamma transition. Accordingly, the 34 kev transition is put below the 100 kev transition in the energy level diagram, indicating that beta decay may occur directly to this level and account for the additional intensity.

2. The 175 kev Level in Pr-144

The existence of a 175 kev level in Pr-144 was first suggested by Emmerich, John and Kurbatov (29) on the basis of energy balance in the gamma rays inferred from internal conversion lines. It was observed that the energy sum of the 134 kev and the 41 kev gamma rays, as well as the 81 kev and 94 kev, is 175 kev in both cases. The assignment is confirmed by Keller and Cork (33), but Porter and Cook (28) do not find any evidence of a 41 kev and a 94 kev transition on which the existence of this level is based.

The increased resolution of the present work shows clearly that a peak in the region of 52-53 keV is complex, as shown in Figure 53. This indicates a K peak of the 94 keV transition at 52 keV. An attempt to identify the corresponding L line has not been completely successful. Some densitometer graphs show an indication for a line of the correct energy, but overlapping of the 134 keV K line at 92 keV with much higher intensity makes the identification of the 58 keV L line difficult.

The existence of the 41 keV gamma ray is based on an analysis of the Auger electrons. This is necessary because the L line of the 41 keV gamma ray falls practically at the same energy as the KLM Auger line for praseodymium.

First, the observed intensity of the 29 keV internal conversion line is 12 in the notation of Table IV. The Auger intensity for the KLL line is 10 as calculated from the fluorescence yield in praseodymium and the L/M ratio for Auger electrons given by Burhop (34). The agreement is sufficiently close to assume that the 29 keV line is entirely due to the Auger electrons.

This is not so for the 34 keV line. The observed intensity is 17 whereas the calculated value for the KLM Auger line turns out to be six. The excess of 11 is then interpreted as the L internal conversion line

of the 41 kev gamma ray.

An attempt to detect direct electromagnetic radiation of 175 kev to the ground state has been unsuccessful. The scintillation spectrometer data show no indication of a peak in this region. The K conversion line of such a transition almost equals the 133 kev M line in energy. The intensity of the 133 kev line is given as three. This is not excessively strong. Although the L/M ratio to be observed for an M1 transition in this energy range has not been calculated it is estimated that this ratio may be as high as six or eight. In that case, one half of the observed intensity may, indeed, be due to K conversion of the 175 kev transition.

3. The 60 kev Transition in Nd-144

The position of the 60 kev gamma ray inferred from internal conversion in the Pr-144 disintegration remains unresolved in the present measurements. This transition is claimed by Keller and Cork (33), and confirmed by Porter and Cook (28). No evidence has been detected with a scintillation spectrometer for free gamma radiation of 60 kev in Pr-144 which had been separated from Ce-144 chemically to a purity of better than 2×10^{-5} . The spectrum showed only Compton scattering from high energy gamma radiation and bremsstrahlung of the beta transitions in this energy range. As a further

check, the neighborhood of the three high energy gamma rays known to exist in the disintegration has been examined with the scintillation spectrometer. The results are shown in Figure 54, and appear to be negative. It is expected that transitions of ± 60 kev in energy from the known peaks occur if a level exists which differs by 60 kev from the ground state or any of the other levels. No electromagnetic radiation was found of this type with an estimated intensity of more than 10 per cent of the 1.48 Mev line, which is the weakest of the set.

Internal conversion lines have been observed, however, as shown in Figure 53 and Table IV, which agree in energy and in intensity with those described by the previous authors.

4. The Branching Ratios in Ce-144

The determination of the branching ratios for the Ce-144 disintegration is made with the aid of internal conversion measurements in the photographic permanent magnet spectrograph, and by means of electromagnetic radiation observed with a scintillation spectrometer.

The K/L ratios as shown in Table IV for the 134 kev and the 81 kev transitions are in agreement with the assignment of M1 and M2 radiation respectively, as compared to the empirical curves of Goldhaber and Sun-

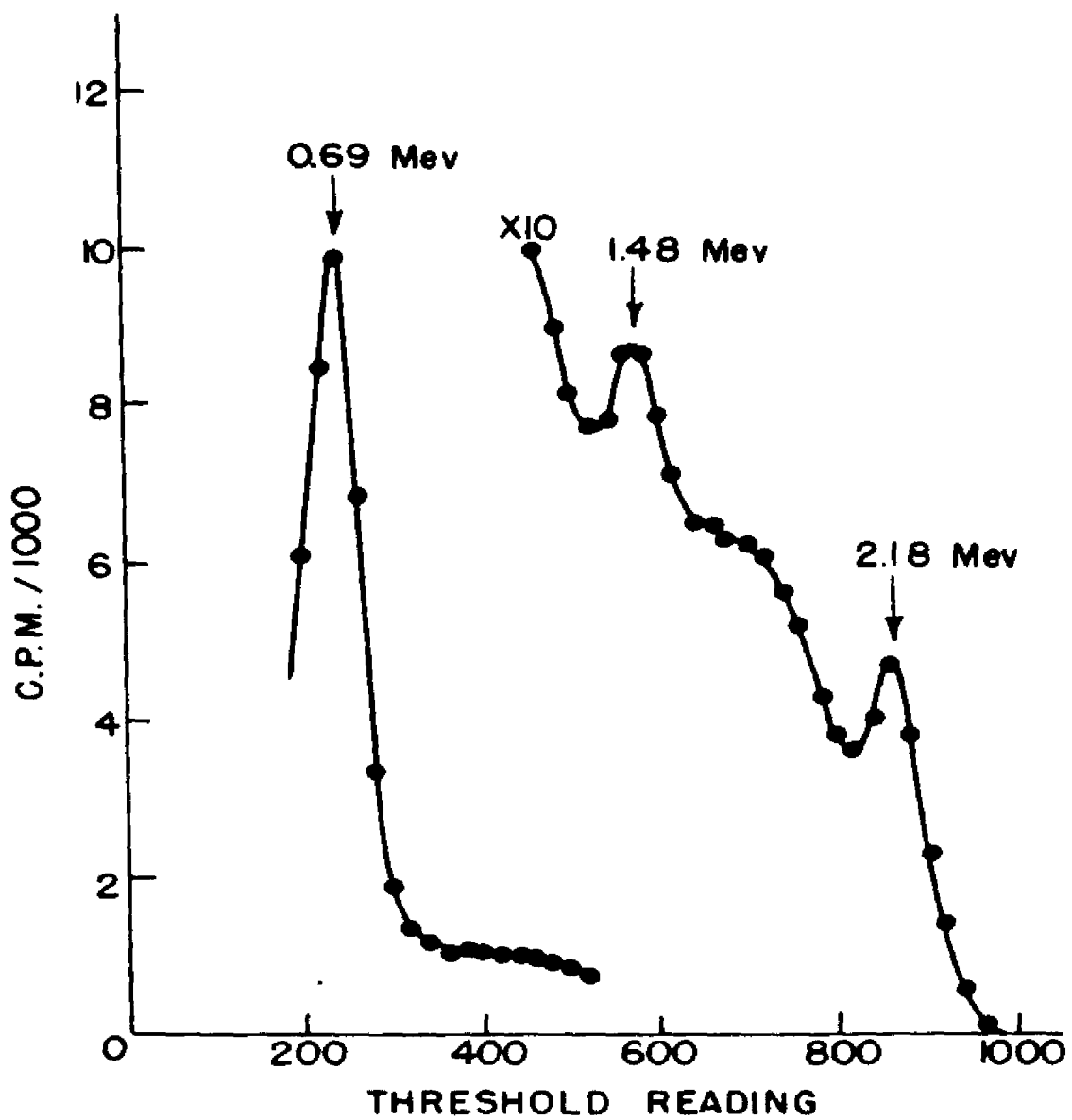


FIGURE 54 SCINTILLATION SPECTROGRAM OF Pr 144

yar (35). This observation forms the basis on which the beta intensity calculations are founded. For the M1 transition, the K conversion coefficient is found to be 0.5 as extrapolated from the theoretical calculations of Rose et al (36).

In terms of the intensity scale used in Table IV, the free gamma radiation of the 134 kev transition is 200 and the total transition probability is 315. For the 81 kev gamma ray, the extrapolated K conversion coefficient is about 10 making the total transition probability equal to 64. The extrapolation beyond the calculated values is very far, so the accuracy of the method is questionable. A scintillation spectrogram of the low energy region in Ce-144 is shown in Figure 55. This shows clearly a peak for the 134 kev transition, a second peak in the region of 80 kev and a third peak at 35 kev, believed to be the x-rays of praseodymium. A subtraction is difficult to perform, since the shape of the underlying spectrum is not known. An estimate yields a ratio of between ten and twenty for the intensity of the 81 kev peak with respect to the 134 kev peak. This is to be compared to the ratio of $200/5$ obtained from the theoretical extrapolation. In either case, the free electromagnetic radiation associated with the 81 kev transition is very small, and any other gamma ray intensities in the

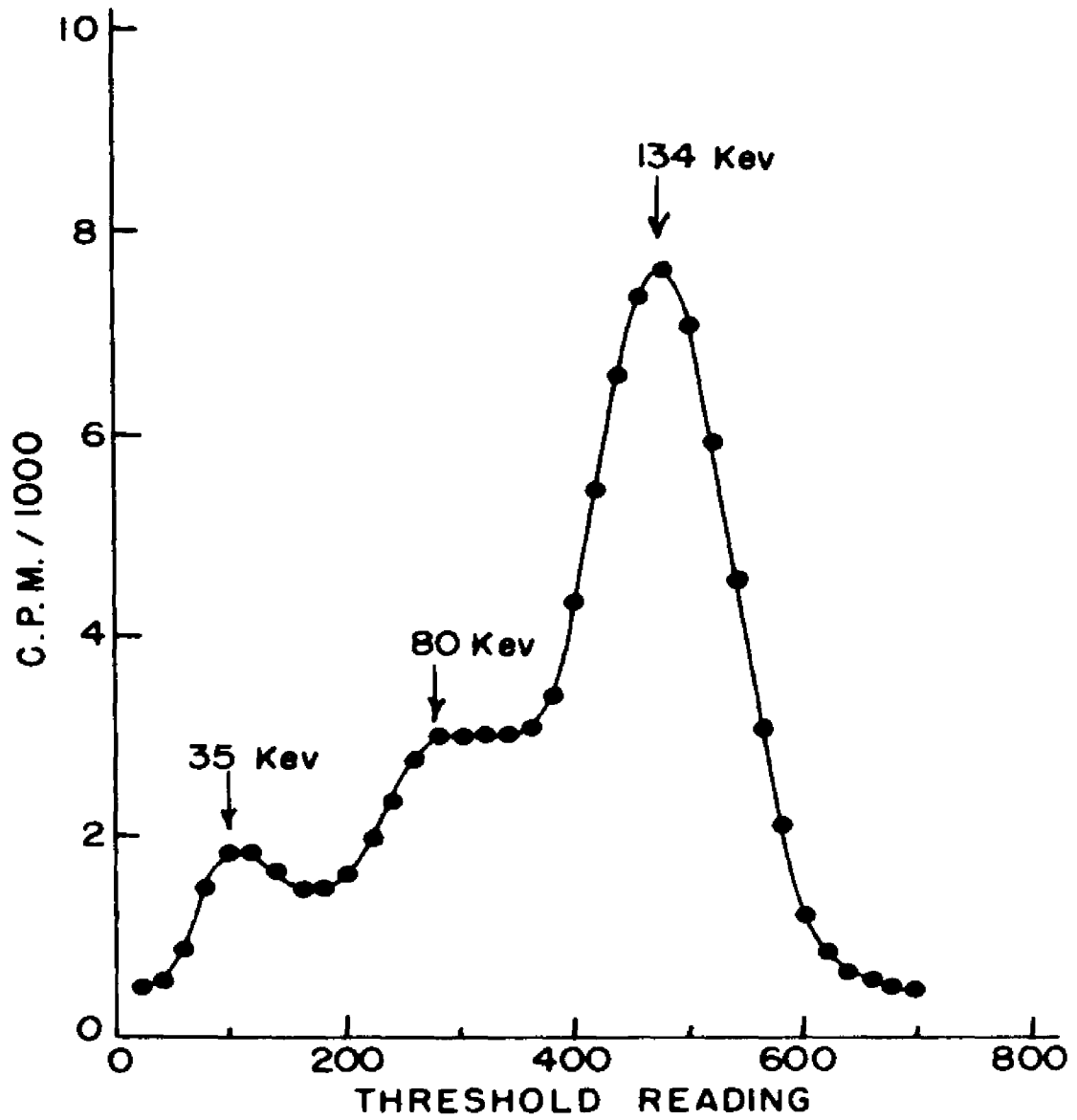


FIGURE 55 SCINTILLATION SPECTROGRAM OF CERIUM 144

energy region from 50 to 100 kev are negligible.

With this information and the knowledge of the intensity ratio of the 304 kev beta spectrum of Ce-144, which is known to be 70 per cent of the total Ce-144 disintegration from several independent investigations, the branching ratios in Ce-144 can be calculated. For convenience, the pertinent data are summarized as follows:

1. The combined inner spectra equal a total intensity of 30 per cent of the disintegration.

2. The sum of the conversion electrons represent an intensity of 218 in the notation of Table IV.

3. The sum of the free gamma radiation represents an intensity of 220 in the notation of Table IV.

Consequently, an intensity of 438 in Table IV represents 30 per cent of the disintegration. In order to calculate the branching ratio for the 170 kev beta transition which feeds the 134 kev level, consider the 41 kev gamma, which also feeds this level, and the 134 kev and 100 kev transitions which are emitted from the level. Since the intensity contributions of the 41 kev and the 100 kev transitions are small and opposed to each other in this calculation, they may be neglected without introducing a sizable error. The contribution

in per cent of the total disintegration for the 134 keV transition is then $30 \times 315/438 = 22$ per cent. Similarly, for the 223 keV beta ray, which feeds the 81 keV level, consider the 53 keV and 94 keV transitions and the 81 keV transition. The intensity of the 81 keV transition is $30 \times 64/438 = 4.4$ per cent. From this must be subtracted the contribution due to the 53 keV and 94 keV transitions.

The 53 keV transition occurs between states having a change in spin of one, and a change in parity. The lowest allowed multipoles are E1 and M2. Only the L conversion line is experimentally observed, with an intensity of three. The theoretical calculations for L conversion in E1 transitions have been carried out by Gellman et al (37). The interpolation yields an L conversion of about one. In case of an M2 transition, the electromagnetic contribution would be even smaller.

In regard to K/L ratios, only one case of E1 transitions is listed by Goldhaber and Sunyar (35). This has a K/L ratio of three. For M2 transitions, the K/L ratio in this region is also three. Thus a K/L ratio of three and negligible electromagnetic contribution may be assumed. The intensity is $30 \times 12/438 = 0.8$ per cent. For the 94 keV transition, only the K peak is observed with an intensity of seven. The L peak is not clearly resolved, but an indication of its

existence is found in some of the photo-densitometer graphs. It appears to have an intensity of about two. This gives a transition intensity of equal or less than $30 \times 9/438 = 0.6$ per cent.

Subtracting the last two values from 4.4 per cent yields equal or less than three per cent for the branching ratio of the 223 kev beta transition.

For the spectra of the Ce-144 disintegration, the following branching ratios are obtained:

304 kev	70 per cent
223 kev equal or less than	3 per cent
170 kev	22 per cent
others equal or less than	5 per cent

The contributing spectra combined under "others" including those feeding the 175 kev and the 34 kev levels.

5. The Branching Ratios in Pr-144

In order to determine the beta decay branching in Pr-144, a relative intensity measurement was made of the beta emission to the ground state and the gamma ray intensity from the excited state of 695 kev in Nd-144. More accurate results are likely by this method than by a Kurie plot analysis of the beta spectra, because the branching ratio is small and therefore large subtractions are involved in the Kurie plot analysis. Furthermore, the Kurie plot analysis is dependent on

the variation of the matrix element of the transition with energy. There is no a priori reason to believe that the Kurie plot for any beta transition be a straight line.

The relative intensity measurements were carried out with the aid of the well known radiations of Cs-137 by comparison methods. Corrections were applied for internal conversion in Ba-137 in accordance with the results obtained by M. Waggoner (38).

Geometrically similar sources were prepared on thin rubber hydrochloride backing. The relative intensity of the gamma rays was measured in the scintillation spectrometer.

The results of a beta ray absorption measurement are shown in Figure 56. The total electron activity is obtained by extrapolating the absorption to zero absorber thickness. In the case of Cs-137, this includes about eight per cent of beta rays directly to the ground state of Ba-137 and 10 per cent internal conversion electrons of the 662 kev gamma transition. For Ce-144 and Pr-144, the extrapolation is made for the high energy beta spectra which represent practically all of the disintegration. This needs no further adjustment since the internal conversion electrons for the gamma rays are negligible. A rise above the extrapolated line at low energies represents the

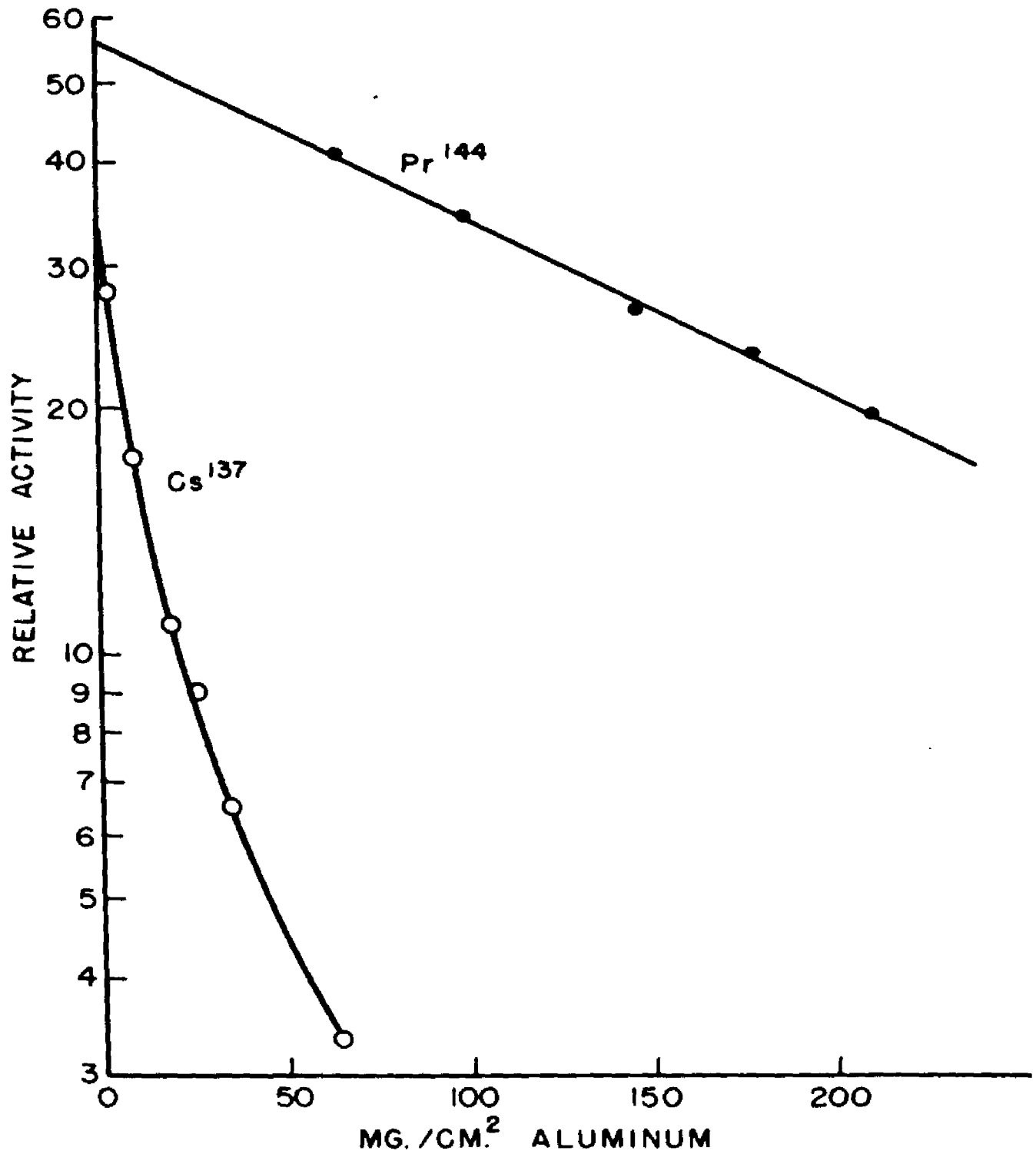


FIGURE 56 ABSORPTION MEASUREMENT OF RELATIVE BETA INTENSITY

effect of the presence of the Ce-144 spectra, and is omitted in Figure 56.

The scintillation spectrometer results are given by Figure 57. Contributions of the two photopeaks are compared above the background count. The calculated intensity of the 695 kev gamma ray in the Pr-144 disintegration is 1.25 ± 0.2 per cent of the total beta activity. The error in this figure is for the uncertainty with which the beta absorption data are extrapolated to zero absorber thickness.

In order to compute the branching ratios for the beta ray components of Pr-144, this information is combined with the relative intensities of the three gamma rays of 695, 1480, and 2185 kev as measured by Alburger and Kraushaar (30). The values given by these authors are 1, 0.4, and 1.1 for these gamma rays respectively with a probable error of about 20 per cent. A qualitative check of these values by means of a scintillation spectrometer indicates that the last two values appear to be roughly correct, but the intensity of the 695 kev transition may be somewhat low.

The branching ratios for the three beta ray components in Pr-144 are:

2.98 Mev	97.3 per cent
2.28 Mev	0.8 per cent
0.80 Mev	1.9 per cent

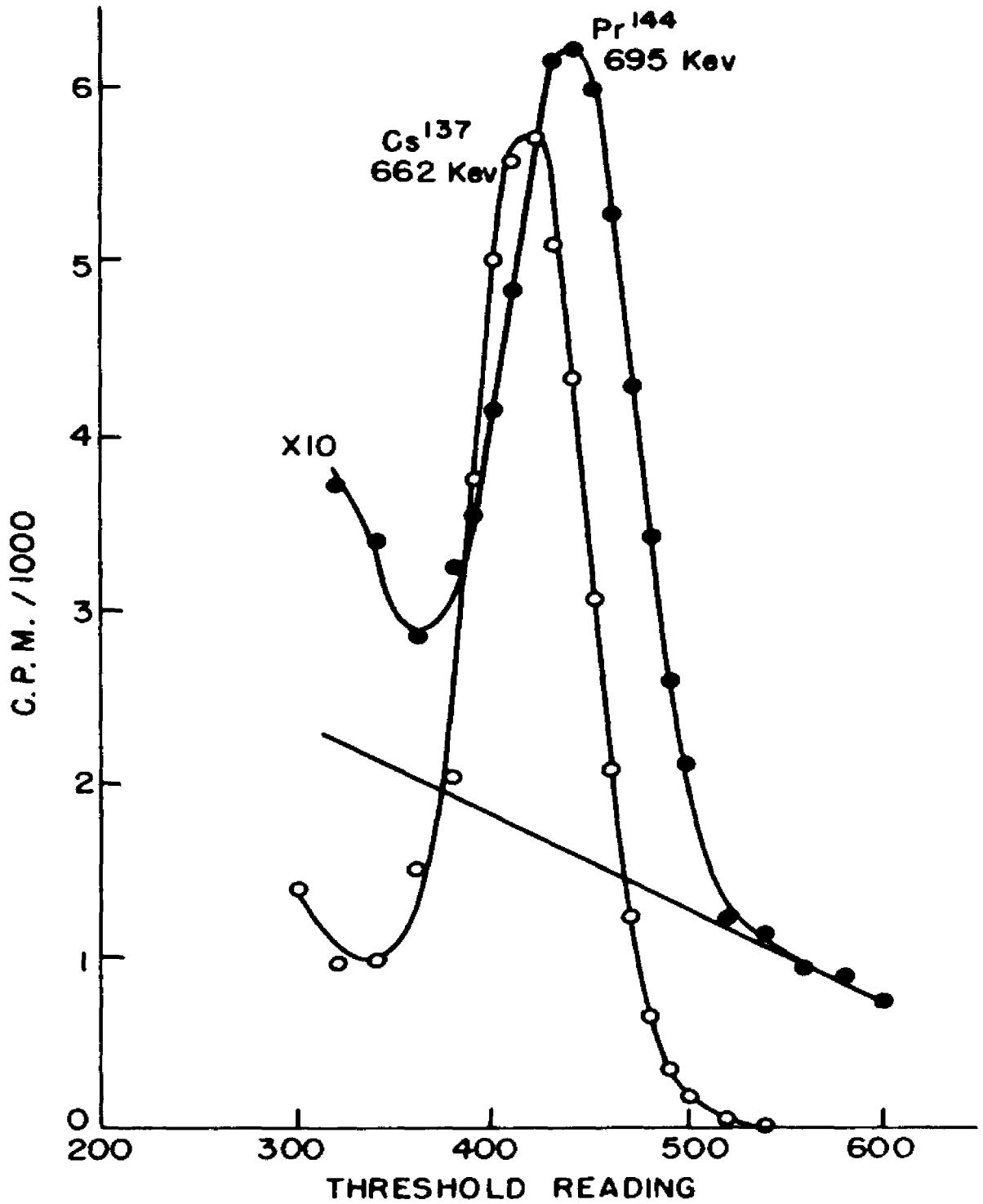


FIGURE 57 SCINTILLATION SPECTROMETER MEASUREMENT OF RELATIVE GAMMA INTENSITY

The results for the 2.28 Mev transition are found to be in satisfactory experimental agreement with the measurements of Porter and Cook (28) but lower than the Kurie plot analysis of W. J. Auth (39). This will be used later in the discussion of the spin and parity assignments for the excited states in Nd-144.

D. DISCUSSION OF THE BETA TRANSITIONS

A tabulation of the results for the beta transitions obtained from the data of Table IV is shown in Table V. The difference in the ft values between the 0.30 Mev transition of Ce-144 and the 2.98 Mev transition of Pr-144 originally observed by Porter and Cook (28) is confirmed here. Both ft values fall within the range of first forbidden transitions, so the discrepancy is not large enough to warrant the consideration of a low lying state in Nd-144, which has so far escaped detection. Such a level would have to be in Nd-144 rather than in Pr-144, because the ft value of the 2.98 Mev is the lower one, and consequently would require the more favorable level. The spectrum of electromagnetic radiation was checked with a scintillation counter down to three kev without finding any unusual amount of radiation. It is, of course, possible that such a low energy transition, though very intense, may be highly internally converted. In that case, the scintillation spectrometer could not detect any

TABLE V

Beta Transition Values

<u>Parent Nucleus</u>	<u>Energy in Mev</u>	<u>Initial State</u>	<u>Final State</u>	<u>Spin, Parity Changes</u>		<u>Log ft Value</u>
Ce-144	0.30	(0+)	(0-)	0	Yes	7.5
Ce-144	0.22	(0+)	(2+)	2	no	8.4
Ce-144	0.17	(0+)	(1-)	1	yes	7.2
Pr-144	2.98	(0=)	(0+)	0	yes	6.6
Pr-144	2.28	(0-)	(2+)	2	yes	8.1
Pr-144	0.80	(0-)	(1-)	1	no	6.0

radiation. The alternative is to assume that the beta transition from an even-even nucleus to an odd-odd nucleus is governed by different rules than that from an odd-odd nucleus to an even-even nucleus. That such differences may occur theoretically, is shown by Brisk (40).

The ft values of the inner spectra of Ce-144 are obtained without direct experimental evidence for existence of these transitions. They are based solely on the requirements imposed by the internal conversion and free gamma ray intensities.

The $\log ft$ value of 8.4 given for the 0.22 Mev transition is probably low. The spin change of two without change in parity makes this transition second-forbidden. The 0.17 Mev transition is first-forbidden with a spin change of one, and parity change. Its ft value falls in line with those listed by Nordheim (41).

The 2.23 Mev transition has a $\log ft$ value of 8.1 which appears to be correct for a spin change of two with parity change.

The $\log ft$ value of 6.0 obtained for the 0.80 Mev transition occurs just at the traditional border line between allowed and first-forbidden transitions. It is plausible that the transition is allowed considering the relatively high ft values observed for first-forbidden transitions in this region of the isotopic

table (41). The assignment of negative parity for the final state of the 0.80 Mev beta ray also agrees with a rule recently suggested by Glaubman (42) for spins and parities of excited states in even-even nuclei.

E. EXCITED STATES OF THE EVEN-EVEN NUCLEUS Nd-144

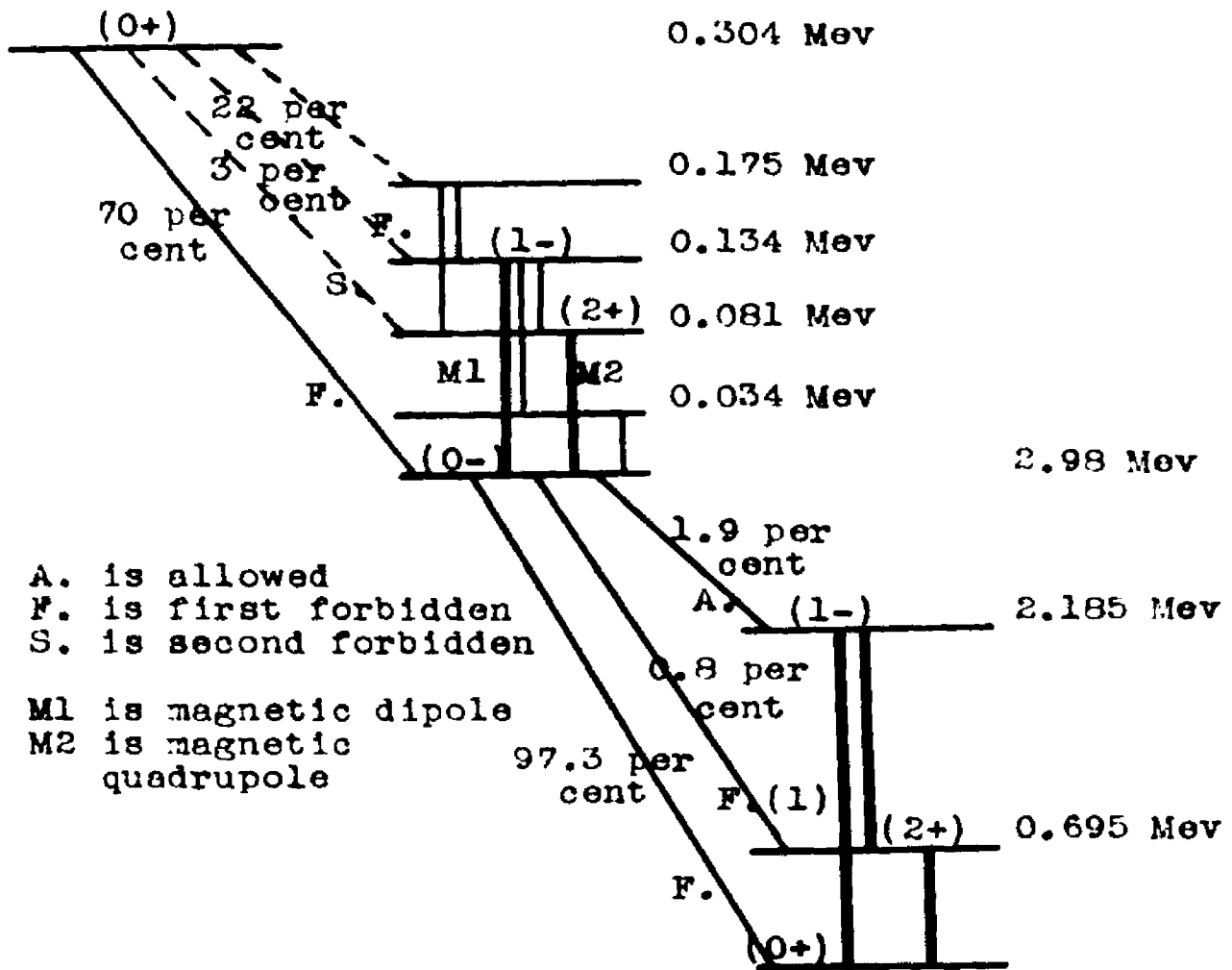
It may be possible that the (1-) level of 2185 kev is third or higher among the excited states in Nd-144, rather than second as is apparently the case in this decay. The second excited states of even-even nuclei occur generally as (4+) states or (2+) for heavy elements as discussed by Scharff-Goldhaber (43). A single additional state of (4+) in the energy range between 695 and 2185 kev would be fed with insufficient intensity either through beta or gamma transitions for observation in the present investigation. A beta disintegration would necessitate a spin change of four, which is highly forbidden. A gamma transition from the (1-) level requires a spin change of three with a change in parity, for which the lowest allowed multipoles are E3 or M4. These would not be observable in competition with the E1 or M2 direct transitions to the ground state, since the level is fed with only about one per cent of the total disintegration.

The 695 kev state is a (2+) state as found by Alburger and Kraushaar (30). This agrees with the rule of Goldhaber and Sunyar (35) that all first excited

states of even-even nuclei are of this type.

F. THE SCHEME OF DISINTEGRATION FOR Ce-144 AND Pr-144

An application of the results obtained in the present investigation to the information already known, is presented in form of the scheme of disintegration for Ce-144 and Pr-144 shown in Figure 58. Energy levels for which the position in the scheme is uncertain, are shown in dotted lines. Transitions which are not directly observed, are likewise shown in dotted lines. Electromagnetic transitions which are observable both through electron lines and scintillation measurements are shown as extra heavy lines in the decay scheme.



Cerium-144 Praseodymium-144 Neodymium-144

Figure 58 . The scheme of Disintegration for Ce-144 and Pr-144.

BIBLIOGRAPHY

- (1) J. K. Knipp and G. E. Uhlenbeck, *Physics*, 3, 425 (1936).
- (2) Felix Bloch, *Phys. Rev.*, 50, 272 (1936).
- (3) P. Morrison and E. I. Schiff, *Phys. Rev.*, 58, 24 (1940).
- (4) C. S. W. Chang and D. L. Falkoff, *Phys. Rev.*, 76, 365 (1949).
- (5) J. M. Jauch, ORNL Report 1102, unpublished (1952).
- (6) H. Bradt, et al., *Helv. Phys. Acta*, 19, 222 (1946).
- (7) D. Maeder and P. Treiswerk, *Phys. Rev.*, 84, 595 (1951).
- (8) Bell, Jauch and Cassidy, *Science*, 115, 12 (1952).
- (9) Bolgiano, Madansky and Rasetti, *Phys. Rev.*, 89, 679 (1952).
- (10) Anderson, Wheeler and Watson, *Phys. Rev.*, 90, 606 (1953).
- (11) E. derMateosian and A. Smith, *Phys. Rev.*, 88, 1186 (1952).
- (12) S. E. Singer, Ph.D. Dissertation, The Ohio State University, unpublished (1953).
- (13) C. W. Johnstone, private communication.
- (14) D. Engelkemeir, unpublished
- (15) D. Maeder and V. Wintersteiger, *Physica*, 18, No. 12, 1147 (1952).
- (16) P. H. Stelson and W. M. Freston, *Phys. Rev.*, 83, 469 (1951).
- (17) Richards, Smith and Browne, *Phys. Rev.*, 80, 524 (1950).

- (18) Schoenfeld, Duborg, Preston and Goodman, Phys. Rev., 85, 873 (1952).
- (19) J. J. McCue and W. M. Preston, Phys. Rev., 84, 384 (1951).
- (20) H. A. Bethe and R. F. Bacher, Rev. Mod. Phys., 8, 122 (1936).
- (21) Brosi, Borkowski, Conn and Gries, Phys. Rev., 81, 391 (1951).
- (22) G. Friedlander, Brookhaven National Lab. report, BNL-AS2, unpublished (1949).
- (23) H. W. Wilson, private communication.
- (24) L. E. Marshak, Phys. Rev., 61, 431 (1942).
- (25) E. Feenberg and G. L. Trigg, Rev. Mod. Phys., 22, 399 (1950).
- (26) J. Davidson, Phys. Rev., 82, 48 (1951).
- (27) Hollander, Perlman and Seaborg, Rev. Mod. Phys., 25, 469 (1953).
- (28) F. Porter and C. S. Cook, Phys. Rev., 87, 464, (1952).
- (29) Emmerich, John and Kurbatov, Phys. Rev., 82, 968 (1951).
- (30) D. E. Alburger and J. J. Kraushaar, Phys. Rev., 87, 448 (1952).
- (31) W. S. Emmerich, Thesis, The Ohio State University, unpublished (1950).
- (32) Rutledge, Cork and Burson, Phys. Rev., 86, 775 (1952).
- (33) H. B. Keller and J. M. Cork, Phys. Rev., 84, 1079 (1951).
- (34) E. H. S. Burhop, The Auger Effect, Camb. U. Press, 48 (1952).
- (35) M. Goldhaber and A. W. Sunyar, Phys. Rev., 83, 906 (1951).

(36) Rose, Goertzel, Spinrad, Harr and Strong, Phys. Rev., 83, 79 (1951).

(37) Gellman, Griffith and Stanley, Phys. Rev., 85, 944 (1952).

(38) M. A. Waggoner, Phys. Rev., 82, 906 (1951).

(39) W. J. Auth, Thesis, The Ohio State University, unpublished (1953).

(40) H. Brisk, Phys. Rev., 90, 365 (1953).

(41) L. W. Nordheim, Rev. Mod. Phys., 23, 322 (1951).

(42) M. J. Glaubman, Phys. Rev., 90, 1000 (1953).

(43) G. Scharff-Goldhaber, Phys. Rev., 90, 587 (1953).

AUTOBIOGRAPHY

I, Werner S. Emmerich, was born in Düsseldorf, Germany, June 3, 1921. I received my secondary school education in the public schools of the city of Düsseldorf, Germany. My undergraduate training was obtained at The Ohio State University, from which I received the degree Bachelor of Science, cum laude and with distinction in Physics, in 1949. From The Ohio State University, I received the degree Master of Science in 1950, and an appointment as University Scholar in the Department of Physics and Astronomy. In 1951 I received an appointment as University Fellow in The Ohio State University. In 1953 I received an appointment as Research Fellow in The Ohio State University. I held this position while completing the requirements for the degree Doctor of Philosophy.